International Journal of Applied Mechanics
Vol. 18, No. 1 (2026) 2530004 (88 pages)

DOI: 10.1142/S1758825125300044

World Scientific
www.worldscientific.com

Advances in Experimental and Computational Methods for Studying Mechanical Properties of Double Network Hydrogels

Zidi Zhou *, Jiapeng You †,‡, Jianxi Huang * and Zishun Liu *,†,§

*City University of Hong Kong (Dongguan)
Dongguan 523808, P. R. China

†City University of Hong Kong, Hong Kong
Hong Kong 999077, P. R. China

‡International Center for Applied Mechanics
State Key Laboratory for Strength and Vibration
of Mechanical Structures, School of Aerospace Engineering
Xi'an Jiaotong University, Xi'an 710049, P. R. China
§zishun.liu@cityu-dg.edu.cn

Received 11 December 2025
Revised 16 December 2025
Accepted 16 December 2025
Published 13 January 2026

Double network (DN) hydrogels have emerged as a transformative class of soft materials, successfully resolving the trade-off between high water content and mechanical robustness. Their exceptional toughness stems from a sacrificial mechanism wherein a rigid network fractures to dissipate energy, while a ductile matrix network maintains structural integrity. Despite progress in synthesis, fully capturing the complex, nonlinear mechanical behaviors of DN gels often requires advanced characterization techniques and even computational modeling. To address this, this review systematically summarizes recent advances in experimental and computational methods for studying the mechanical behavior of DN gels. We discuss experimental techniques ranging from standard macroscopic tests to emerging non-contact methods, alongside computational methods such as molecular dynamics, network simulations, finite element methods and machine learning. The paper concludes by identifying current challenges and outlining future directions for the field.

Keywords: Double network hydrogels; mechanical behavior; experimental characterization; computational modeling.

1. Introduction

Hydrogels, three-dimensional polymer networks swollen with large amounts of water (typically >90%), have garnered significant attention since the pioneering work of Wichterle and Lím in the 1960s [Huang *et al.*, 2020; Lei *et al.*, 2021b; Liu *et al.*, 2015; Wichterle and Lím, 1960]. Although their resemblance to biological tissue

§Corresponding author.

makes them ideal candidates for applications such as contact lenses and wound dressings, traditional single-network (SN) hydrogels suffer from a critical limitation: they are mechanically brittle. With an elastic modulus of several kilopascals, a strength of a few tens of kilopascals, and a fracture energy of around $10\,J/m^2$, these materials can easily deform and typically fail catastrophically under minimal loads. This paradigm shifted fundamentally in 2003 when Gong and coworkers introduced the concept of double network (DN) hydrogels [Gong *et al.*, 2003]. Unlike traditional interpenetrating polymer networks (IPNs) composed of chemically similar polymers, the DN strategy is predicated on strong structural asymmetry. A classical DN gel comprises a rigid, brittle polyelectrolyte network (termed the first network) that is tightly crosslinked, and a soft, ductile neutral polymer network (termed the second network) that is loosely crosslinked and present in a higher molar ratio relative to the first [Chen *et al.*, 2015; Eshaghi *et al.*, 2014; Huang *et al.*, 2007; Johnson *et al.*, 2010; Na *et al.*, 2004; Nakajima *et al.*, 2009; Nakajima, 2017; Shestakova *et al.*, 2011]. The typical structure of DN gels across the molecular to macroscopic scale is illustrated in Fig. 1. Although the two constituent networks are mechanically inferior, the synergy arising from this specific architecture results in DN gels with a leap in mechanical performance, including superior strength, fracture toughness, stretchability and wear resistance [Gong, 2010; Kaneko *et al.*, 2005; Teng *et al.*, 2025; Yang *et al.*, 2022]. Consequently, DN gels have found applications across diverse fields, ranging from food science and biomedical devices to tissue engineering, environment protection and soft robotics [Costa and Mano, 2015; Khalesi *et al.*, 2020; Liu *et al.*, 2017; Milner *et al.*, 2018; Murosaki *et al.*, 2009; Nonoyama and Gong, 2021; Selvamuthu *et al.*, 2023; Takagi *et al.*, 2019; Tominaga *et al.*, 2007; Wang *et al.*, 2022; Yasuda *et al.*, 2009; Yin *et al.*, 2023; Yuk *et al.*, 2019; Zhang *et al.*, 2023a].

The invention of DN gels has attracted broad interdisciplinary interest, prompting material scientists and mechanicians to elucidate their unique mechanical properties. Extensive research has been conducted to establish the relationship between network structure and mechanical behavior. Key areas of investigation

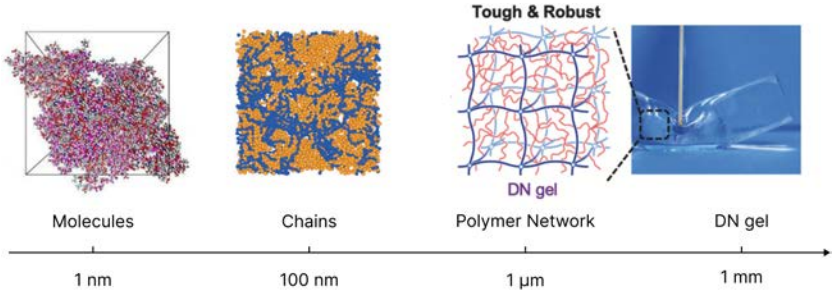

Fig. 1. Multiscale structure of DN gels. The DN gel is shown across four distinct scales: molecular (∼1 nm), chain (∼100 nm), network (∼1 μ m), and macroscopic (∼1 mm) [Higuchi *et al.*, 2018; Nonoyama and Gong, 2021; Zong *et al.*, 2024].

Source: Copyright 2024 AIP Publishing; Copyright 2018 American Chemical Society; Copyright 2020 The Society of Polymer Science.

include the underlying strengthening and toughening mechanisms [Brown, 2007; Fukao *et al.*, 2020; Morovati and Dargazany, 2019; Morovati *et al.*, 2020; Nakajima *et al.*, 2013; Tanaka, 2007], the effect of the network components and topology, yielding criteria, the brittle to ductile transition, and the characterization of the damage zone [Ahmed *et al.*, 2014; Eshaghi and Weiss, 2016; Frauenlob *et al.*, 2019; Jia *et al.*, 2022; Kopnar *et al.*, 2025; Lu *et al.*, 2024; Matsuda *et al.*, 2016, 2025; Na *et al.*, 2004; Tsukeshiba *et al.*, 2005; Wang *et al.*, 2025a; Xin *et al.*, 2013; You and Liu, 2024; You *et al.*, 2025a,b]. Furthermore, researchers have examined the influence of environmental and loading factors, such as prestretch, freeze-thaw cycles, tear velocity, water content, etc., on mechanical performance [Eshaghi *et al.*, 2018; Furukawa *et al.*, 2008; Itagaki *et al.*, 2010; Liang *et al.*, 2012; Tominaga *et al.*, 2012; Zheng *et al.*, 2023b, 2024a].

The extraordinary toughness of DN gels is attributed to a distinct coupling effect between the two constituent networks. Upon deformation, the rigid first network, which contains shorter chain segments, reaches its extension limit and fractures preferentially. Crucially, this fracture does not propagate into a macroscopic failure; instead, it occurs diffusely throughout the material, forming damaged clusters or micro-cracks that dissipate enormous amounts of mechanical energy. Simultaneously, the ductile second network acts as a matrix that bridges these micro-cracks to sustain the load and maintain structural integrity. Over the past two decades, this DN principle has evolved from applied to specific chemical compositions to a universal design philosophy. Researchers such as Sun *et al.* [2012] expanded the concept by incorporating reversible physical bonds into the first network. These tough gels not only dissipate energy but also possess self-healing capabilities due to the reversible nature of the sacrificial bonds. Later, Nakajima *et al.* [2012] demonstrated that the DN gel does not necessarily require a polyelectrolyte constituent; any rigid, pre-stretched network can serve as the sacrificial scaffold, allowing the DN strategy to toughen a broad range of neutral hydrogels [Wang *et al.*, 2019; Zhu *et al.*, 2024b]. Recent innovations have further advanced the field, leading to self-growing DN gels and various variants of DN gels. These materials retain high toughness while also exhibiting stimuli-responsiveness, shape memory, low plastic deformations, etc. [Chen *et al.*, 2021; Fang *et al.*, 2024; Hsu *et al.*, 2019; King *et al.*, 2019; Matsuda *et al.*, 2019; Wang *et al.*, 2025c; Xu *et al.*, 2021; Yang *et al.*, 2018a] .

The rapid development of DN gels has spurred further research into this type of material. Beyond fracture toughness, researchers are increasingly interested in behaviors such as necking, asymmetric-rate sensitivity, inverse mechanical-swelling coupling, shape change/memory effect, etc. [Ahmed *et al.*, 2014; Imaoka *et al.*, 2023; Mao *et al.*, 2017; Na *et al.*, 2006; Yu *et al.*, 2009; Zhang *et al.*, 2014]. To comprehensively characterize these properties and elucidate the underlying mechanisms, diverse experimental and computational methods have been employed. In the early 2000s, experimental methods were primarily adapted from established techniques for rubber-like materials, including tension testing, compression testing, and

the measurement of fracture toughness and fatigue threshold. These early methods established a preliminary framework for understanding DN gels. In the past decade, however, the experimental landscape has expanded significantly to address complex boundary conditions while maintaining high accuracy. Recent studies have focused on interfacial properties, such as adhesive strength and toughness, as well as factors that govern crack sensitivity, pre-stretching effects, fatigue behavior, tribology, and rheology. Notably, there has been a shift toward novel characterization techniques, particularly non-contact methods, that enable refined, *in situ* measurements. In summary, modern experimental methods provide reliable data with high accuracy, facilitating the discovery of unforeseen phenomena and validating complex systems that remain challenging to model.

Complementing experimental approaches, computational methods provide an efficient and cost-effective means to investigate DN gels, circumventing the limitations of expensive instrumentation and complex material synthesis processes. Propelled by advances in computational science, numerical studies of DN gels have witnessed rapid development. Molecular dynamics (MD) simulations have evolved from early all-atom and coarse-grained (CG) models to multiscale models that surmounted spatiotemporal limitations, enabling the study of larger systems over extended timescales. At the mesoscale, discrete network simulations simplify polymer chains by abstracting chain configurations while incorporating random crosslinker placement to reflect realistic structural stochasticity. This method is particularly advantageous for studying fracture behaviors, as it explicitly simulates crack initiation and propagation through individual chain scission events, which are difficult to capture in continuous media. At the macroscopic scale, finite element methods (FEM) are employed to solve boundary value problems involving complex loading conditions, providing intuitive visualizations of stress–strain relationships. More recently, machine learning (ML) has emerged as a powerful tool for predicting mechanical properties and accelerating material design. These computational methods not only validate experimental findings but also challenge established paradigms and guide future material design. Thus, a synergistic combination of experimental and computational methods is essential for advancing the field.

In this review, we focus on state-of-the-art experimental and computational methods used to investigate the mechanical properties of DN gels. This paper is organized as follows. Sections 2 and 3 cover recent advances in experimental characterization and computational modeling, respectively. Section 4 discusses current challenges in the field. Section 5 provides conclusions and an outlook on future research directions.

2. Experimental Methods for Studying Mechanical Properties

2.1. *Uniaxial tension and compression testing*

Uniaxial testing stands as one of the most fundamental and accessible methods for characterizing the mechanical properties of DN gels. It principally encompasses

two loading modes: uniaxial tension and compression, both of which may be conducted under monotonically or cyclically loading profiles. Beyond capturing the characteristic deformation behavior of DN gels, uniaxial tests are essential for quantifying critical mechanical parameters, including initial elastic modulus, strength, stretchability, work of fracture and energy dissipation.

2.1.1. *Specimen geometry and basic definitions*

Specimen geometry varies fundamentally between tension and compression. For uniaxial tension, the DN gel samples are typically shaped into a dumbbell configuration characterized by an initial gauge length of L, width of W, and thickness of T [Fig. 2(a)]. Specific dimensions generally adhere to standards for rubber-like materials (e.g., ISO 37: 2024). A widely adopted geometry has gauge dimensions of 20 mm × 4 mm × 2 mm ($L \times W \times T$). In contrast, uniaxial compression utilizes cylindrical specimens with a diameter of D and a thickness of T. To prevent buckling instability and ensure measurement accuracy, the aspect ratio is usually constrained to $T/D < 2$ [Es-haghi and Weiss, 2016] [Fig. 2(b)]. A representative dimension for such specimens is 9 mm × 4 mm ($D \times T$) [Gong *et al.*, 2003; Matsuda *et al.*, 2016; Webber *et al.*, 2007].

Uniaxial tension and compression tests are typically conducted using a universal testing machine equipped with different fixtures. For tensile testing, the ends of the dumbbell-shaped specimen are secured by parallel-plate clamps, and the upper gripper rises vertically at a constant velocity. Conversely, for compression testing, the cylinder-shaped specimen is centered on a lower fixed platen, while an upper platen descends vertically at a constant velocity. To ensure accurate compression data, lubricants such as silicone oil are applied between the specimen and platens to facilitate free sliding and to mitigate specimen dehydration. Furthermore, platen

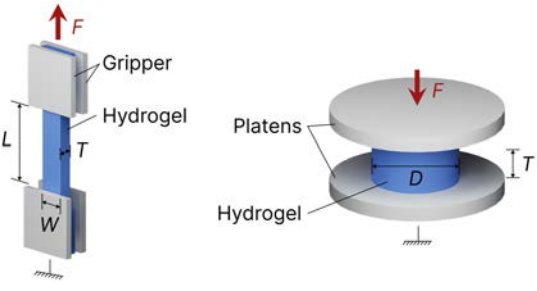

Fig. 2. Schematic diagrams of specimens used for uniaxial mechanical testing. (a) Dumbbell-shaped specimen for uniaxial tension. The two ends are secured by grippers, concentrating deformation within the central rectangular gauge section. (b) Cylinder-shaped specimen for uniaxial compression. The upper and lower surfaces are in contact with the compression platens.

dimensions must be sufficiently large to accommodate the lateral expansion of the specimen during compression.

During the test, force F and displacement δ are continuously recorded to derive nominal stress–stretch relationships. Nominal stress σ is defined as the force divided by the initial cross-sectional area A, i.e., $\sigma = F/A$. For uniaxial tension, $A = WT$, and the stretch λ is defined as the ratio of the current gauge length to the original one, i.e., $\lambda = (L + \delta)/L$. In compression, $A = \pi D^2/4$, and stretch is defined as the ratio of current to original thickness, i.e., $\lambda = (T + \delta)/T$. For further details on the stress and stretch of soft materials like hydrogels, it is recommended to refer to the textbook by Liu [2024]. Monotonic tests typically proceed until macroscopic fracture occurs, whereas cyclic tests involve repeated loading–unloading cycles to investigate hysteresis or fatigue life. Uniaxial test results may be affected by the loading velocity, depending on the specific DN gel material used. The usually adopted loading velocity reported for PAMPS/PAAm DN gels is 100 mm/min for tension and $0.1\,\text{min}^{-1}$ for compression [Jia *et al.*, 2022; Matsuda *et al.*, 2016].

2.1.2. *Deformation behaviors under uniaxial tension*

Under uniaxial tension, DN gels can exhibit diverse deformation behaviors governed by the mechanical interplay between the two constituent networks [Ahmed *et al.*, 2014; Fukao *et al.*, 2020; Lu *et al.*, 2024; Wang *et al.*, 2025d; Xin *et al.*, 2013]. By systematically varying the crosslinking density (crosslinker to monomer molar ratio) θ and monomer concentration C of two networks, You *et al.* [2025b] identified five distinct deformation modes of DN gels: (1) Brittle & Non-necking I; (2) Brittle & Necking; (3) Ductile & Necking; (4) Ductile & Non-necking; (5) Brittle & Non-necking II [Fig. 3(a)]. Figure 3(b) illustrates representative stress–strain curves for these five categories. The transition between these modes is driven by the relative dominance of the networks. When parameters (θ and C) of the first network are held constant, increasing θ or C of the second network drives a transition from (1) to (5). Conversely, when the second network is held constant, increasing the parameters of the first network reverses this trend, shifting the behavior from mode (5) back to (1) [You *et al.*, 2025b]. Among these categories, the type (3) "Ductile & Necking" DN gels with moderate θ and C for two networks are extensively studied due to their excellent ductility, fracture toughness and energy dissipation ability [Morovati *et al.*, 2020; Nakajima *et al.*, 2009, 2020; Yoshida *et al.*, 2024]. This type of DN gel is also the main subject of our subsequent discussion.

A typical deformation process and corresponding stress–stretch curve of "Ductile & Necking" DN gels under monotonic loading are shown in Figs. 4(a) and 4(b), respectively. The stress–stretch curve can be divided into three distinct regions: ① pre-necking region, ② necking region and ③ hardening region [Nakajima *et al.*, 2013; You and Liu, 2024]. These regions correspond to the morphological evolution of the specimen during loading: the pre-necking stage, the necking stage, and the hardening stage [Morovati *et al.*, 2020; Na *et al.* 2006; Zhu and Zhong, 2020].

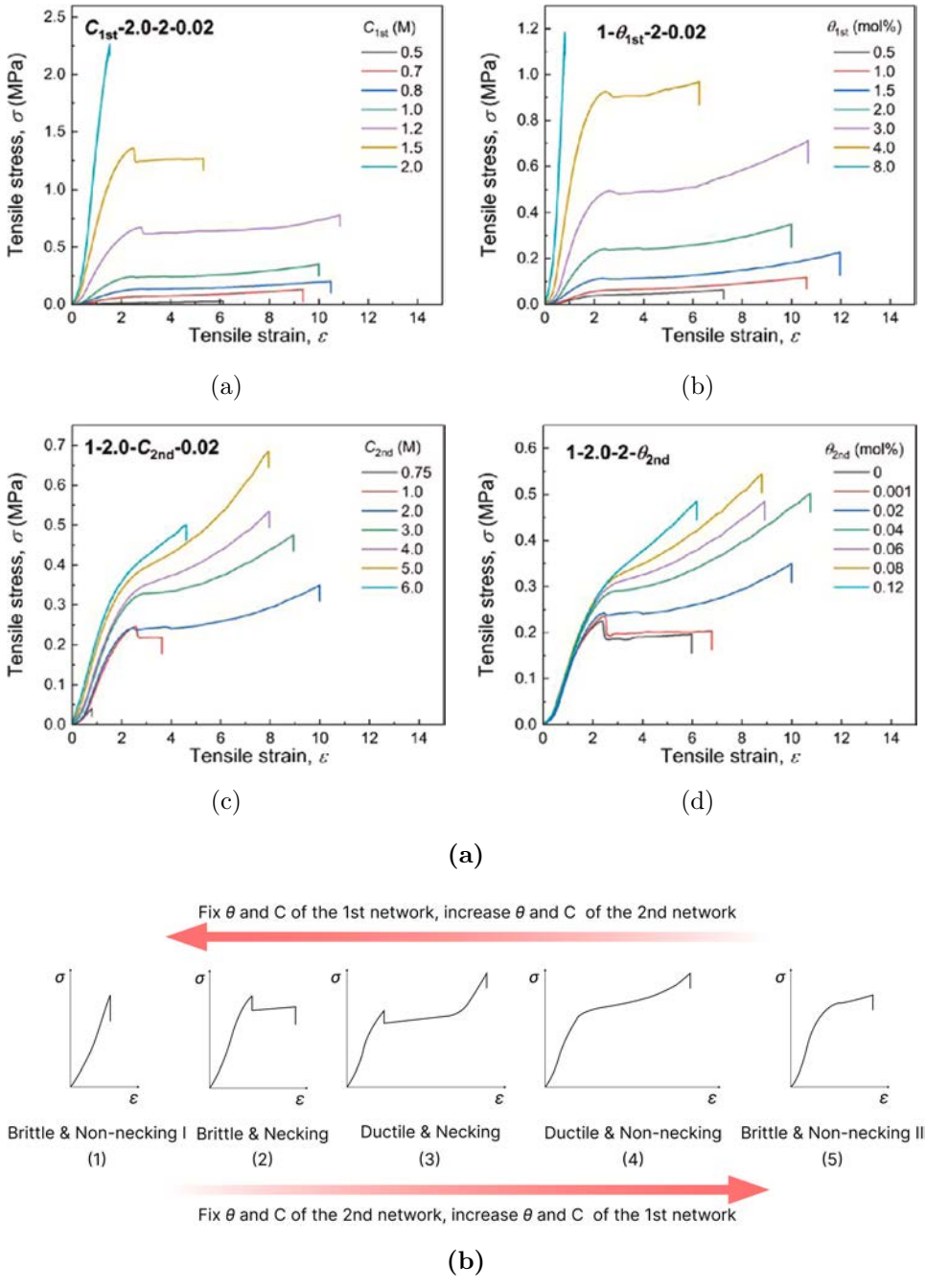

Fig. 3. Nominal stress–strain behavior of DN gels under uniaxial tension. (a) Experimental curves of DN gels with different crosslinking degrees (θ) and monomer concentration (C). (b) Five characteristic types of nominal stress–strain curve summarized from the data in (a) [You *et al.*, 2025b].

Source: Copyright 2025 Elsevier.

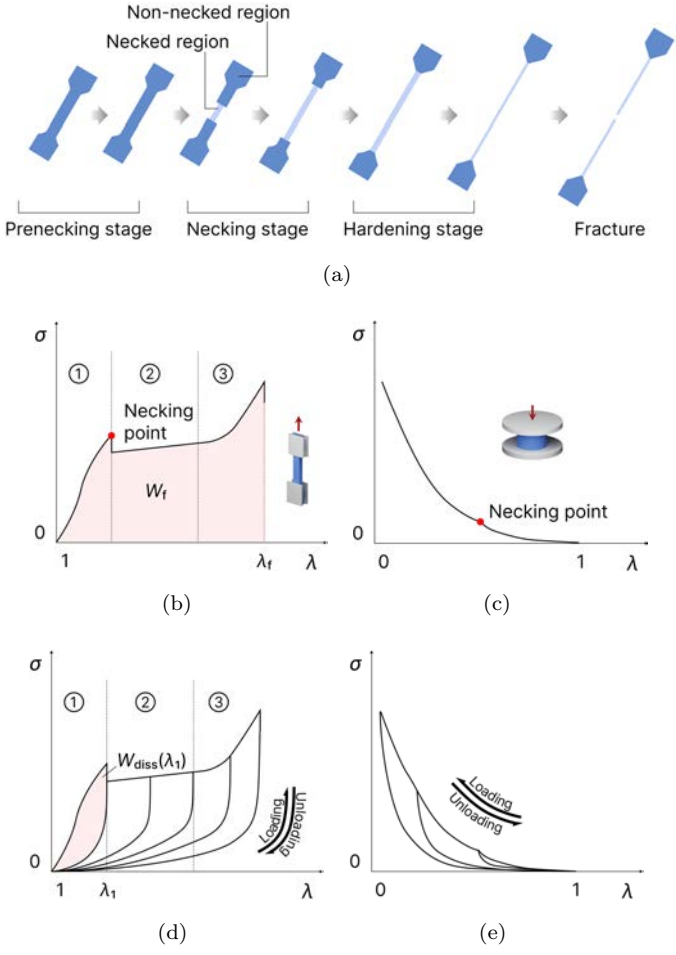

Fig. 4. (Color online) Mechanical response of DN gels under uniaxial tension and compression. (a) Schematic of deformation stages showing necked (light blue) and non-necked (dark blue) regions. (b, c) Monotonic loading curves for (b) tension and (c) compression. The work of fracture (W_f) is calculated as the area under the curve. (d, e) Cyclic loading curves for (d) tension and (e) compression. The dissipated energy density (W_{diss}) is calculated from the area within the hysteresis loop.

Source: [You and Liu, 2024]. Copyright 2024 Elsevier.

In the pre-necking stage, stress increases monotonically with stretch until the specimen reaches the necking (yield) point, defined as the transition to the necking stage. The specific yield stress and stretch are governed by both the microscopic structure and the macroscopic stress concentrations of the DN gel specimens [Yoshida *et al.*, 2024]. Specifically, a critical specimen width exists, approximately ten times the mesh size of the first network. Below this critical width, yield stress and stretch exhibit a size dependency, increasing with specimen width

and the crosslinking density of the first network, while remaining unaffected by changes in the second network concentration. Conversely, above the critical width, yielding behavior becomes width-independent and is determined intrinsically by the structure of the two networks. In this regime, increasing either the crosslinking density of the first network or the concentration of the second network enhances the yield stress and stretch [Yoshida *et al.*, 2024].

Following yield, the specimen enters the necking stage, where stress remains relatively constant (a plateau) as stretch increases. This stage is characterized by the formation of a localized necked region that is significantly softer than the surrounding material and propagates along the gauge length. Once this necked region expands throughout the entire specimen, the material enters the hardening stage, where stress rises sharply with stretch until macroscopic rupture occurs.

Under uniaxial compression, the nominal stress of DN gels increases monotonically as the stretch decreases, as shown in Fig. 4(c). A yield point is often observed, typically defined as the inflection point of the nominal stress–stretch curve. Ideally, uniaxial compression can be considered equivalent to equibiaxial extension in the plane perpendicular to the loading axis; thus, compression data can be converted to represent equibiaxial tensile behavior [Matsuda *et al.*, 2016; Webber *et al.*, 2007]. However, compared to tensile studies, investigations into the compressive behavior of DN gels are less common. This scarcity is likely attributed to experimental challenges that make detecting the precise macroscopic failure point in compression difficult [Tsukeshiba *et al.*, 2005; Xiao *et al.*, 2013], and data scatter can be significant if interfacial friction is not effectively eliminated.

When subjected to cyclic loading, DN gels display prominent hysteresis loops. A characteristic feature of this behavior is that the reloading curve almost completely overlaps with the preceding unloading curve, indicating significant stress softening (Mullins effect), as shown in Figs. 4(d) and 4(e) for tension and compression, respectively [Jia *et al.*, 2022; Webber *et al.*, 2007].

Together, monotonic and cyclic stress–stretch curves provide a comprehensive framework for characterizing the mechanical properties of the DN gels, including elastic modulus, work of fracture, and energy dissipation ability. In the following sections, we define and discuss these mechanical properties in detail.

2.1.3. *Elastic modulus measured under uniaxial tension or compression*

The elastic modulus constitutes a fundamental mechanical parameter of DN gels. Data obtained from monotonic loading curves can yield two distinct metrics: the initial elastic modulus (E_{initial}) and the tangent modulus (E_{tangent}).

Initial elastic modulus is defined as the ratio of stress to strain within the linear elastic region of the material, typically at very small strains [Lin *et al.*, 2010]. It reflects the material's resistance to elastic deformation during the nascent stages of loading. Two primary methods are employed to determine E_{initial}. The first method involves directly calculating the slope of the stress–stretch curve within a small

strain range (e.g., <5%), applicable to both tension and compression. The second method involves fitting the nominal stress–stretch data to hyperelastic constitutive models, such as the Neo-Hookean or Mooney–Rivlin models [Mooney, 1940]. The initial modulus of typical PAMPS/PAAm DN gels measured by these two methods is on the same order of 0.1 MPa [Tsukeshiba *et al.*, 2005; Zhang *et al.*, 2018]. It is worth noting that although the second method may yield a larger standard deviation, the resulting modulus often provides better predictiveness for deformation at larger stretches compared to the first method. Beyond uniaxial testing, the initial elastic modulus can also be indirectly determined via pure shear tests and rheological measurements, which will be discussed in Secs. 2.2 and 2.7, respectively. Furthermore, atomic force microscopy (AFM) and indentation techniques allow for the measurement of local moduli of DN gels at the microscale [Tanaka *et al.*, 2008]; however, we will not elaborate in detail here.

Tangent modulus is defined as the instantaneous slope of the stress–stretch curve at a specific deformation point under monotonic loading, expressed as [You and Liu, 2024]

$$E_{\text{tangent}} = \frac{\mathrm{d}\sigma}{\mathrm{d}(\lambda - 1)}, \tag{2.1}$$

where E_{tangent} describes the material's resistance to further deformation at a given stretch and serves as a critical parameter for characterizing mechanical nonlinearity. By analyzing the evolution of E_{tangent} and E_{initial} of DN gels during the pre-necking stage of cyclic loading, You and Liu [2024] partitioned the strain energy density to elucidate the underlying toughening mechanisms of DN gels. It is noteworthy that the definition of tangent modulus parallels the concept of the incremental modulus for hydrogels proposed by Liu *et al.* [2011], which was specifically developed to investigate instability patterns arising from the swelling of hydrogel beam and film structures in their work.

2.1.4. *Work of fracture*

The work of fracture, W_f, represents the total strain energy density required to rupture a material. It typically carries a unit of $\mathrm{J/m^3}$, which is calculated by integrating the area under the nominal stress–stretch curve obtained from uniaxial tension testing [Fig. 3(b)]:

$$W_f = \int_1^{\lambda_\mathrm{f}} \sigma \mathrm{d}\lambda, \tag{2.2}$$

where λ_f denotes the stretch to rupture (also termed stretchability), and the corresponding peak stress, $\sigma_{\max}$, defines the tensile strength. As reported, DN gels can exhibit exceptional tensile strength of around 0.68 MPa and compression strength of around 17.2 MPa, with corresponding stretchability of around 15 in tension and 0.92 in compression [Gong *et al.*, 2003]. Consequently, W_f for typical DN gels is usually on the order of 10^6 $\mathrm{J/m^3}$ [Jia *et al.*, 2022; Zhou *et al.*, 2021].

2.1.5. *Energy dissipation*

During deformation, the rigid first network of DN gels undergoes irreversible fracture, resulting in significant energy dissipation. This mechanism is considered the primary contributor to DN gels' exceptional toughness. Quantitatively, this property is assessed via the dissipated energy density, W_{diss}, which is defined as the area enclosed by the hysteresis loop during a single loading–unloading cycle. Take cyclic tension as an example [Fig. 4(d)], where the specimen is loaded from an initial stretch of 1 to a maximum stretch of λ_1 and subsequently unloaded, W_{diss} is calculated as [Lu *et al.*, 2025; Qi *et al.*, 2024; You *et al.*, 2025b; Zheng and Gong, 2025]

$$W_{\text{diss}}(\lambda_1) = \int_0^{\lambda_1} \sigma^+(\lambda)\mathrm{d}\lambda - \int_0^{\lambda_1} \sigma^-(\lambda)\mathrm{d}\lambda, \tag{2.3}$$

where $\sigma^+(\lambda)$ and $\sigma^-(\lambda)$ denotes the nominal stresses during the loading and unloading paths, respectively. This equation is also applicable to cyclic compression [Webber *et al.*, 2007].

To analytically characterize W_{diss} of DN gels, Brown [2007] and Tanaka [2007] proposed cyclic models based on the assumption of a linear stress–stretch relationship during unloading. Long and Hui [2016] later refined these models by introducing a bilinear approximation for the unloading path, an approach that has been widely accepted. However, these earlier studies were limited to the pre-necking and necking stages of deformation. Recently, You *et al.* [2025b] bridged this gap by establishing a correlation between monotonic loading behavior and W_{diss} across the entire deformation spectrum. However, the theoretical characterization of W_{diss} under other loading conditions still needs to be explored.

2.2. *Pure shear test*

The pure shear test constitutes a pivotal experimental technique for characterizing the mechanical properties of DN gels. This test method is originally established to determine the fracture energy of rubbers [Lake and Thomas, 1967; Rivlin and Thomas, 1953], while with development, this method has been extensively adapted to quantify the fracture toughness (also termed fracture energy) [Kolvin *et al.*, 2018; Li *et al.*, 2014; Zheng *et al.*, 2024a; Zhuo *et al.*, 2023], and many other mechanical properties including the elastic modulus, fatigue behavior, fractocohesive length, etc., of DN gels [Bai *et al.*, 2017, 2019a; Li *et al.*, 2024c; Zhang *et al.*, 2018]. Furthermore, it can be used for investigating the unique crack growth behavior of DN gels [Zhang *et al.*, 2022].

2.2.1. *Specimen geometry and basic definitions*

Specimens employed in pure shear tests are usually rectangular thin sheets with a geometry satisfying $L \geqslant 5H$ and $c \gg H \gg T$ [Rivlin and Thomas, 1953], either

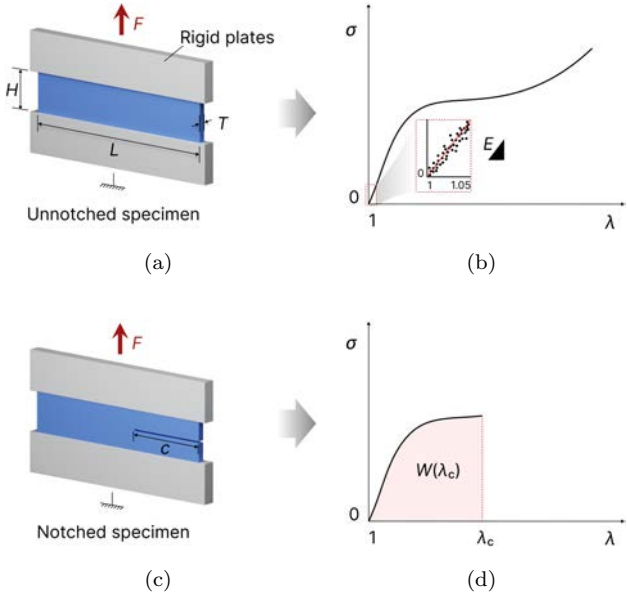

Fig. 5. Schematic diagrams of specimen geometries and typical curves for pure shear testing. (a, b) Unnotched specimen (a) and its corresponding nominal stress–stretch curve (b). (c, d) Notched specimen (c) and its corresponding nominal stress–stretch curve (d).

with or without a notch of c in the middle of the height. Here, L, H, and T refer to the initial length, gauge height, and thickness of a specimen for the interest of the test, respectively [Figs. 5(a) and 5(c)]. This geometry configuration is designed to enable the translational invariance of the stress and strain field as the crack propagates [Long and Hui, 2016].

Pure shear tests are usually conducted using a universal testing machine. Prior to testing, the specimen is clamped along the length direction with rigid plates, and then the upper gripper of the testing machine moves up vertically at a constant velocity. Throughout the test, the force F and displacement δ are continuously recorded to derive the nominal stress–stretch curve. The nominal stress, σ, is defined as the force normalized by the initial cross-sectional area A ($A = LT$), i.e., $\sigma = F/A$. The stretch, λ, is calculated as the ratio of the current test height, h, to the original gauge height, i.e., $\lambda = h/H$.

2.2.2. *Elastic modulus measured by pure shear testing*

A typical nominal stress–stretch curve for an unnotched DN gel specimen under pure shear is shown in Fig. 5(b). As displacement increases, the nominal stress increases, plateaus, and increases again, before dropping abruptly upon rupture. Analogous to uniaxial testing, the initial elastic modulus E under a pure shear test is determined by linear fitting the nominal stress–stretch data within the regime of $1 < \lambda < 1.05$.

Note that, unlike uniaxial tension, where the measured initial elastic modulus approximates three times the shear modulus μ (i.e., $E_{\text{initial}} = 3\mu$), the measured initial elastic modulus under pure shear test is four times the shear modulus [Yang *et al.*, 2019]:

$$E = 4\mu. \tag{2.4}$$

Typically, μ of DN gels ranges from 10 kPa to 100 kPa [Nakajima *et al.*, 2013; Zhang *et al.*, 2018].

2.2.3. *Fracture toughness measured by pure shear testing*

To determine fracture toughness, both notched and unnotched specimens are subjected to pure shear loading. For a notched specimen with an initial crack length c, the measured nominal stress–stretch profile overlaps with that of the unnotched counterpart until the onset of macroscopic crack propagation, which occurs at a critical stretch λ_c [Figs. 5(c) and 5(d)]. Fracture toughness (Γ), defined as the material's resistance to crack growth, is calculated by integrating the area under the nominal stress–stretch curve of the unnotched specimen up to λ_c to get the strain energy density $W(\lambda_c)$, multiplied by the initial gauge height H:

$$\Gamma = W(\lambda_c)H = \int_1^{\lambda_c} \sigma(\lambda)\mathrm{d}\lambda H. \tag{2.5}$$

The fracture toughness of DN gels measured via this method typically ranges from 10^3 J/m^2 to 10^4 J/m^2 [Li *et al.*, 2014; Zheng *et al.*, 2024a]. To elucidate the mechanistic origins of this toughness, Γ is generally decomposed into two parts:

$$\Gamma = \Gamma_0 + \Gamma_d, \tag{2.6}$$

where Γ_0 denotes the intrinsic fracture energy, representing the energy required to break polymer chains crossing the crack plane per unit area [Lake and Thomas, 1967], and Γ_d denotes the dissipated energy, representing the energy dissipated through bulk hysteresis in the damage zone around the crack tip [Zhao, 2014]. Based on this, Zhang *et al.* [2015] developed a method to determine Γ_0. By pre-stretching a specimen to near the rupture limit and then unloading it, the dissipative component Γ_d can be effectively eliminated before the fracture test. Using this method, the measured Γ_0 of DN gels is around 400 J/m^2.

2.2.4. *Fractocohesive length*

With this fracture toughness Γ measured from pure shear tests and work of fracture W_f obtained from uniaxial tensile tests mentioned in Sec. 2.1.4, we can define a critical characteristic length known as the fractocohesive length l_f:

$$l_f = \frac{\Gamma}{W_f}. \tag{2.7}$$

This length scale characterizes the size of the region within which the stress concentration is effectively screened by the dissipative process [Jia *et al.*, 2022;

Long *et al.*, 2021; Zheng *et al.*, 2021]. Conventional SN gels typically exhibit l_f on the order of 1 mm [Yang *et al.*, 2019], while for DN gels, this value can exceed 10 mm [Jia *et al.*, 2022; Long *et al.*, 2021]. Note that Eq. (2.7) only represents a scaling estimate. More accurate considerations of a prefactor are required if more quantitative estimates are of interest.

2.2.5. *Fatigue behavior measured by pure shear testing*

The fatigue behavior of a material usually includes two phenomena: fatigue damage and fatigue fracture. Fatigue damage refers to the degradation of mechanical properties under cyclic loading, e.g., modulus reduction, whereas fatigue fracture denotes the macroscopic rupture of the material under cyclic loads. Both phenomena of DN gels are usually characterized by pure shear tests. Unlike quasi-static tests mentioned above, fatigue tests are time-intensive and usually take at least 1 day. Thus, it is necessary to introduce a humidity maintenance apparatus during the test to prevent specimen dehydration. A widely adopted solution is to use a homemade acrylic chamber equipped with a humidifier to maintain a high humidity surrounding the specimen [Figs. 6(a), 6(c)] [Bai *et al.*, 2017; Zhang *et al.*, 2018].

To characterize fatigue damage of DN gels, unnotched pure shear specimens are subjected to cyclic loading with a triangular profile at a fixed frequency (e.g.,

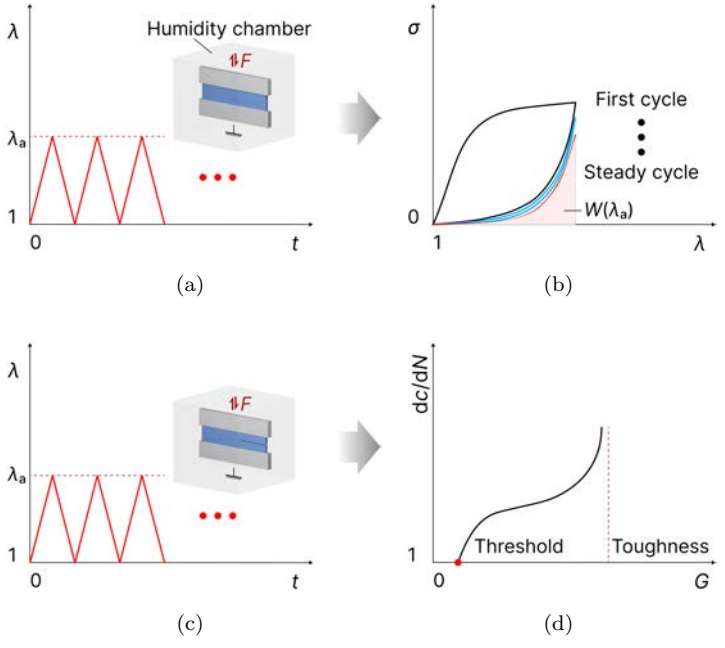

Fig. 6. Cyclic pure shear testing for fatigue analysis. (a, b) Cyclic triangular loading profile applied to an unnotched specimen (a) and the corresponding nominal stress–stretch curve (b). (c, d) Cyclic triangular loading profile applied to a notched specimen (c) and the steady-state crack extension per cycle ($\mathrm{d}c/\mathrm{d}N$) plotted as a function of the energy release rate (G) (d).

0.25 Hz) [Bai *et al.*, 2017; Zhang *et al.*, 2018] [Fig. 6(a)]. A typical nominal stress–stretch curve reveals that the peak stress at the applied stretch amplitude λ_a decreases over successive cycles [Fig. 6(b)]. The hysteresis loop is pronounced in the first cycle but diminishes rapidly in subsequent cycles. Eventually, the stress–stretch response stabilizes, a phenomenon termed shakedown. For DN gels, the shakedown typically occurs after 2000 loading–unloading cycles.

Fatigue fracture properties, specifically the fatigue threshold, are determined using notched pure shear specimens [Bai *et al.*, 2017, 2019a; Li *et al.*, 2024b; Tang *et al.*, 2017; Zhang *et al.*, 2018] [Fig. 6(c)]. Specimens are cyclically stretched to various maximum amplitudes, λ_a, using the same frequency as in damage tests. The crack extension, δc, is monitored via a digital camera and plotted against the number of cycles, N. Usually, crack propagation develops rapidly during the initial cycles but decelerates to a steady state afterwards, correlating with the shakedown of DN gels during the fatigue damage test. For most cases, after about 2000 cycles, δc increases linearly with N, meaning that the crack extension reaches a steady state. In this condition, the applied energy release rate G for a given λ_a is calculated by integrating the loading curve of the unnotched specimen up to λ_a to get the strain energy density $W(\lambda_a)$, and then multiplied by the initial gauge height of the specimen, i.e., $G = W(\lambda_a)H$ [Bai *et al.*, 2017; Rivlin and Thomas, 1953; Zhang *et al.*, 2018]]. Different applied stretches λ_a result in different applied energy release rates G. By plotting the steady-state crack extension per cycle, i.e., $\mathrm{d}c/\mathrm{d}N$, as a function of G, the fatigue threshold Γ_0 is determined as the intercept of the curve on the G axis when $\mathrm{d}c/\mathrm{d}N = 0$ via linear regression [Fig. 6(d)].

The fatigue threshold defines the critical energy release rate below which the crack will not propagate under infinite cycles of loads. A material is more fatigue fracture resistant with a higher fatigue threshold. The fatigue threshold of DN gels is often on the order of $100\,\mathrm{J/m^2}$ [Bai *et al.*, 2017; Zhang *et al.*, 2018], which is approximately one order of magnitude lower than their fracture toughness. Researchers also studied the effect of network components on the fatigue threshold and found that fatigue threshold depends on the long-chain polymer network, but negligibly on the short-chain polymer network [Bai *et al.*, 2017; Zhang *et al.*, 2019b].

When the DN gel is loaded above its fatigue threshold, the slope of $\mathrm{d}c/\mathrm{d}N$ versus G determines how fast the crack grows over the loading cycles, and it serves as another indicator of fatigue fracture properties. The smaller the slope, the better the fatigue fracture resistance. DN gels exhibit superior fatigue fracture resistance compared to conventional SN gels in terms of both parameters [Bai *et al.*, 2017].

2.2.6. *Crack growth behavior*

While the standard pure shear tests discussed previously utilize specimens with pre-existing notches, a modified protocol has been developed to investigate fracture dynamics by introducing a notch into a specimen already subjected to high tension [Kolvin *et al.*, 2018; Zhang *et al.*, 2022] [Fig. 7(a)]. This method characterizes the

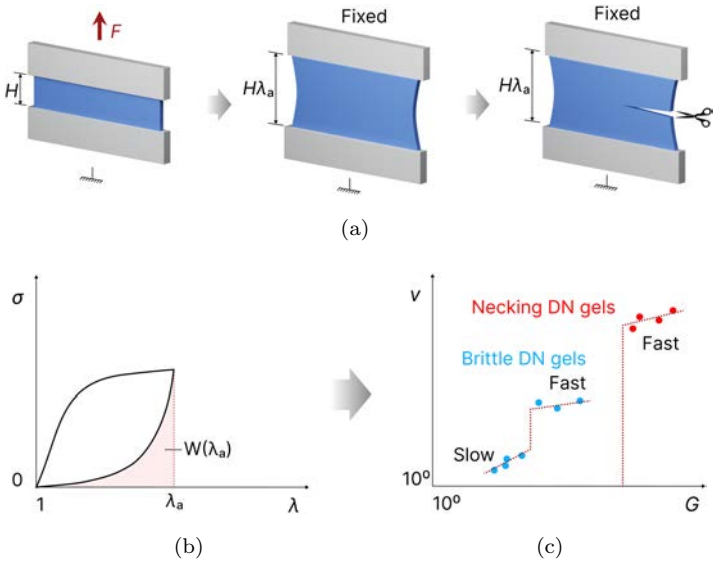

Fig. 7. Schematic illustration of the crack growth experiment and data analysis. (a) Test procedure showing the original pure shear specimen, the specimen with a specified stretch of λ_a, and the introduction of a notch after the stretch. (b) Determination of the strain energy density ($W(\lambda_a)$) for energy release rate calculations. (c) Crack growth velocity (v) plotted as a function of the applied energy release rate (G).

dynamic fracture behavior of DN gels and offers a more practical meaning, as such a post-notch can be inserted by accidental puncture or impact damage during service.

In this test, the DN gel specimen is first stretched to a certain stretch λ_a and then unloaded to a stretch of 1. The driving force for fracture (i.e., applied energy release rate G), is calculated by integrating the unloading part of the nominal stress–stretch curve of the unnotched specimen within the stretch range from 1 to λ_a to get the strain energy density $W(\lambda_a)$ [Fig. 7(b)], and then multiply it by the initial test height of the specimen, i.e., $G = W(\lambda_a)H$. Afterward, a long cut is introduced at one edge of the specimen in the center using sharp scissors, and the subsequent crack propagation is recorded by a high-speed camera. By analyzing the acquired images, the crack propagation process can be extracted, and the time profiles of the crack length can be obtained. Based on these data, the crack growth velocity can be plotted as a function of the applied energy release rate [Fig. 7(c)].

Research reveals distinct behaviors based on the DN gel formulation. Brittle DN gels exhibit a transition from a slow mode (quasi-stationary fracture) to a fast mode (dynamic fracture) as G increases, analogous to conventional SN gel. In contrast, necking DN gels only exhibit fast modes once G exceeds a critical threshold. This phenomenon indicates that for necking DN gels, the formation of a large damage zone creates a substantial energy barrier to crack initiation. However, once this barrier is surmounted, the excess energy release accelerates the crack propagation, resulting in dynamic fracture [Zhang *et al.*, 2022].

2.3. *Single-edge notch test*

The single-edge notch test, originally established by Greensmith to determine the fracture toughness of rubbers [Greensmith, 1963], has been recently adapted to study the fracture and flaw sensitivity of DN gels [Zhou *et al.*, 2021].

2.3.1. *Specimen geometry and basic definitions*

Single-edge notch test employs rectangular-shaped specimens where the width W is much smaller than the gauge length L, i.e., $W \ll L$. A small notch with a length of c is introduced at the midpoint of one edge along the length direction, satisfying $c \ll W$ [Fig. 8(a)]. Representative specimen dimension reported in the literature has a gauge length of 25 mm, a width of 4 mm, a thickness of 1.5 mm, and a notch length of 1 mm [Matsuda *et al.*, 2021].

For the characterization of flaw sensitivity, specimens with notches of varying lengths within 1/4 of the specimen width are prepared. The long notches can be introduced using cutting dies or razor blades, while small notches can be introduced

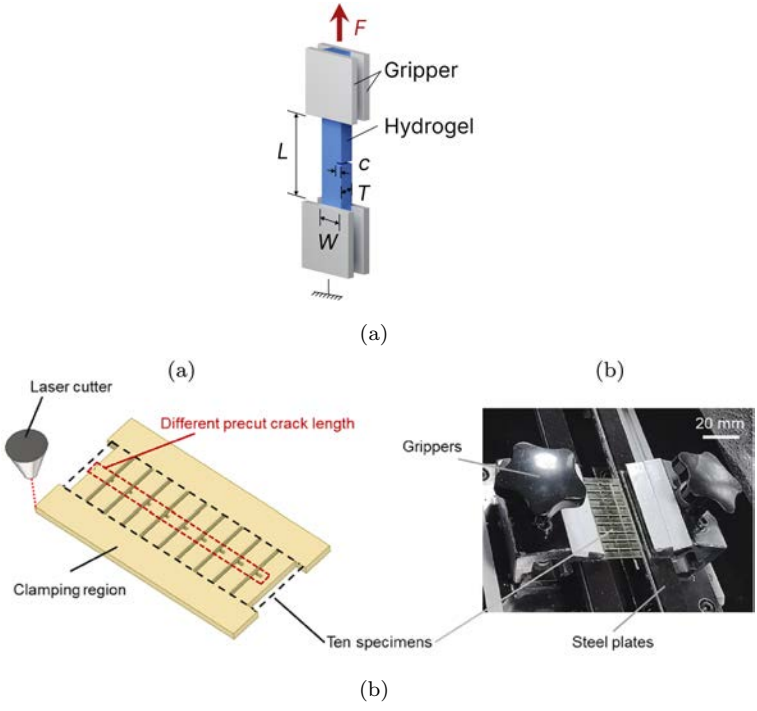

Fig. 8. Experimental setups for single-edge notch testing. (a) Geometry of the rectangular specimen used for testing. (b) Schematic and photograph of a high-throughput experimental system. Ten specimens with varying notch lengths are mounted in parallel on shared grippers for simultaneous testing [Liu *et al.*, 2024].

Source: Copyright 2024 Elsevier.

using the femtosecond laser [Chen *et al.*, 2017; Sun *et al.*, 2024; Zhou *et al.*, 2021]. The loading protocol follows the uniaxial tension test described in Sec. 2.1, with nominal stress and stretch definitions remaining analogous.

The single-edge notch test can characterize the fracture toughness and flaw sensitivity of DN gels with minimal material, making it especially suitable for scenarios where limited material or space is available, such as high-throughput experiments [Fig. 8(b)] [Liu *et al.*, 2024].

2.3.2. *Fracture toughness measured by single-edge notch testing*

As mentioned before, fracture toughness quantifies a material's resistance to crack growth. The fracture toughness measured by single-edge notch tests can be determined as the critical energy release rate at the onset of the crack growth as follows:

$$\Gamma = 2kW(\lambda_c)c = \frac{6}{\sqrt{\lambda_c}}W(\lambda_c)c, \tag{2.8}$$

where k is an empirical correction factor of $3\lambda_c^{-1/2}$ [Ducrot *et al.*, 2014], λ_c is the critical stretch at which the crack propagates, $W(\lambda_c)$ is the strain energy density stored in the specimen, which can be obtained from the nominal stress–stretch curve of the unnotched specimen of identical dimensions, similar to Eq. (2.5). Note that the accuracy of measured fracture toughness may be compromised when using a relatively small notch length due to its proximity to the flaw-sensitivity length of the materials. Thus, measurements are typically performed across a range of notch lengths. The resulting fracture toughness will first increase with the notch length and then reach a plateau. The notch length-independent fracture toughness is obtained by averaging these plateau values [Liu *et al.*, 2024; Sun *et al.*, 2024].

The single-edge notch test has some limitations worth highlighting. First, the equation used above is valid only for small notch lengths and crack propagation occurred at small to moderate strains; otherwise, Eq. (2.8) may underestimate the fracture toughness [Long and Hui, 2016; Matsuda *et al.*, 2021]. Second, it works well with materials that obey the Mooney–Rivlin model [Greensmith, 1963], while its applicability to DN gels that usually undergo necking and hardening at large deformations still needs further verification.

2.3.3. *Fatigue behavior measured by single-edge notch testing*

The characterization of fatigue properties, including fatigue damage and fatigue fracture, using the single-edge notch test follows protocols analogous to the pure shear test mentioned in Sec. 2.2.5, with the primary distinction lying in the calculation of the applied energy release rate. For a notched sample under the Nth loading

cycle with applied stretch λ_a, the applied energy release rate is calculated as

$$G(\lambda_a, N) = \frac{6}{\sqrt{\lambda_a}} W(\lambda_a, N) c(N), \tag{2.9}$$

where c is the current notch length in the undeformed configuration, and $W(\lambda_a, N)$ is the strain energy density of the unnotched specimen at the Nth cycle:

$$W(\lambda_a, N) = \int_1^{\lambda_a} \sigma \mathrm{d}\lambda, \tag{2.10}$$

where σ and λ are the measured nominal stress and stretch, respectively. By systematically varying λ_a, the crack extension per cycle versus the applied energy release rate, i.e., $\mathrm{d}c/\mathrm{d}N$ versus G, can be obtained. The fatigue threshold Γ_0 is estimated by linearly extrapolating the $\mathrm{d}c/\mathrm{d}N$ versus G curve to the intercept with the abscissa.

2.3.4. *Flaw sensitivity*

Flaw sensitivity length reflects the sensitivity of a material to flaws, and it can be characterized by the flaw sensitivity length c_c. Figure 9 shows magnified schematic diagrams of the crack tip region of single-edge notched specimens. As shown in the

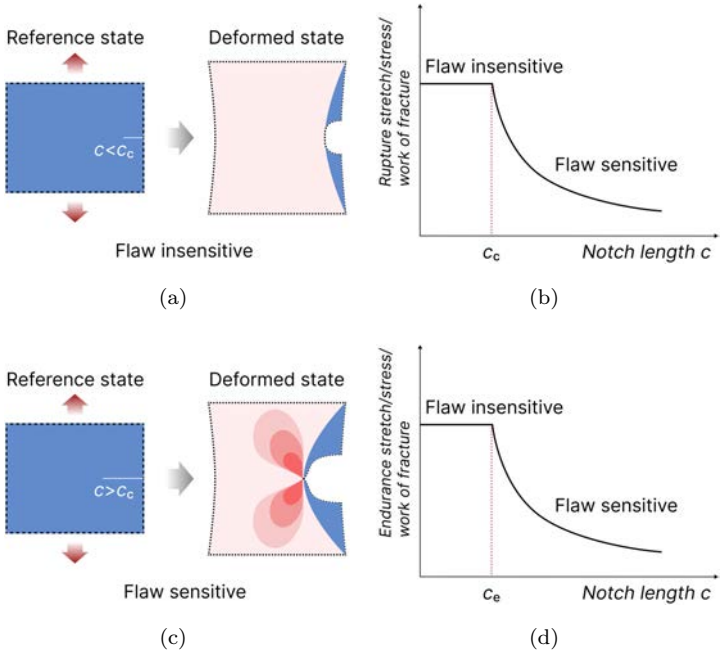

Fig. 9. Schematic illustration of flaw sensitivity transitions. (a) Flaw-insensitive behavior ($c < c_c$) showing uniform stress distribution ahead of the crack tip. (b) Flaw-sensitive behavior ($c > c_c$) showing stress concentration at the crack tip. (c) Rupture limits (stress, stretch and work of fracture) versus notch length c. The flaw sensitivity length c_c is defined by the transition point where these limits drastically decrease. (d) Endurance limits versus notch length c. Similarly, the endurance flaw sensitivity length c_e is defined by the point of abrupt reduction.

figure, when the flaw length is smaller than c_c, the material exhibits uniform stress distribution during loading until rupture [Fig. 9(a)]. When the flaw is larger than c_c, the material exhibits stress concentration at the crack tip [Fig. 9(b)], which leads to the reduction of mechanical properties, including the strength, stretchability and work of fracture.

The flaw sensitivity length can be experimentally determined by measuring the rupture parameters (i.e., rupture stretch, stress or work of fracture) as a function of notch length [Ma *et al.*, 2024; Sun *et al.*, 2024; Zhou *et al.*, 2021]. When the notch length is smaller than a critical length, these parameters are independent of the notch length; when the notch length is larger than this critical length, these parameters decrease with the notch length [Fig. 9(c)]. This critical length yields the flaw sensitivity length c_c. Theoretically, c_c scales with the fractocohesive length Γ/W_f mentioned in Sec. 2.2.4, and can be determined through

$$c_c = \frac{1}{k}\frac{\Gamma}{W_f}, \tag{2.11}$$

where Γ is the notch length-independent fracture toughness of DN gels, which can be obtained using specimens with long notches through various methods, including the single-edge notch test mentioned above, or pure shear test, etc., and W_f is the work of fracture measured using unnotched specimens through the uniaxial tension test. For an edge-cracked specimen with the simplicity of linear elasticity, $k = 2\pi(1.122)^2$ [Tada *et al.*, 2000; Zhou *et al.*, 2021]. For DN gels with Γ on the order of $10^3\,\mathrm{J/m^2}$ and W_f on the order of $10^6\,\mathrm{J/m^3}$, c_c is approximately on the order of 0.1 mm.

The concept of flaw sensitivity can also extend to cyclic loading, denoted as the endurance flaw sensitivity length (c_e). It identifies the critical notch length at which endurance limit (rupture stretch, stress or work of fracture) exhibits an abrupt reduction [Fig. 9(d)]. Similarly, c_e is calculated as

$$c_e = \frac{1}{k}\frac{\Gamma_0}{W_e}, \tag{2.12}$$

where Γ_0 is the fatigue threshold measured using specimens with long notches, W_e is the endurance work of fracture measured using specimens without notches. Γ_0/W_e is termed the endurance fractocohesive length [Zhou *et al.*, 2021]. For DN gels with Γ_0 on the order of $10^2\,\mathrm{J/m^2}$ and W_e on the order of $10^5\,\mathrm{J/m^3}$, c_e is also approximately on the order of 0.1 mm.

The flaw sensitivity of DN gels can also be measured by conducting pure shear tests; the process is similar to that described here [Ma *et al.*, 2024; Yang *et al.*, 2019]. The flaw sensitivity of typical PAAm hydrogel is usually on the order of 1 mm [Chen *et al.*, 2017; Yang *et al.*, 2019], however, according to existing studies, DN gels do not exhibit any advantage in terms of flaw sensitivity.

2.4. *Trouser tear test*

Analogous to the pure shear test, the trouser tear test was originally established for characterizing the fracture of rubber and elastomers before being adapted for

hydrogels in recent years. However, its application to traditional SN gels is often limited by the "stick–slip" effect, a phenomenon characterized by large fluctuations in force data due to unstable crack propagation during tearing. In contrast, DN gels typically exhibit stable tearing behavior with negligible stick-slip effect. Furthermore, the crack propagation velocity during tearing is directly controlled by the loading velocity [Bai *et al.*, 2019a]. Thus, the trouser tear test has emerged as a prevalent experimental method for studying the fracture properties, especially fracture toughness and the damage zone, of DN gels.

2.4.1. *Specimen geometry and basic definitions*

The specimens used for the trouser tear test are rectangular-shaped, with a length of L, width of $2w$, and thickness of t. A pre-crack of length c is introduced at the width edge [Fig. 10(a)], creating two arms. For reference, L, w, t and c could be 70, 15, 1.5 and 15 mm, respectively [Jia *et al.*, 2022]. During testing, the two arms are secured in opposing grippers of a universal testing machine. One arm moves upward at a constant velocity while the other remains fixed [Fig. 10(b)]. Considering that the deformation of the two arms may affect the measured tear force, two

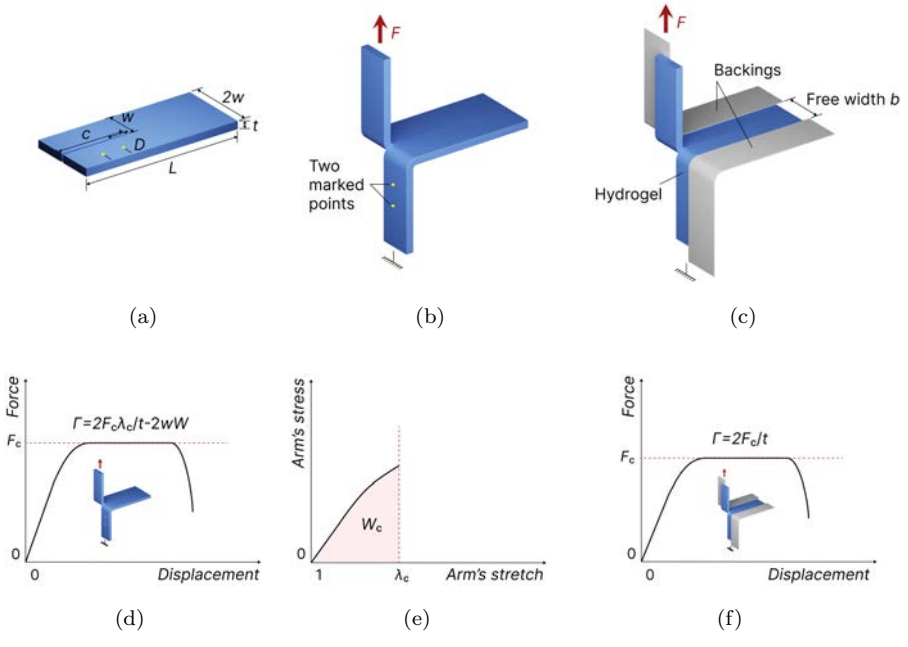

Fig. 10. Experimental setups and results for trouser tear tests. (a) Specimen geometry. (b) Conventional trouser tear test setup. The two arms are secured in opposing grippers, and arm deformation is measured by tracking the distance between two marked points. (c) Modified trouser tear test setup. Inextensible backings are adhered to arms with a separation distance b. (d) Typical tearing curve from the conventional test. (e) Determination of the arm's strain energy density W_c during steady-state crack propagation. (f) Typical tearing curve from the modified test.

points with an initial distance of D are marked on one arm before the test for the characterization of the contribution of the deformed arms [Matsuda *et al.*, 2021]. The force and distance between two marked points on the arm during deformation are recorded.

Recently, Jia *et al.* [2022, 2023] modified this trouser tear test by introducing backings onto the specimen surfaces [Fig. 10(c)]. The backings are usually flexible and inextensible tapes with a thickness of around 100 μm, and the distance between two backings determines the "free width" b. These backings avoid the elongation of arms during tearing, thus no need to quantify their deformation, and by adjusting the free width b, the damage zone at the tear front can also be controlled. The details of this test will be described in subsequent sections.

2.4.2. *Derivation of fracture toughness during tearing*

During a trouser tear test, the crack tip undergoes deformation primarily through out-of-plane shear, combined with local tension [Long and Hui, 2016]. As the test proceeds, the tear force increases initially before reaching a steady-state plateau, denoted as F_c, as the crack propagates [Fig. 10(d)]. Due to the deformability of hydrogels, the arms of the specimen stretch during testing. The stretch in the arm, λ_a, can be calculated as $\lambda_a = d/D$, where d is the current distance between marker points that can be obtained from the non-contact video extensometer and D is their initial distance [Matsuda *et al.*, 2021]. The fracture toughness is calculated accounting for the work done by the external force and the elastic energy stored in the deformed arms [Long and Hui, 2016; Rivlin and Thomas, 1953]:

$$\Gamma = \frac{2F_c\lambda_a}{t} - 2wW_a, \tag{2.13}$$

where W_a is the average strain energy density of the arm when the crack propagation reaches a steady state, which can be determined by stretching an arm strip to λ_c [Fig. 10(e)].

To simplify the measurement of fracture toughness, [Jia *et al.*, 2022] introduced backings on two arms of the specimen used for trouser tear tests [Fig. 10(c)]. With the constraint of backings, the deformation of two arms is suppressed, and λ_c and W_c can be approximated to 1 and 0, respectively. Therefore, the fracture toughness in this case can be simplified to [Fig. 10(f)]:

$$\Gamma = \frac{2F_c}{t}. \tag{2.14}$$

A critical parameter in the modified trouser tear test is the "free width" b between two arms. This width spatially confines the damage zone at the tear front [Jia *et al.*, 2022] [Fig. 11(a)]. Jia *et al.* [2022] demonstrated that for PAMPS/PAAm DN gels, the measured fracture toughness is sensitive to this confinement. As b increases from 0 mm to 10 mm, the measured fracture toughness rises before stabilizing at a plateau value of approximately $3600\,\mathrm{J/m^2}$ [Fig. 11(b)]. This plateau

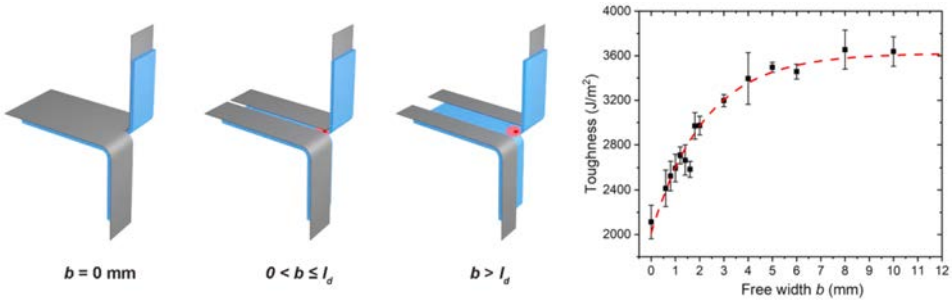

(a) (b)

Fig. 11. Dependence of fracture toughness on the free width b. (a) Schematic illustration of the dissipation zone at the crack tip of DN gels for varying free widths b. The parameter l_d denotes the characteristic size of the damage zone. (b) Measured fracture toughness of DN gels plotted as a function of the free width b [Jia *et al.*, 2022].

Source: Copyright 2022 Elsevier.

fracture toughness Γ_c should be comparable to that measured by DN gel specimens without backings. The results also remind us that the width of the DN gel specimen used for the trouser tear test should be large enough, or the measured fracture toughness would be specimen-size dependent.

Bai *et al.* [2019a] also used the trouser tear test to measure the fracture toughness of PAAm-Ca-alginate hydrogels. In their experiment, they introduced backings on both the top and bottom surfaces of DN gel specimens to suppress the deformation of the arms and guide the crack path during tearing, while the distance between backings was unknown. According to their experimental results, the measured fracture toughness of DN gels was influenced by both the specimen thickness and the tear velocity. For DN gels with the same tear velocity, increasing the thickness may result in the fracture toughness increasing at first and finally reaching a plateau when the thickness exceeds a critical value, due to the transition from small-scale inelasticity to large-scale inelasticity [Fig. 12(a)]. For DN gels with the same thickness, increasing the tear velocity may also increase the fracture toughness, as the size of the inelastic zone increases as the tear velocity increases [Fig. 12(b)]. When the velocity vanishes, the fracture toughness reaches a threshold. This threshold depends on the concentration of calcium and may exhibit a thickness dependence, depending on the thickness relative to the size of the inelastic zone.

2.4.3. *Components of fracture toughness during tearing*

As mentioned in Sec. 2.2.3, the fracture toughness Γ can be decomposed into an intrinsic fracture energy Γ_0 and dissipated fracture energy Γ_d. The modified trouser tear test offers a unique capability to isolate these components: Γ_0 corresponds to the fracture toughness measured in the limit where the free width b approaches zero. While Γ_d is obtained by subtracting Γ_0 from the plateau fracture toughness

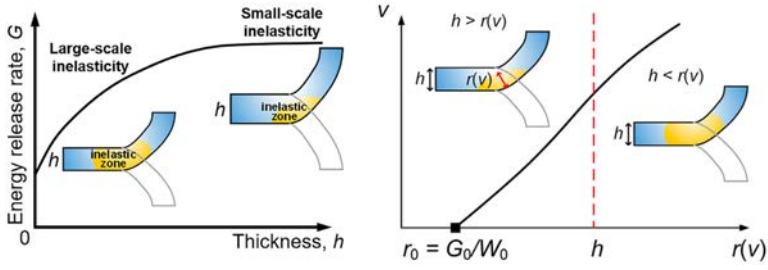

Fig. 12. Specimen thickness (h) and tear velocity (v) dependence of energy release rate (G). (a) schematic showing the transition from thickness-dependent to thickness-independent energy release rate as h increases. (b) Schematic illustration showing that the characteristic size of the inelastic zone $r(v)$ increases with v. When $h > r(v)$, dissipation is confined to a region of size $r(v)$; when $h < r(v)$, dissipation occurs throughout the entire active deformation zone, scaled by h.

Source: [Bai *et al.*, 2019a]. Copyright 2019 Elsevier.

Γ_p [Jia *et al.*, 2022]. For a classic PAAm/PAMPS DN gel, this method yields an intrinsic fracture energy Γ_0 of approximately $2000\,\mathrm{J/m^2}$ [Fig. 11b]. This value is on the same order of magnitude as the dissipated fracture energy Γ_d, which is around $1600\,\mathrm{J/m^2}$, given a plateau toughness Γ_p of around $3600\,\mathrm{J/m^2}$ [Jia *et al.*, 2022]. This finding contradicts conventional wisdom, which typically assumes that Γ_0 for DN gels corresponds roughly to the fracture toughness of the component long-chain polymer network (i.e., the second network) and is way much lower than Γ_d. This discrepancy likely stems from different definitions of the so-called "intrinsic" fracture energy. In fatigue threshold measurement, Γ_0 represents the energy to rupture a single layer of polymer chains of the long-chain polymer network [Zhang *et al.*, 2018]. In contrast, in the modified trouser tear test, Γ_0 represents the energy required to propagate a crack through the interpenetrated network structure. In this context, rupturing the long-chain polymer network inevitably involves damaging the surrounding short-chain polymer network. Consequently, the measured intrinsic fracture energy Γ_0 through the modified trouser tear test is significantly higher and exhibits deformation history dependence [Jia *et al.*, 2022].

2.4.4. *Damage zone during tearing*

The damage zone, by definition, is the region within which the material is damaged to a certain degree and mechanical properties are deteriorated [Creton and Ciccotti [2016]; Long *et al.* [2021]; Zheng *et al.* [2021]; Zhou *et al.* [2024b]. The characterization of the damage zone is important, as it can offer the damage condition of the material when used in real applications.

When a crack propagates in the DN gel during tearing, a damage zone forms around it. The degree of damage is quantified by the dissipated energy density, denoted as U_{diss} [Jia *et al.*, 2022; Matsuda *et al.*, 2020, 2021]. U_{diss} reaches its

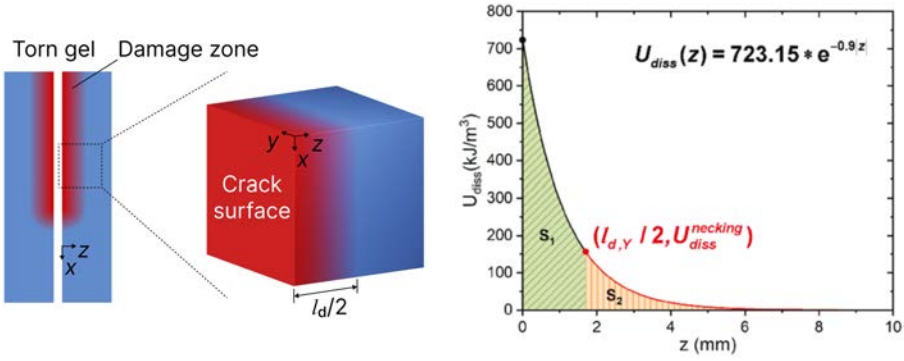

(a) (b)

Fig. 13. (Color online) Distribution of dissipated energy density in a torn DN gel. (a) Schematic of the dissipated energy density field. The red region denotes the damage zone where significant dissipation occurs. (b) Profile of the dissipated energy density (U_{diss}) as a function of distance along the z-axis ($z \geqslant 0$). U_{diss} peaks at the crack tip due to stress concentration and decays along the z-axis away from the crack plane. [Jia *et al.*, 2022].

Source: Copyright 2022 Elsevier.

maximum value at the crack tip due to stress concentration and decays along the axis perpendicular to the crack plane. The boundary where U_{diss} approaches zero defines the boundary of the damage zone, and the distance between this boundary to the crack plane determines half the damage zone, denoted as $l_d/2$ [Fig. 13(a)].

According to Fig. 11(b), Γ measured through modified trouser tear tests varies as the free width b varies. This relationship can be modeled using an exponential function as follows:

$$\Gamma(b) = -a_1 e^{-a_2 b} + a_3, \tag{2.15}$$

where a_1, a_2 and a_3 are all positive fitting parameters, which can be obtained by fitting this equation to experimental results in Fig. 11(b). The feature size of the damage zone l_d can therefore be mathematically determined as the value of b by setting the measured fracture toughness to $0.99\Gamma_p$, since $\Gamma_p = a_3$, we have

$$-a_1 e^{-a_2 l_{\text{d}}} + a_3 = 0.99 a_3. \tag{2.16}$$

The feature size of the damage zone can therefore be obtained as follows:

$$l_d = \frac{\ln a_1 - \ln 0.01 a_3}{a_2}. \tag{2.17}$$

Assuming the dissipation is uniform along the thickness direction of DN gel specimens. According to the above analysis, Γ_d can be estimated as follows:

$$\Gamma_d(b) = 2 \int_0^{\frac{b}{2}} U_{\text{diss}}(z) \mathrm{d}z, \tag{2.18}$$

where z is the direction perpendicular to the crack plane [Fig. 13(a)]. Therefore, the fracture toughness can be written as

$$\Gamma(b) = 2\int_0^{\frac{b}{2}} U_{\text{diss}}(z)\mathrm{d}z + \Gamma_0. \tag{2.19}$$

The expression for U_{diss} can be obtained by taking the derivative of Eq. (2.19), thus we have

$$U_{\text{diss}}\left(\frac{b}{2}\right) = \frac{\mathrm{d}\Gamma(b)}{\mathrm{d}b}. \tag{2.20}$$

Substituting Eq. (2.15) into Eq. (2.20) and replacing b with $2z$, the dissipated energy density along the z direction ($z \geqslant 0$) can be obtained as follows:

$$U_{\text{diss}}(z) = a_1 a_2 e^{-2a_2 z}. \tag{2.21}$$

As for typical PAMPS/PAAm DN gels, the feature size of the damage zone measured by this method is approximately 8 mm [Jia *et al.*, 2022; You *et al.*, 2025a], with the corresponding dissipated energy density profile shown in Fig. 13(b). Based on this method, You *et al.* [2025a] proposed another form of the dissipated energy density $U_{\text{diss}}(z)$ that can characterize the dynamic changes of the fracture toughness during the damage process. By pre-stretching DN gel specimens prior to tearing and further decomposing the damage zone into three mechanically distinct regions, they found that the lengths of these regions sensitively depended on the first network's cross-linking density θ. Their analysis further revealed that both the U_{diss} and the feature size of the damage zones are critical factors affecting the fracture toughness Γ.

The dissipated energy density and feature size of the damage zone can also be more directly characterized by other methods, for example, the mechanochemistry technique [Matsuda *et al.*, 2020] and microelectrode technique [Nishimura *et al.*, 2024]. We will discuss them further in Sec. 2.8.

2.5. *Adhesion test*

Although the invention of synthetic hydrogels has given rise to their applications in the field of adhesion, it was not until the recent 10 years, with the birth of DN gels, that breakthroughs have been made in this field [Li *et al.*, 2017; Yang *et al.*, 2018b; Yuk *et al.*, 2016a,b]. The adhesion performance of hydrogels can be quantitatively characterized by various adhesion tests and evaluated by various indicators. Common testing methods include peel test (ASTM F2256-24), bilayer-stretch test [Tang *et al.*, 2016], lap-shear test (ASTM F2255-24) [Rose *et al.*, 2014], and butt-joint test (ASTM F2258-24) [Figs. 14(a)–(e)]. There are two primary indicators corresponding to these adhesion test methods: interfacial toughness (also known as adhesion toughness or adhesion energy) and interfacial strength. Peel and bilayer-stretch tests usually introduce a small initial pre-crack at the adhesion interface, and these two methods can be used to measure the interfacial toughness; while the lap-shear and

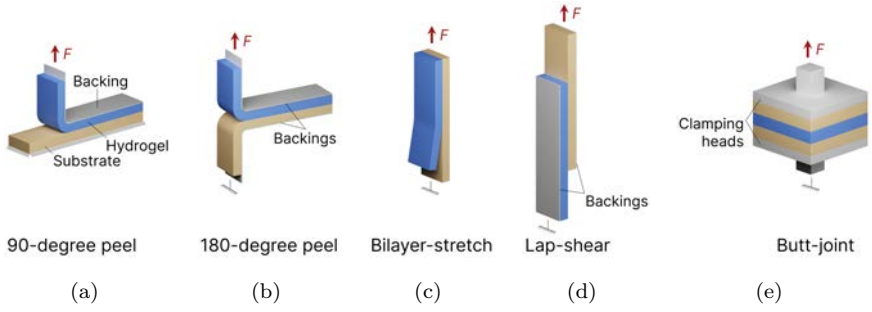

Fig. 14. Common experimental methods for characterizing the adhesion properties of DN gels: (a) 90° peel test; (b) 180° peel test; (c) bilayer-stretch test; (d) lap-shear test; (e) butt-joint test.

butt-joint tests generally do not introduce initial pre-cracks in the specimen and thus can be used to measure the interfacial strength. In practical applications, it is often necessary to select the appropriate testing method and indicator based on the specific usage scenario of DN gels.

2.5.1. *Specimen geometry and basic definitions*

Among the above adhesion tests, the peel and lap shear tests are the most commonly used adhesion tests for DN gels. We will elaborate on the specimen geometry and basic definitions of these two adhesion tests in detail below.

There are mainly two types of peel tests: the 90° peel test, which is usually used for the measurement of the adhesion property of a soft material on a hard substrate (e.g., the DN gel on the bone) [He *et al.*, 2021; Jiang *et al.*, 2024; Zhou *et al.*, 2024b], and the 180° peel test, which is more suitable for characterizing the adhesion property between two soft materials (e.g., the DN gel on the skin tissue) [Gao *et al.*, 2020; Saito *et al.*, 2011; Sakurai *et al.*, 2025; Yuan *et al.*, 2025]. The specimens used for peel tests are usually rectangular strips with a dimension of $l \times w \times t$, where l, w and t refers to the length, width and thickness of the specimen, respectively [Fig. 15(a)]. Before the peel test, the inextensible but flexible backing, usually made by polyethylene glycol terephthalate (PET), is adhered to the surface of the specimen to avoid the stretching of the specimen, and a sharp pre-crack is introduced at the interface [Fig. 15(a)], after which either the hard substrate and the peel arm or two peel arms are clamped to the test machine, and one arm of the specimen is stretched under displacement control. The force and time during the testing process are recorded to finally obtain the peeling curve in Fig. 15(b). The peel test has the same advantage of a controlled crack growth velocity as the trouser tear test, while it is worth noting that the measured interfacial toughness may be thickness-dependent [Liu *et al.*, 2019a]. Recently, some studies have noticed that the introduction of pre-cracks in the specimen may underestimate the adhesion properties of materials, as there may be no sharp pre-cracks in the material in a

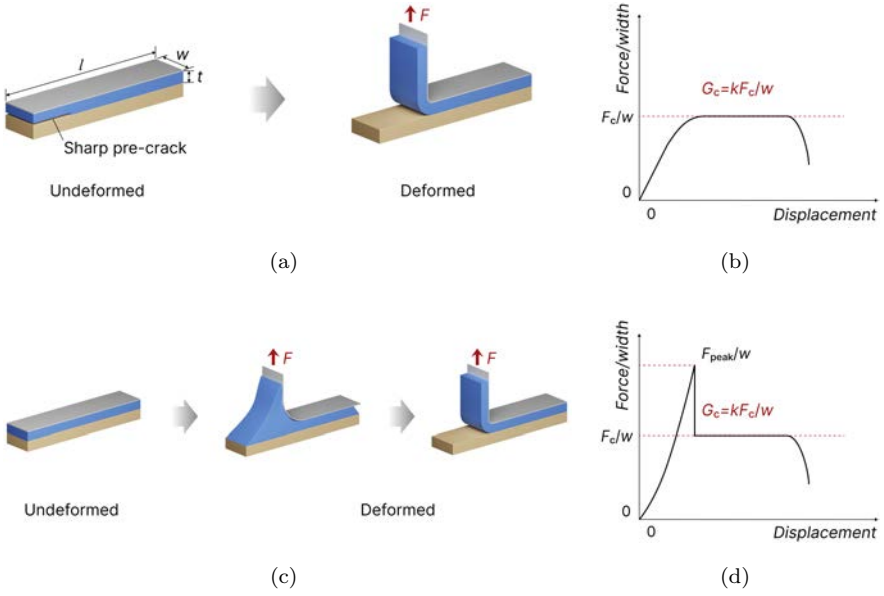

Fig. 15. Comparison of peeling behaviors of hydrogel specimens with and without pre-cracks. (a) 90° peel test of a specimen with a sharp pre-crack. The crack propagates steadily with minimal deformation at the peel front. (b) Schematic of a typical peeling curve of hydrogel specimens with a pre-crack, showing immediate steady-state crack propagation. (c) 90° peel test of a specimen without a pre-crack. Significant deformation occurs at the peel front as the crack must initiate before propagation. (d) Schematic of a typical peeling curve of hydrogel specimens without a pre-crack, characterized by a high initiation peak peel force followed by steady-state crack propagation.

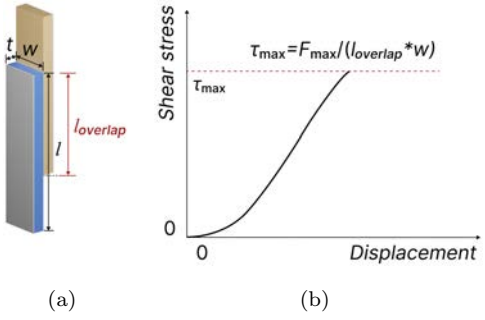

Fig. 16. Experimental setup and typical results for the lap-shear test. (a) Rectangular specimen used for testing. Unlike peel tests, pre-cracks are usually not introduced in lap-shear specimens. (b) Schematic illustration of a typical shear stress–displacement curve obtained during the test.

practical situation [Zhou *et al.*, 2024b] [Figs. 15(c) and 15(d)]. We will discuss these in detail in the subsequent sections.

For the lap-shear test, similar rectangular specimens are used. The DN gel and the hard/soft adherend overlap at the ends, and the overlap length is denoted as l_{overlap} [Fig. 16(a)]. The length of the specimen l is set at least 1.5 times the overlap

length to ensure that the failure occurs at the overlap region (ASTM F2255-24). Although one of the adherends may also be a hard or soft material, a similar setup is used. Before the lap-shear test, a stiff backing (e.g., glass film) is often adhered to the surface of the soft adherend to avoid the stretching of the specimen, and no sharp pre-crack is introduced at the interface. After which, the specimen is loaded on the tensile tester and then stretched under displacement control. The force and time during the testing process are recorded to finally obtain the shear stress–displacement curve in Fig. 16(b).

2.5.2. *Interfacial toughness*

Interfacial toughness is defined as the energy required for the interfacial crack to advance a unit area and has a unit of $\mathrm{J/m^2}$ or N/m. Interfacial toughness of DN gels is often measured by either a 90° or a 180° peel test [Kurokawa *et al.*, 2010; Li *et al.*, 2017; Yang *et al.*, 2020; Yuk *et al.*, 2016a,b]. During the test, one arm of the specimen is vertically pulled from a rigid substrate (90° peel test) or from a soft layer (180° peel test). The pre-crack propagates either at the interface between the gel and the substrate or within the bulk of the specimen. Throughout the peeling process, the peel force F initially increases until it reaches a plateau and remains constant until one arm of the specimen completely detaches [Fig. 15(b)]. Interfacial toughness is calculated as the ratio of the plateau peel force F_c to the width of the specimen:

$$G_c = k\frac{F_c}{w}, \tag{2.22}$$

where k is a prefactor, which equals 1 for 90° peel tests and 2 for 180° peel tests. This measure reflects the ability of the adhesion system to resist crack propagation when the crack grows steadily, namely, the crack propagation resistance. In this scenario, the adhesion system is safe if the external driving force is lower than the plateau peel force.

Due to the high water content and low surface friction coefficient, it has long been considered extremely difficult to adhere hydrogels to other materials, and the interfacial toughness between hydrogels and biological tissue is only around $10\,\mathrm{J/m^2}$ [Rose *et al.*, 2014]. With the emergence of DN gels, the tough adhesion of hydrogels to solid substrates can be achieved by anchoring the DN gels to the porous solid via DN structure formation, achieving an interfacial toughness of several hundred to one thousand [Kurokawa *et al.*, 2010; Saito *et al.*, 2011; Sakurai *et al.*, 2025]. However, this method can only be applied to the adhesion of DN gels to porous solids. Until 2016, Yuk *et al.* [2016a] proposed a breakthrough strategy to achieve tough adhesion between hydrogel and non-porous materials, which has two requirements: a tough hydrogel and a strong interface [Yang *et al.*, 2020]. Based on these requirements, a commonly adopted strategy for achieving tough adhesion is the combination of tough DN gels and the chemical/physical anchorage of polymer chains to the substrate surface, which results in an interfacial toughness on the

order of $1000\,\mathrm{J/m^2}$ [Freedman *et al.*, 2024; Li *et al.*, 2017; Ma *et al.*, 2022; Sakurai *et al.*, 2025; Yang *et al.*, 2018b; Yuk *et al.*, 2016a,b]. By using a particle gel-based DN gel technique with surface initiation of substrates, the tough adhesion of DN gels to non-porous solids with various complex shapes can also be achieved [Saito *et al.*, 2011; Takahashi *et al.*, 2018].

Different from what has been mentioned above, in practical use, sharp interfacial pre-cracks may not exist, and a crack needs to initiate first before reaching a steady propagation state [Fig. 15(c)]. In this case, the peel force will first increase to a peak and then abruptly drop to a low value, accompanied by the initiation of a sharp crack. Subsequently, the crack propagates steadily, and the peel force reaches a plateau. The plateau peel force at this time is the same as that of the adhesion system with an initial sharp pre-crack, as mentioned above, but much lower than the peak peel force [Fig. 15(d)]. Although the plateau peel force can still reflect the interfacial toughness of the adhesion system, the maximum allowable loading force for an intact adhesion system should not be determined by it, but by the peak peel force; otherwise, the bearing capacity of the system would be far underestimated. Considering this, Zhou *et al.* [2024b] proposed a new measure of adhesion property named crack initiation resistance, which characterizes the crack initiation resistance of hydrogels and may have a more realistic meaning. It is worth mentioning that some researchers have also noticed this problem relating to hydrogel adhesion [He *et al.*, 2021]. However, the crack initiation resistance of DN gels has not been widely explored yet.

2.5.3. *Interfacial strength*

Interfacial strength is defined as the maximum nominal stress at which the adhesion system is ruptured under monotonic loading and has a unit of $\mathrm{N/m^2}$. Interfacial strength of DN gels is often measured by the lap-shear test (ASTM F2255-24) [Song *et al.*, 2024; Zhang *et al.*, 2023b]. During the lap-shear test, one arm of the specimen is monotonically loaded until fracture, and the measured force F monotonically increases with the displacement. A representative force–displacement curve of a lap-shear test is shown in [Fig. 16]. The maximum force $F_{\max}$, together with the initial overlap area $l_{\mathrm{overlap}}w$, determines the interfacial strength $\tau_{\max}$:

$$\tau_{\max} = \frac{F_{\max}}{l_{\mathrm{overlap}}w}. \tag{2.23}$$

The DN gels can provide interfacial strength of dozens to hundreds of kilopascals [Song *et al.*, 2024; Yuk *et al.*, 2019], while for SN gels, this value is usually hundreds of pascals [Zhang *et al.*, 2023b].

It is worth noting that although the interfacial toughness and interfacial strength are indicators of adhesion performance, they sometimes conflict. High interfacial toughness does not necessarily mean high interfacial strength, and vice versa. For example, it is generally believed that hydrogel adhesion based on commercial

502 glue (primarily composed of cyanoacrylate) exhibits low interfacial toughness but high interfacial strength, while chitosan-based hydrogel adhesion exhibits high interfacial toughness but low interfacial strength [Yang *et al.*, 2018b, 2020]. The contradictory relationship between the two indicators of interfacial toughness and interfacial strength still needs further study.

Recent studies have shown that there exists a characteristic length of hydrogel adhesion [Zhang *et al.*, 2023b]. When the hydrogel thickness is less than this characteristic value, the interfacial strength behaves as a material constant, while the interfacial toughness increases with increasing thickness. Conversely, when the hydrogel thickness exceeds the characteristic value, the interfacial toughness becomes a material constant, while the interfacial strength decreases with increasing thickness and exhibits a large scattering. This characteristic length is believed to be related to the flaw-sensitivity length of the hydrogel [Chen *et al.*, 2017; Liu *et al.*, 2019a; Zhang *et al.*, 2023b]. For DN gels, their flaw-sensitivity length is measured to be around 0.05 mm [Zhou *et al.*, 2021]. When evaluating the adhesion performance of DN gels, the influence of the hydrogel thickness may also need to be considered.

2.5.4. *Fatigue behavior*

The above test methods can characterize the adhesion properties of DN gels under monotonic loads. However, in practical applications, adhesion systems often need to withstand long-term dynamic loads, which may also cause fatigue at the bonding interface. Similar as mentioned in Sec. 2.2.5 about the fatigue behavior using pure shear tests, fatigue of the adhesion system also includes fatigue damage and fatigue fracture, and they can be measured using adhesion tests.

By improving the adhesion testing method under monotonic loading, the adhesion fatigue performance of DN gels under cyclic loading can also be measured. For example, by applying cyclic loads of varying amplitudes to a pre-cracked adhesion system under the 90° peel test and recording the crack growth during each load cycle, the crack growth rate as a function of energy release rate can be plotted [Figs. 17(a), 17(b)]. When the energy release rate approaches the interfacial toughness under monotonic loading, the crack growth rate approaches infinity. Reducing the energy release rate until the crack growth rate approaches 0 is the fatigue threshold of the adhesion system under cyclic loading [Fig. 17(b)]. Below the fatigue threshold, the crack will not grow under cyclic loading.

By applying cyclic loads with varying amplitudes to an adhesion system without pre-cracks under the butt-joint test and recording the displacement during each load cycle [Fig. 17(c)], the evolution of the maximum displacement as a function of the number of cycles can be obtained [Fig. 17(d)]; by recording the number of cycles until the adhesion system ruptures, a stress amplitude-cycle number curve, also known as an S–N curve, can also be obtained [Fig. 17(e)]. Through this curve, the interfacial strength of the adhesion system under monotonic load and the endurance limit under cyclic load can be obtained. When the cyclic load is lower than the endurance

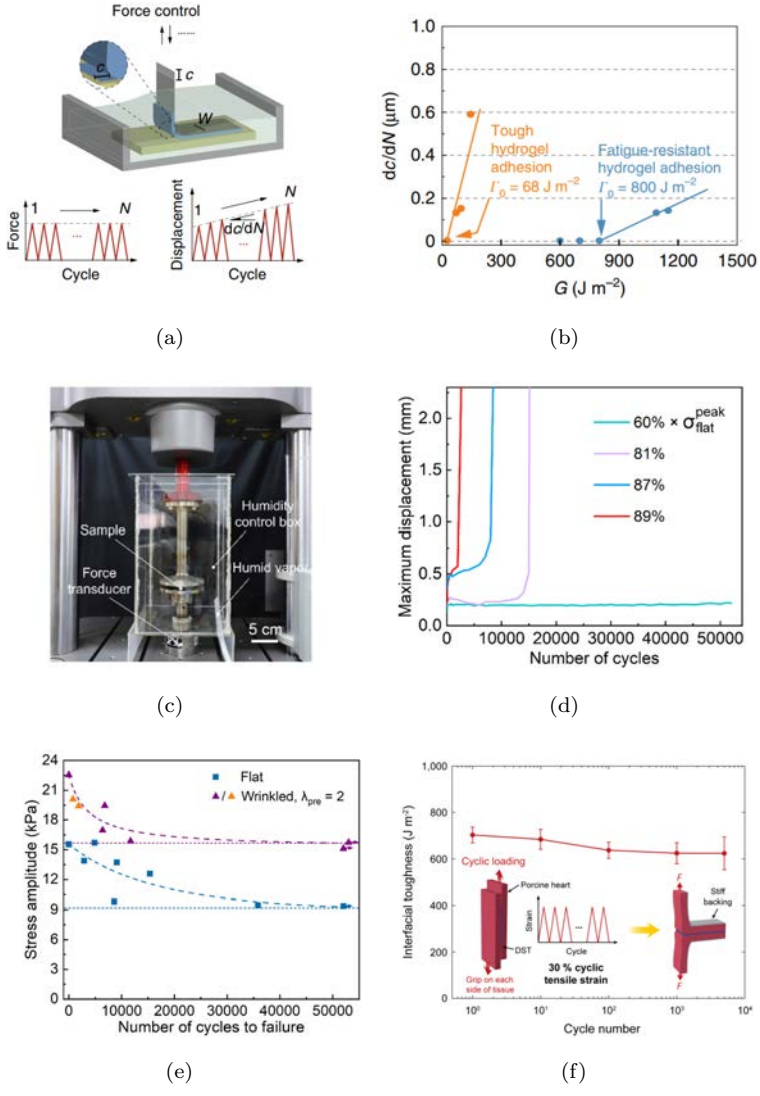

Fig. 17. Experimental methods for characterizing fatigue of hydrogel adhesion. (a) Schematic illustration of the fatigue crack propagation test, measuring interfacial crack extension c versus cycle number N under a cyclic peeling force F_a. (b) Crack extension rate (dc/dN) plotted against the applied energy release rate G ($G{=}F_a/w$) for tough and fatigue-resistant hydrogel adhesion on glass. (c) Experimental setup for the fatigue damage test using force control. (d) Maximum displacement during each load cycle plotted against N. (e) S–N curves for different adhesion systems. Horizontal dashed lines indicate endurance limits, while curved dashed lines serve as guides for the eye. Arrows indicate that no failure occurred. (f) Experimental setup for another type of fatigue damage test via cyclic pre-loading followed by a 180° peel test, with the corresponding interfacial toughness versus cycle number presented.

Source: [Liu *et al.*, 2020]. Copyright 2020 under the terms of the Creative Commons CC BY license. [Li *et al.*, 2021]. Copyright 2021 under the terms of the Creative Commons CC BY license. [Yuk *et al.*, 2019]. Copyright 2019 under the terms of the Creative Commons CC BY license.

limit, the adhesion system does not suffer fatigue fracture under long-term cyclic load. When the cyclic load is close to or even higher than the interfacial strength, the adhesion system is prone to fracture under monotonic load. By applying different degrees of cyclic load to the adhesion system without pre-cracks and then measuring the interfacial strength or interfacial toughness of the adhesion system, the change of adhesion performance with loading history can be obtained [Yuk *et al.*, 2019] [Fig. 17(f)], which is also a way to reflect the fatigue damage behavior of the adhesion system.

Under cyclic loading, tough adhesion strategies that are suitable for monotonic loading may not necessarily be effective. For example, the tough adhesion strategy based on the combination of tough DN gels and strong interfacial interactions may experience a sharp decline in interfacial toughness under cyclic loading. This is primarily due to the irreversible rupture of sacrificial bonds within the DN gels after repeated loading, resulting in a decrease in the fracture toughness of the hydrogel itself and no longer meeting one of the requirements of the tough adhesion strategy. Therefore, there is a need to explore new strategies for the anti-fatigue tough adhesion strategy.

Considering that the limitation of traditional tough adhesion strategy mainly stems from the destruction of irreversible covalent bonds in tough hydrogels, the most direct way to achieve fatigue-resistant hydrogel adhesion is to introduce a network constructed by dynamic covalent bonds or non-covalent bonds into the hydrogel. For example, Rao *et al.* [2018] prepared a DN gel with the sacrificial network constructed by dynamic hydrogen bonds. Due to the presence of these reversible bonds, the DN gel has a self-repairing function and maintains strong adhesion performance under cyclic load. Another approach to achieve the anti-fatigue adhesion of hydrogels is structural design [Zhou *et al.*, 2024b], which does not necessarily require the use of DN gels and will not be elaborated in detail in this article. However, the use of dynamically cross-linked sacrificial networks to construct DN gel adhesive patches is still a common strategy used in current biomedical articles and applications.

2.6. *Tribological test*

The discovery of DN gels has greatly expanded the potential of hydrogels to a wide range of applications where better tribological properties, such as low friction and high wear resistance, are required. The friction and wear properties of DN gels against a piece of solid substrate, such as glass, can be measured in air or in water using the tribometer, rheometer, or AFM [Gombert *et al.*, 2019; Gong *et al.*, 1999a; Gong and Osada, 2002; Meinert *et al.*, 2025], which will be elaborated one by one in details in subsequently sections.

One way to measure the friction properties of DN gels against a solid substrate is to use the tribometer [Chang *et al.*, 2007; Gong and Osada, 2002; Simic *et al.*, 2020; Takahashi *et al.*, 2018]. There are two common types of tribometers, one is

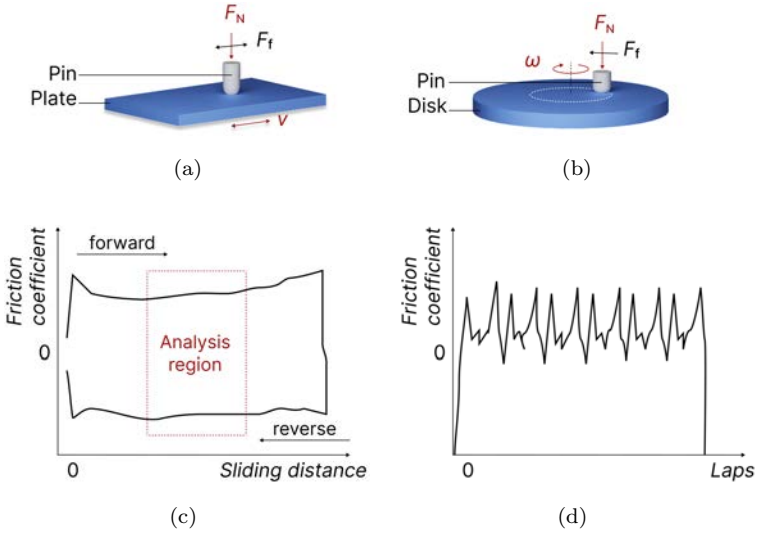

Fig. 18. Experimental setups of tribometers and typical results for tribological tests. (a) Schematic of the pin-on-plate test, where the plate is mounted on a stage reciprocating at a specified speed v. (b) Schematic of the pin-on-disk test, where the disk rotates with a specified angular velocity ω. (c) Typical friction loops measured from the pin-on-plate test, the friction coefficient is obtained by averaging the middle analysis region. (d) Typical profile of the friction coefficient versus rotation laps from the unidirectional pin-on-disk test, the final coefficient is determined by averaging the steady-state region.

the linear reciprocating tribometer [Bonyadi *et al.*, 2021; Simic *et al.*, 2020; Takahashi *et al.*, 2018] [Figs. 18(a) and 18(b)], the other is the pin-on-disk tribometer [Li *et al.*, 2024c; Zhang *et al.*, 2019a] [Figs. 18(c)–18(e)]. Usually, a motor-driven stage will oscillate the plate or rotate the disk beneath a fixed ball. The former one, by definition, conducts a linear reciprocating motion, while the latter one conducts a rotational motion. For both types of tribometers, the hydrogel can either be the pin or the plate/disk, or both the pin and plate/disk, which corresponds to two different contact types, i.e., migrating contact and static contact. As for the static contact, the same area of the hydrogel surface is continuously in contact with the countersurface and the contact zone is stationary on the hydrogel specimen during the friction test; while for the migrating contact, the countersurface constantly moves onto a new, undisturbed area of the hydrogel surface and the contact zone is continuously migrating across the hydrogel specimen. For example, a solid pin sliding on a hydrogel plate results in a migrating contact, while a hydrogel pin sliding on a solid surface results in a static contact. Thus, the specimen used on a tribometer can be a pin or a flat plate/disk, depending on which tribometer and contact type are adopted [Figs. 18(a) and 18(b)].

The frictional force as a function of time can be recorded during the friction test. The friction performance of the hydrogel is usually characterized by the friction coefficient or coefficient of friction (i.e., COF) μ, and calculated as the ratio of the

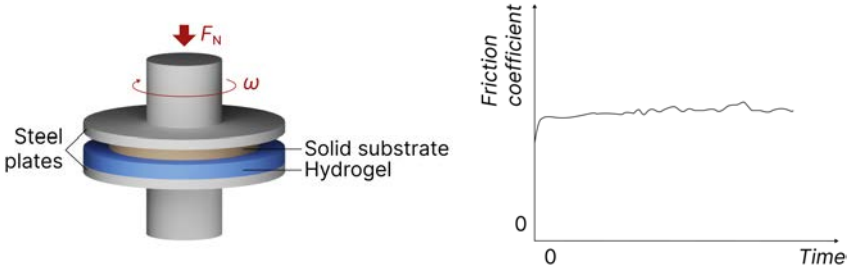

(a) (b)

Fig. 19. Rheometer-based experimental setup and typical tribological result. (a) Schematic illustration of the rheometer setup. (b) Typical profile of the friction coefficient versus time measured using the rheometer.

constant frictional force F_f and the applied load F_N:

$$\mu = \frac{F_f}{F_N}. \tag{2.24}$$

Typical profiles of friction coefficient as a function of the sliding distance obtained from the pin-on-plate test or friction coefficient as a function of the rotation laps obtained from the pin-on-disk test are shown in Figs. 18(c) and 18(d), respectively.

The friction properties of DN gels against a solid substrate can also be measured using a rheometer [Chang *et al.*, 2007; Ren *et al.*, 2024; Simic *et al.*, 2020] [Fig. 19(a)]. The specimen used on the rheometer is usually a round/square sheet. Prior to the measurement, the gel specimen is glued to the lower surface of coaxial disk-shaped platens, and another solid substrate is either the upper platen or glued to the upper platen, with a diameter of R, R is much smaller than the radius/side length of the specimen. An axial force F_N is then applied to the specimen, and the upper platen rotates with a constant angular velocity ω. The time and torque T during the test are recorded. Since the rotation velocity v changes with the distance from the center of the axis, i.e., $v = \omega R$, the obtained torque T is a total value over the velocity range from 0 to ωR. Supposing that the friction is linearly proportional to the velocity, the frictional force is calculated as [Gong *et al.*, 1999b]

$$F_f = \frac{4T}{3R}. \tag{2.25}$$

The COF can subsequently be obtained by substituting the above equation into Eq. (2.24) [Fig. 19(b)]. The COF obtained from the rheometer generally agrees with results obtained from the tribometer [Kagata *et al.*, 2002]. In both cases, prior to the measurement, the gel specimen is usually loaded with a normal strain (or normal load) for a certain time period (usually 10–60 min) Gong and Osada [2002]; Parada *et al.* [2017], until the normal load (or normal strain) reaches an equilibrium state. After achieving relaxation equilibrium, a displacement with a constant velocity ω

(or v) is applied to the upper platen (or lower platen) to generate the torque (or frictional force).

Using a rheometer to measure the friction properties is considered to have several advantages over the tribometer. One is the possibility of measuring the friction of the DN gel–solid interface with small gel specimens. The other is its high sensitivity in detecting the frictional force that is encountered in measuring the extremely low friction of gels. Varying normal forces and shear rates can be used to study the effect of these two parameters on the friction properties of DN gels. At a constant shear rate, the COF of DN gels generally exhibits a slight reduction as the normal force increases, while at a constant normal force, the COF increases as the shear rate increases [Kaneko *et al.*, 2005; Ren *et al.*, 2024]. However, this speed-dependency of hydrogels is considered characteristic of dense, crosslinked surfaces, whereas brushy surfaces maintain low, speed-independent friction unless continuous contact and shear cause water exudation and subsequent densification of this surface layer [Simic *et al.*, 2020]. The dependency of COF on the normal force and shear rate is considered to be influenced by the dynamics of polymer chain ends and loops tethering the hydrogel surface [Chang *et al.*, 2007; Ren *et al.*, 2024], while their underlying mechanisms have not been fully explored yet. These phenomena also demonstrate that, unlike general solids, the DN gel friction does not simply obey Amonton's law [Gao *et al.*, 2004] (i.e., $F_f = \mu F_N$), in which μ is a material constant [Gong *et al.*, 1999a].

The COF of conventional covalent-crosslinked DN gels (e.g., PAMPS/PAAm DN gel) in existing researches are usually on the order of around 10^{-1} to 10^{-2} under a pressure on the order of kilopascal [Bonyadi *et al.*, 2021; Kaneko *et al.*, 2005; Ren *et al.*, 2024; Takahashi *et al.*, 2018], some other DN gels consisting of both ionic and covalent networks can achieve a super-lubrication with the COF on the order of 10^{-3} at relatively low velocity of around $10^{-4}\,\mathrm{ms}^{-1}$ and a pressure of 7 Pa [Li *et al.*, 2015]. Existing studies have shown that the presence of polyelectrolyte brushes on a hydrogel surface can effectively reduce their COF against a glass plate to a value as low as 10^{-4} [Gong *et al.*, 2001]. Based on this conclusion and combines the DN gel, Kaneko *et al.* [2005] added a third component, either a weakly crosslinked PAMPS network or non-crosslinked linear PAMPS polymer chains, to the DN gel, the new materials show compressive strength as high as the DN gel while COF as low as 10^{-5} even with a high pressure around 105 Pa. Bonyadi *et al.* [2021] further investigated the tribological performance of charged DN gels by introducing 10 wt% comonomers of varying charges (i.e., neutral, positive, negative, and zwitterionic), and found that DN gels with a neutral or zwitterionic second network had the lowest friction that even below that of cartilage. Their work also demonstrated that the tribological properties of DN gels can fulfill the lubrication demands of the joint as successful cartilage replacement candidates. By exploiting environmental oxygen "contamination", Zhang *et al.* [2019a] synthesized P(AAm-AMPS)/alginate DN gels with a gradient in crosslinking density at the near-surface region, which can result in a top-surface delamination of DN gels when swelled in water, due to

the mismatch in the swelling ratio between the skin layer and the bulk DN gel. The subsequently exposed subsurface exhibited a COF of 0.02 in gel-on-glass, which validates it as another effective method for designing DN gels with high lubrication. By applying a voltage within the range of 0–5 V, Wada *et al.* [2018] found that the friction of DN gels can be controlled. With the increase of the voltage from 0 V to 5 V, the COF increases from the order of around 0.01–0.1. By using this property of DN gels, they even developed a soft inchworm robot with friction control of feet [Selvamuthu *et al.*, 2023; Takagi *et al.*, 2019].

In addition to the above two mainstream testing methods, AFM has emerged as an indispensable tool in recent years, offering molecular-level insights into hydrogel friction that are inaccessible through macroscopic measurements. The most reliable method employs AFM in lateral force microscopy (LFM) mode [Lee and Espinosa-Marzal, 2023; Ruan and Bhushan, 1994; Shoaib and Espinosa-Marzal, 2018, 2019; Shoaib *et al.*, 2022] [Fig. 20(a)]. The use of a micrometer-sized spherical tip (e.g., silicon or colloid), rather than a sharp tip, is critical. This approach ensures a well-defined contact geometry, generating low contact pressures (typically in the range of tens of pascals) that prevent sample damage, such as plowing or pile-up. The COF measured at this micro-scale is usually much lower than values obtained from macroscopic tribometers or rheometers [Ruan and Bhushan, 1994]. This discrepancy arises probably because macroscopic friction includes substantial energy dissipation from mechanisms largely absent in AFM measurements, such as the ploughing of surfaces by asperities, the abrasive effects of wear debris, and large-scale viscoelastic deformation [Ruan and Bhushan, 1994]. During a measurement, the sample is scanned perpendicular to the cantilever's long axis, and the frictional force is determined directly from the torsional (lateral) response of the cantilever. By analyzing the difference between the trace and retrace signals, known as the friction loop, the signals related to friction can be accurately quantified while decoupling them from topographical artifacts [Ruan and Bhushan, 1994]. Furthermore, this technique allows for the investigation of more sophisticated phenomena such as static friction F_s and contact aging (the increase in static friction with the increase of loading time) [Shoaib and Espinosa-Marzal, 2019]. This is achieved through a "stop-hold-go" protocol, where the probe remains stationary on the surface for a controlled hold time before sliding is initiated. The static friction is then defined as the maximum lateral force observed at the onset of motion, after which the friction force will drop to a dynamic one F_d [Fig. 20(b)]. By systematically varying parameters such as normal load, sliding velocity, hold time, and temperature, AFM enables researchers to build a direct structure-property relationship, linking the unique network architecture and interfacial dynamics of hydrogels to their micro-scale frictional response. By using this LFM mode of AFM, Lee and Espinosa-Marzal [2023] investigated the stimuli-responsive friction properties of Agarose/poly(acrylamide-co-acrylic acid) DN gels. Through the AFM technique, the 2D friction images of DN gels can be obtained [Fig. 20(c)], and the friction loop can be obtained by extracting data from a specified line on the friction image [Fig. 20(d)]. Due to the high resolution of the

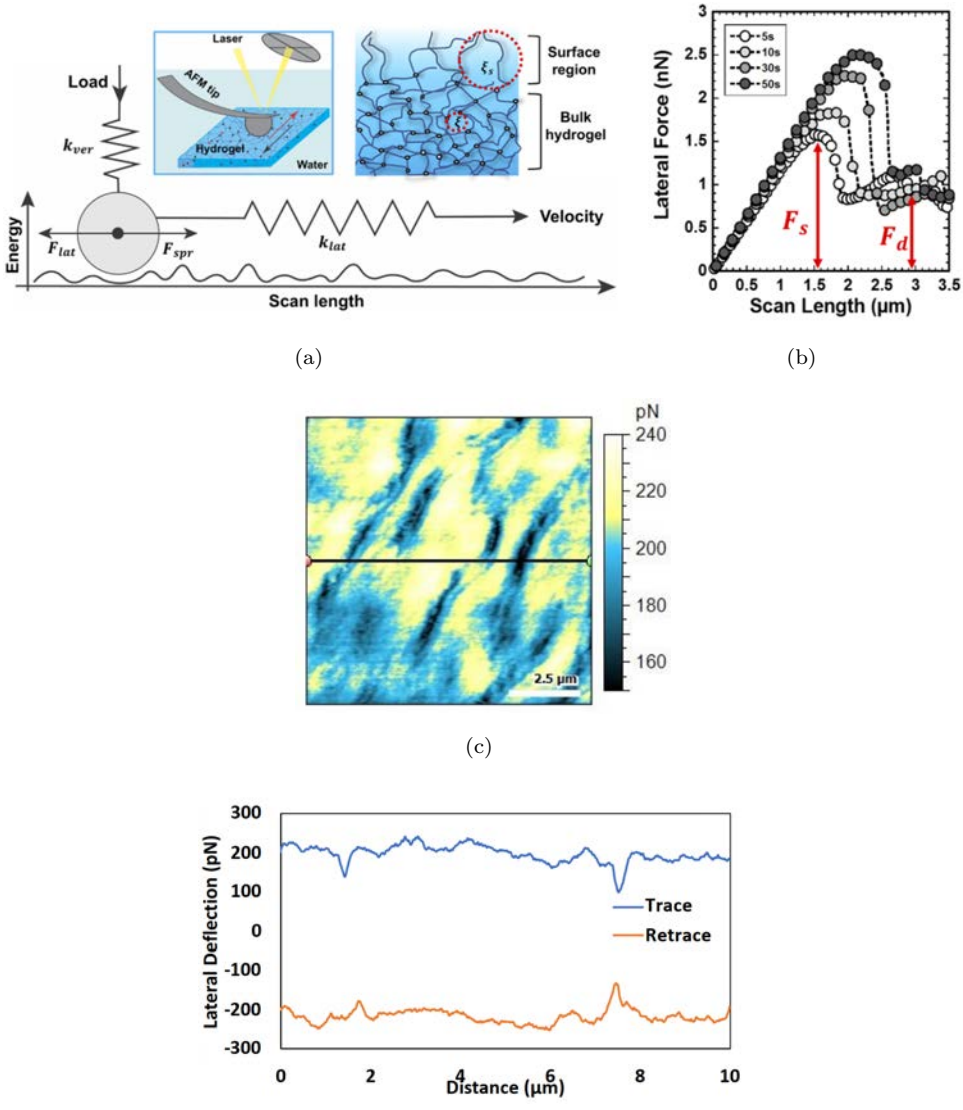

Fig. 20. Experimental setup and typical results for AFM-based friction measurements. (a) Schematic of the AFM setup using a micrometer-sized spherical tip on a hydrogel surface. Lateral force (F_{lat}) is determined from the cantilever torsion, measured via laser deflection and the lateral spring constant (k_{lat}). (b) Lateral force measured at a sliding velocity of 2 μm/s after various dwell times (5, 10, 30 and 60 s). The plot highlights static friction (F_s) and dynamic friction (F_d). (c) 2D friction image recorded at a normal load of 10 nN and a sliding velocity of 10 μm/s. (d) Friction loop extracted along the line shown in (c), illustrating the heterogeneous frictional response of the DN gel.

Source: [Shoaib and Espinosa-Marzal, 2019]. Copyright 2019 American Chemical Society. [Lee and Espinosa-Marzal, 2023]. Copyright 2023 under the terms of the Creative Commons CC BY license.

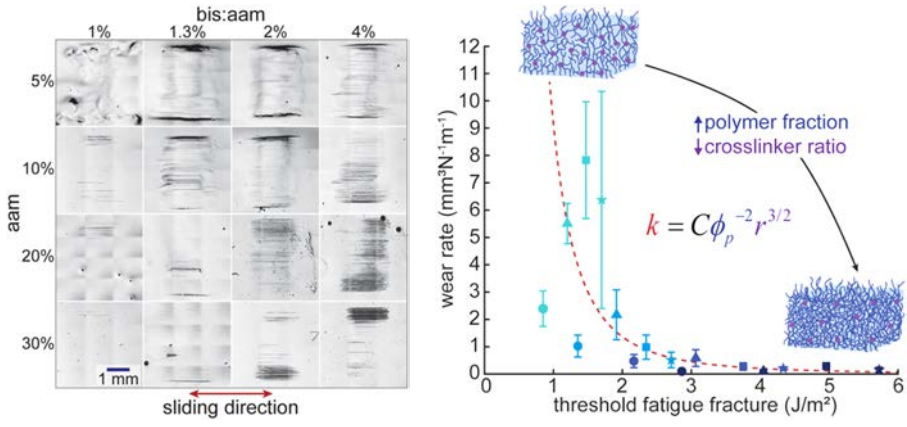

(a) (b)

Fig. 21. Wear analysis of hydrogels. (a) Optical images of wear scars for hydrogels with varying compositions. (b) Correlation between the wear rate and the theoretical fatigue fracture threshold for hydrogels with varying compositions. [Bonyadi and Dunn, 2020b].

Source: Copyright 2020 American Chemical Society.

AFM technique, the contribution of each network to friction can be easily characterized, and they found that the copolymer-rich phase is the main source of the stimulus-responsive friction, and friction mainly arises from the viscous shear of the polymeric networks, whereas hydrodynamic lift and viscoelastic deformation become more significant at higher sliding velocities.

The wear test of DN gels can be performed using the above-mentioned friction tests with a cyclic loading control [Takahashi *et al.*, 2018]. The wear scar [Kim *et al.*, 2021; Takahashi *et al.*, 2018], wear depth H [Chanda *et al.*, 1997; Yasuda *et al.*, 2005], or wear volume V [Bonyadi *et al.*, 2019; Bonyadi and Dunn, 2020a]] obtained from laser scanning confocal microscopy are direct measurements of wear properties. Besides, Archard's wear law is commonly used for comparing the wear resistance of different materials under different loading conditions [Bonyadi and Dunn, 2020b] [Fig. 21(d)]:

$$k = \frac{V}{F_N d}, \tag{2.26}$$

where k is the wear rate, F_N is the normal load, and d is the total sliding distance. The wear rate may be influenced by the normal load or the sliding velocity during the wear test [Bonyadi and Dunn, 2020a].

By conducting one million-cycle pin-on-plate tests on DN gels with different compositions, Yasuda *et al.* [2005] found that the PAMPS/PDMAAm DN gel possesses remarkable wear-resistant properties, with a maximum wear depth (3.20 μm) that was minimal and statistically comparable to that of ultra-high molecular weight polyethylene (UHMWPE) (3.33 μm), the clinical standard for artificial joints. This

superior performance has been reinforced in studies of particle-based DN (P-DN) gel coatings, which also utilize the DN sacrificial bond concept [Takahashi *et al.*, 2018]. In pin-on-plate tests, P-DN coatings demonstrated strong wear resistance with no observable wear tracks after 300 cycles, in stark contrast to SN PAAm gel coatings that show obvious wear tracks. Other compositions, such as PAMPS/PAAm and Cellulose/PDMAAm, also proved significantly more resistant to wear than conventional hydrogels, although not all DN designs (e.g., Cellulose/Gelatin) were successful [Yasuda *et al.*, 2005], highlighting the critical role of network composition.

The mechanism of wear is fundamentally rooted in fracture mechanics, as wear is defined as the removal of material from a surface [Bonyadi *et al.*, 2019]. Because wear is a cyclic process, it can be characterized as a fatigue fracture phenomenon. This connection has been explicitly quantified in recent studies on SN hydrogels, which provide a framework for linking fundamental network properties to abrasive wear by measuring the theoretical fatigue fracture threshold and wear rate of hydrogels with different compositions [Bonyadi and Dunn, 2020b] [Fig. 21]. Consequently, the researchers found the wear rate k follows a power law relationship with the theoretical fatigue fracture threshold Γ_0 as

$$k = \mathrm{c}\Gamma_0^b, \tag{2.27}$$

where b and c are fitting constants. Because theoretically the fatigue fracture of hydrogels depends on the polymer fraction and molar ratio of the polymer to crosslinker, that is

$$\Gamma_0 = \phi_p^{\frac{2}{3}} bUl\sqrt{n}, \tag{2.28}$$

where b is the number of C–C bonds per volume of dry polymer, U is the energy of a single C–C bond, l is the length of the monomer, n is the number of monomers between two crosslinks, and ϕ_p is the volume fraction of the polymer in the hydrogel. Substituting Eq. (2.28) into Eq. (2.27), a direct relationship between the hydrogel composition and wear rate is developed:

$$k = \mathrm{C}\phi_p^{-2} r^{\frac{3}{2}}, \tag{2.29}$$

where C is a constant that contains structural information of hydrogels [Bonyadi and Dunn, 2020b]. According to this scaling law, a higher polymer content ϕ_p and lower cross-linker ratio r can reduce wear. Although this work is based on the study of SN hydrogels, this relationship may also be applied to DN gels, and its universality still needs to be verified.

2.7. *Rheological test*

Rheology studies the deformation and flow properties of materials. It not only focuses on the static mechanical properties of materials, but also on their dynamic response. A comprehensive rheological analysis of DN gel systems is essential, as it

(a)

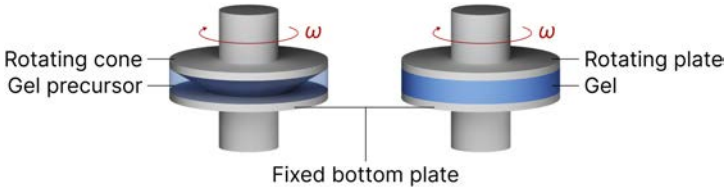

(b)

Fig. 22. Rheological test apparatus used to characterize hydrogels. (a) Overall view of the DMA and the tension clamp configuration. The instrument supports multiple modes (tension, compression, flexure, shear) [Liu *et al.*, 2019b]. (b) Rheometer configurations. The cone-and-plate geometry (left) is typically used for liquid precursors, while the parallel-plate geometry (right) is used for cured solid gels.

Source: Copyright 2018, Springer Science Business Media B.V.

provides the critical link between chemical structure and the functional properties required for both processing and final application.

Rheological test is usually conducted on a dynamic mechanical analyzer (DMA) [Fig. 22(a)] or a rheometer [Fig. 22(b)]. The former is more suitable for analyzing the tension, compression, and bending behaviors of already formed, solid-state hydrogels, while the latter is primarily used to characterize the precursor of hydrogels, measuring properties such as sol–gel transition, thixotropy that are critical for developing applications related to 3D printing and injectability, and it can also be used to characterize cured hydrogels such as measure the tribological properties of hydrogels, as we have discussed in Sec. 2.6.

In rheological research, the rheological properties of materials are described by a series of rheological parameters, such as viscosity η, complex modulus G^*, phase angle δ, etc, which can be obtained directly from the DMA or rheometer.

The rheological testing protocols of DN gels can be broadly divided into two main categories: (1) characterization of the precursor or soft gel state to determine processing viability (such as for 3D printing and injectability), and (2) characterization of the final cured or solid state to determine its end-use mechanical performance. For DN hydrogels designed to be injectable or used as bio-inks for 3D printing, the rheological properties of the precursor solution are paramount. In this case, the

steady shear test and step-recovery test are two commonly used tests. While after the DN gel is processed and fully cured, a different set of rheological tests, such as strain sweep test and frequency sweep, is required to characterize its final network structure and mechanical performance.

Next, we will first introduce the concepts of these rheological parameters and then elucidate rheological testing protocols for DN gels.

2.7.1. *Definition of common rheological parameters*

The viscosity η measures the internal resistance of the DN gel precursor in shear flow. In the simplest model, a force (shear stress τ) is applied to the upper surface of the fluid layer, while the lower surface remains fixed. If the fluid undergoes deformation, the viscosity is the proportional coefficient between the applied shear stress τ and the shear rate $\dot{\gamma}$:

$$\eta = \frac{\tau}{\dot{\gamma}}. \tag{2.30}$$

For a viscoelastic precursor, the measured η is not constant, it is a function jointly determined by the shear rate $\dot{\gamma}$, temperature T, and network structure. At very low shear rate (within the linear viscoelastic region (LVR)), the precursor usually presents a "zero shear viscosity" η_0, i.e., the platform value, which reflects the synergistic contribution of the hydraulic resistance of the polymer chains and the instantaneous entanglement between the two networks. As the shear rate $\dot{\gamma}$ increases, shear thinning (η decreases) may be observed, which is due to the gradual orientation or partial disentanglement of the network in the flow.

During rheological experimental tests, the complex modulus G^* is a frequency-dependent vector that simultaneously quantifies the elastic stiffness and viscous damping of the DN gel, as expressed by

$$G^*(\omega) = G'(\omega) + iG''(\omega), \tag{2.31}$$

where $G'(\omega)$ is the storage modulus, which is the in-phase elastic component and reflects the energy stored and recovered per cycle, while $G''(\omega)$ is the loss modulus, which is the 90°-out-of-phase viscous component and reflects the energy dissipated per cycle. The magnitude $|G^*| = \sqrt{G'^2 + G''^2}$ is regarded as an apparent stiffness, while the ratio $\tan\delta = G''/G'$ is the loss factor:$\tan\delta \ll 1$ indicates a solid-like DN gel, and $\tan\delta \approx 1$ indicates a visco-liquid. G^* serves as the crucial constitutive parameter for the viscoelastic behavior of the DN gels, providing an experimental bridge for quantitatively coupling the evolution of microscopic networks with macroscopic mechanical responses. Specifically, the storage modulus G' directly reflects the instantaneous stiffness of the polymer network, while the loss modulus G'' characterizes the energy dissipation ability. By adjusting the formulation of DN gels, both G^* and $\tan\delta$ can be controlled accordingly [Wang *et al.*, 2023a,b].

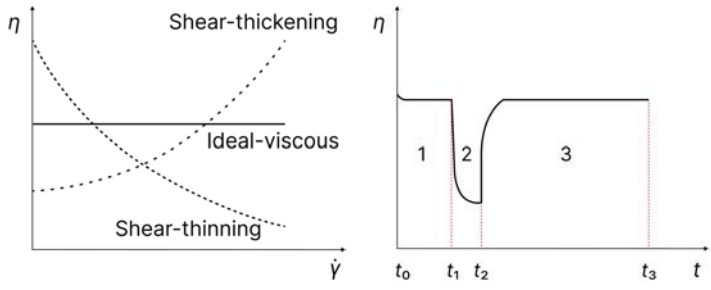

Fig. 23. Rheological flow behavior of hydrogel precursors. (a) Schematic graph showing the viscosity (η) as a function of shear rate ($\dot{\gamma}$). Hydrogel precursors may exhibit Newtonian, shearing-thinning, or shear-thickening behaviors. (b) Time-dependent viscosity profile of a thixotropic hydrogel. From t_0 to t_1 (low shear), the material exhibits a stable rest viscosity. Structural decomposition occurs from t_1 to t_2 (high shear application), followed by structural regeneration from t_2 to t_3 (shear removal).

2.7.2. *Steady shear*

Steady shear test measures the material's viscosity η as a function of the applied shear rate $\dot{\gamma}$ with controlled shear rate or controlled shear stress [Tirumala *et al.*, 2008; Tominaga *et al.*, 2007; Zheng *et al.*, 2023a], the resulting curve of which is usually called flow curve [Fig. 23(a)]. This is the primary test to determine the tendency of a material to flow, or to put it more practically, extrudability. According to the flow curve, solutions may exhibit ideal-viscous, shear-thinning, or shear-thickening behaviors. An ideal hydrogel precursor solution that can be used as printing inks exhibits shear-thinning behavior, where viscosity decreases significantly at high shear rates (i.e., inside the printing nozzle or injection needle). This property ensures the material can be extruded smoothly with minimal force, which is particularly important for 3D printing manufacture of DN gels. By conducting steady shear tests on PAMPS/PAAm solution mixtures with different PAMPS volume fractions, Tominaga *et al.* [2007] found that the maximum in the solution viscosity and fracture toughness occur in a similar volume fraction range, which indicates that there may be an association between the two components of DN gels.

2.7.3. *Thixotropy*

While shear-thinning ensures extrudability, thixotropy dictates the shape fidelity of the printed structure after extrusion. Thixotropy is the time-dependent recovery of viscosity (or modulus) once shear is removed. This is usually quantified using a step test involving three distinct stages with controlled shear rate: first, the initial, high-modulus state G' of the material is measured using a low, non-destructive shear rate; second, a high shear rate is applied to simulate the damage and fluidization that occurs during extrusion; and finally, the test immediately switches back to the

low, non-destructive shear rate, allowing the rheometer to monitor the recovery of viscosity η as a function of time. These three phases correspond to 1–3 in Fig. 23(b), respectively. A desirable bio-ink must recover its η rapidly upon deposition, allowing it to maintain its shape and support the weight of subsequent layers. This same high-low strain methodology is also the standard protocol for quantifying the self-healing behavior of dynamic DN gels [Zheng *et al.*, 2023a].

2.7.4. *Strain sweep*

For the final solid gel, a strain sweep is the mandatory first step in any oscillatory analysis. It is performed by applying an increasing oscillatory strain at a constant frequency. A typical measuring result of a strain sweep test is the moduli as a function of the shear strain, as shown in Fig. 24(a). The purpose of the strain sweep test is to identify the LVR — the strain range at low strains where the moduli are independent of the applied stress, reflecting the material's undamaged network structure. This test provides two crucial pieces of information: establishing the safe

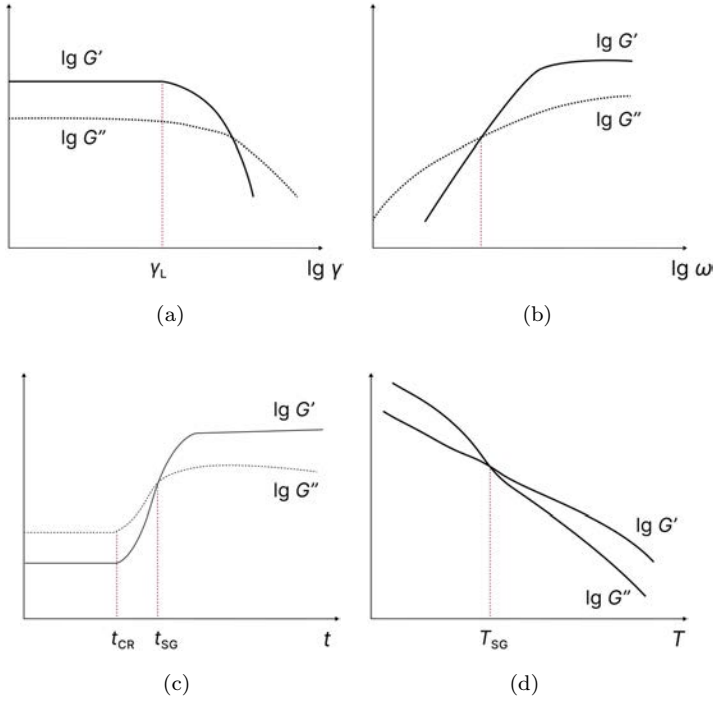

Fig. 24. Rheological analysis of hydrogel viscoelasticity. (a) Strain sweep determining the LVR and linearity limit (γ_{L}). (b) Frequency sweep illustrating microstructural changes as the frequency increases beyond the characteristic crossover point ($G' = G''$). (c) Time sweep monitoring gelation, with t_{CR} marks the reaction onset, and t_{SG} marks the sol-gel transition ($G' = G''$). (d) Temperature sweep demonstrating thermal stability, where the crossover point ($G' = G''$) defines the sol–gel transition temperature (T_{SG}).

non-destructive strain amplitude that must be used for subsequent tests to ensure their validity, and identifying the yield point (where G' begins to drop). This yield point is critical for DN gels as it often corresponds to the onset of network failure, such as the breaking of the sacrificial first network, providing insight into its energy dissipation mechanism.

2.7.5. *Frequency sweep*

Once the LVR is known, a frequency sweep is performed at a constant, low strain. This test reveals the underlying network architecture by determining the relationship between the testing frequency and the G' and G'' moduli [Fig. 24(b)]. For a stable DN hydrogel, a solid-like structure ($G' > G''$) is typically observed, while the emergence of a crossover of G' and G'' indicates that a reversible network may exist in the hydrogel, and the material properties of these hydrogels are typically highly frequency dependent.

2.7.6. *Time sweep*

A time sweep test monitors G' and G'' at a constant frequency and strain over a set period [Fig. 24(c)], used to monitor structural changes. This method has two primary applications critical to DN gels. First, it is essential for studying gelation kinetics, particularly for in-situ forming networks (e.g., via photopolymerization). By tracking the evolution of G' and G'' from a hydrogel precursor, the test can precisely determine the time point t_{CR} at the onset of the chemical reaction, and the time point t_{SG} at the sol/gel transition in terms of the crossover point $G' = G''$. Second, this test is used to assess hydrogel stability, where no significant changes in G' and G'' over time suggest high stability.

2.7.7. *Temperature sweep*

A temperature sweep measures G' and G'' as the temperature is ramped up or down [Fig. 24(d)]. This test is critical for assessing the thermal stability of the DN gels, showing the temperature range where the moduli are stable. Furthermore, for DN gels designed to be thermoresponsive (e.g., those containing PNIPAAm), this test is the standard method to identify the sol–gel transition temperature T_{SG}, which is characterized by the corresponding temperature of the crossover point $G' = G''$.

2.7.8. *Creep recovery and stress relaxation*

Transient tests, such as creep test and stress relaxation test, are vital for assessing the time-dependent mechanical behavior of DN gels, especially for load-bearing applications. The creep test measures the material's compliance by applying a constant static stress and recording the resulting strain deformation over time. The subsequent recovery phase, where the stress is removed, quantifies the hydrogel's

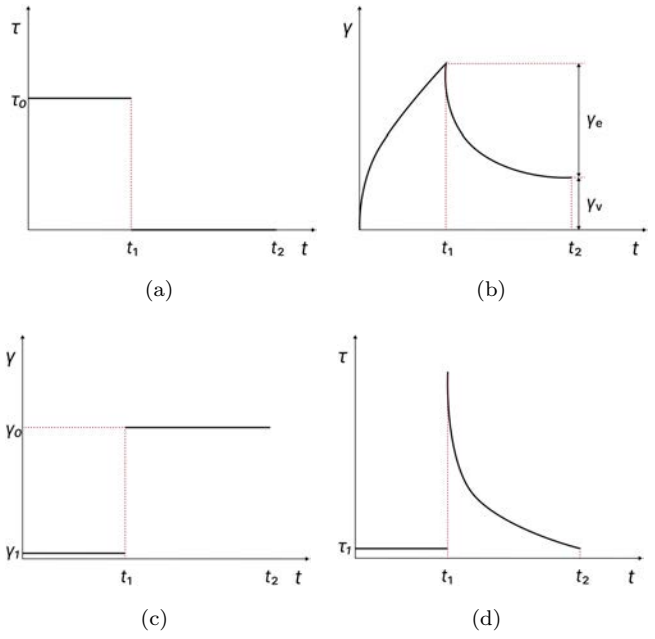

Fig. 25. Creep-recovery and stress relaxation behaviors. (a) Applied stress profile for creep-recovery testing. (b) Typical creep and recovery curve, distinguishing the recoverable elastic deformation (γ_e) from the permanent viscous deformation (γ_v). (c) Applied strain profile used for stress relaxation testing. (d) Typical stress relaxation curve showing stress decay over time.

ability to return to its original state and its resistance to permanent deformation [Figs. 25(a), 25(b)]. Conversely, a stress relaxation test applies a constant strain and measures the decay of the stress exerted by the specimen over time [Figs. 25(c), 25(d)]. It is suggested to apply a low, constant strain γ_1 to the test specimen before performing the large γ_0 step to increase the test reproducibility [Mezger, 2020]. The stress relaxation test directly probes the material's ability to dissipate internal stresses and establishes its time-dependent viscoelastic nature.

2.8. *Non-contact characterization techniques*

The traditional mechanical test is usually limited by the contact sensor and limited spatial sampling, which may affect the surface morphology of DN gel and cause stress concentration, and is not conducive to the study of the mechanical properties of DN gels. The non-contact characterization techniques, often relying on optical or scattering principles, allow for measurement without direct mechanical coupling to the sensor. These techniques avoid the introduction of measurement-induced boundary conditions, thereby preserving the intrinsic mechanical environment of the DN gel specimen. These techniques quantify the evolving stress, strain, and even microstructure of the DN gel during loading with unprecedented spatial-temporal resolution.

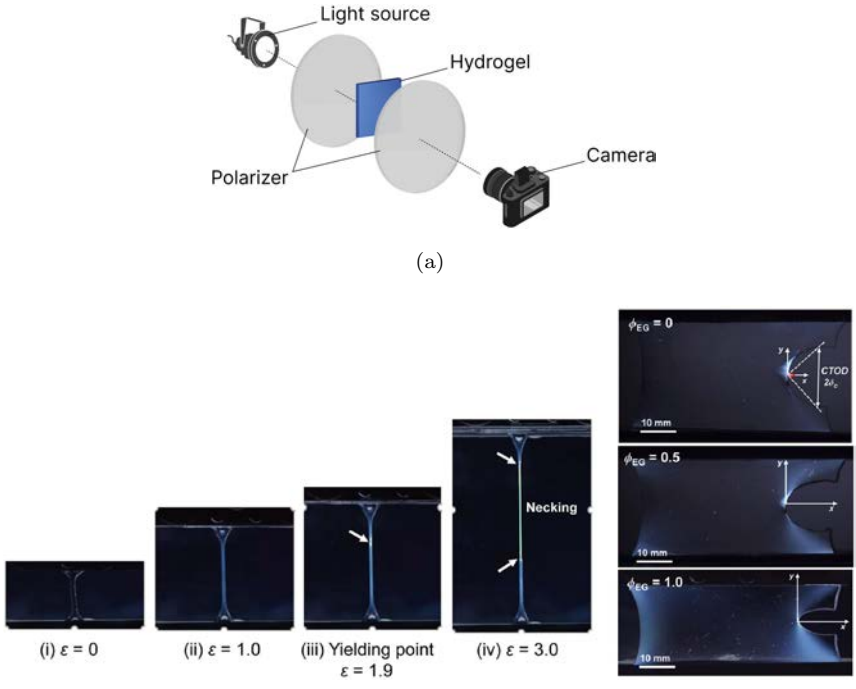

Fig. 26. Visualization of DN gel deformation using birefringence. (a) Schematic illustration of the experimental setup for birefringence observation. (b) Birefringence images of DN gels subjected to uniaxial stretching (left) and pure shear stretching (right) [Zheng *et al.*, 2021].

Source: Reproduced with permission from PNAS.

2.8.1. *Birefringence observation*

The birefringence observation is the most widely used non-contact characterization technique for the DN gels. During birefringence observation, when there is molecular chain orientation inside the DN gel, its refractive index will vary due to different polarization directions, resulting in optical path differences when polarized light passes through (manifested as light and dark stripes or color patterns), and then the anisotropic structure or stress–strain distribution of the DN gel can be studied through the birefringence observation test. The experimental setup shown in Fig. 26(a) is used to perform real-time imaging of birefringence during the tensile process. The DN gel sample is placed between two crossed circular polarized films, and the two films are placed between a white lamp and a video camera. The birefringence during the tensile process is recorded with the video camera (referential setting: 24 frames/s, 1920 × 1080 pixels).

By conducting birefringence observation during the uniaxial tension or pure shear test of DN gels, the size of the necking/yielding zone at the crack tip can

be tracked in real time through birefringence imaging, as there is pronounced orientation of the second network strands in the necking/yielding zone [Lu *et al.*, 2024; Zheng *et al.*, 2024b] [Fig. 26(b)]. Based on this, Zheng *et al.* [2021] studied the effect of chain dynamics on the crack initiation of DN gels and found that the necking zone size and fracture toughness of PNaAMPS/PAAm DN gels can be greatly reduced by increasing the solvent viscosity η_s, the underlying mechanism of which was attributed to the increase of the relaxation time of the second network segment with the increase of η_s, which leads to stress overshoot at the crack tip and premature fracture of the second network. Furthermore, Zheng *et al.* [2024b] used this technique to study the unique stick–slip crack dynamics of DN gels under pure-shear loading. By respectively changing the loading rate and prestretch applied to the DN gels, the authors found that the stick–slip is caused by an energy supply–demand imbalance between "dynamic crack propagation" and "energy dissipation zone reconstruction", and this dynamic fracture can be effectively suppressed by introducing predamage to the brittle first network. A systematic study on the effect of the predamage on the fracture toughness of DN gels also adopted the birefringence observation technique [Zheng *et al.*, 2024a]. Besides, researchers also conducted birefringence observation tests to study the pre-yielding, yielding, and necking process [Lu *et al.*, 2024; Yoshida *et al.*, 2024], and crack growth behavior [Zhang *et al.*, 2022] of DN gels.

2.8.2. *Digital image correlation technique*

Digital image correlation (DIC) can be used to measure the strain field in DN gels, especially for the inhomogeneous local deformation during necking [Ajam *et al.*, 2024; Joseph *et al.*, 2025; Mao *et al.*, 2017; Wang *et al.*, 2025b; Yuan *et al.*, 2025; Zhang *et al.*, 2015]. The general principle of the DIC technique is shown in Fig. 27(a). Images taken successively are compared with each other. The first image is divided into a grid with a fixed mesh size. The grey value of each box of the grid is then measured. On the second image, the software will find the previous grid in the new image. Therefore, the difference between the first grid and its new position in the second grid gives the local displacement field. In Fig. 27(a), in the reference image on the left, a zone of interest is defined, this same zone is tracked by the software in the deformed image, as shown on the right. From this, the local displacement and strain of the zone of interest can be deduced [Fig. 27(b)]. However, for DN gels containing a large amount of water content, creating a durable speckle pattern is usually challenging as the liquidous surface layer may cause pattern smearing. Recently, Wang *et al.* [2025b] proposed a method to produce robust speckle patterns on DN gels by using the lycopodium microparticles, which can ensure a successful capturing of strains up to 1000% during uniaxial deformation of DN gels using the DIC method, both in air and in aqueous environments. Joseph *et al.* [2025] even adopted the DIC method to characterize the strain fields around the interfacial crack tip between two DN gels to understand the opening and shear

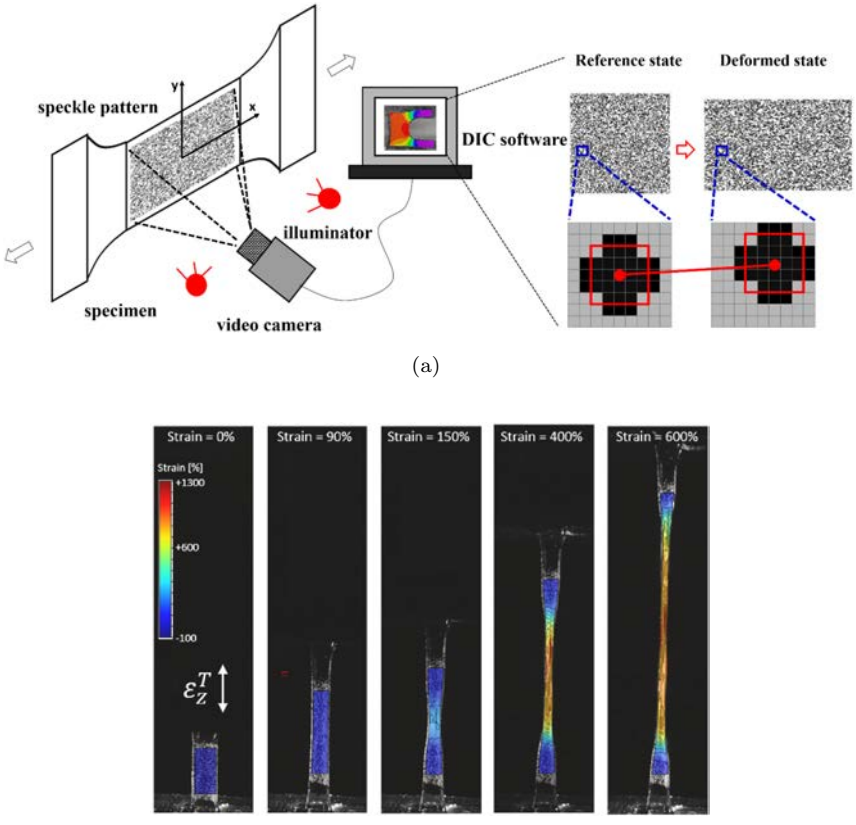

Fig. 27. Strain field measurement using the DIC technique. (a) Schematic illustration of the technique. A random speckle pattern is applied to the specimen surface, and images are recorded at both reference and deformed states. Surface displacement and strain are calculated by matching digital images using correlation software [Zhang *et al.*, 2015]. (b) Representative strain field evolution of a DN gel specimen under uniaxial stretching, measured using the DIC technique [Wang *et al.*, 2025b].

strain field within the fracture process zone and to correlate with fracture toughness values.

2.8.3. *Multi-particle tracking technique*

Although the DIC technique is an effective way to probe the strain field of a material with large deformation by analyzing the motion of speckles within a grid, it is usually limited to measuring the continuous deformation of the material. When discontinuous deformation, such as fracture, occurs, the grid generated in this method often fails, resulting in the loss of strain information in that region. To address this, MPT

has emerged as an effective technique that can probe both the continuous and discontinuous deformation fields of materials with large deformation by analyzing the motion of particles. The MPT technology is adopted as shown in Fig. 28(a). The surface of the specimen is first coated with round tracking particles of the same size, which is considered to have negligible influence on the deformation of the specimen. Then, the specimen is clamped onto the loading machine, and a high-speed camera is set to capture the deformation of the specimen during the experiment process. For continuous deformation scenarios, the camera used a low frame rate, high pixel mode. When the experiment involved the fracture of the specimen, i.e., discontinuous deformation, the camera used a high frame rate, low pixel mode. To enhance the accuracy of the MPT technique, a white light source is often placed behind the sample. The strain field of the specimen is obtained by using the multi-particle matching algorithm. Specifically, the particle coordinates of two consecutive photos are matched by a topology-based particle tracking algorithm [Patel *et al.*, 2018]. All particles are matched in order. Then, we calculate the displacement component of each particle according to the matching results. The incremental displacement component is the displacement relative to the previous photo. Next, using the moving least square method, the displacement component of the matching failed particle is interpolated by using the displacement component of the successful matching particle to ensure that the particle on each image has an effective displacement. Finally, synthesize the displacement results of particles on all photos, and accumulate the absolute displacement field of particles on each photo relative to that on the first photo. According to the absolute displacement field, we calculate the partial derivative of the displacement field relative to the coordinate and obtain the strain field result. Using the MPT technique, Wang *et al.* [2025a] probed the strain field of the DN gel specimen during its whole uniaxial tension process, from which the pre-necking, necking, and hardening stages can be clearly specified [Fig. 28(b)]. Based on this, they further developed a damage constitutive model that can successfully account for the inhomogeneous deformation of DN gels during the necking stage, either under monotonic or cyclic loading.

2.8.4. *Small-angle scattering tests*

The SAS measurement, including small-angle X-ray scattering (SAXS) and small-angle neutron scattering (SANS), probes nano-to-micrometer scale structures by measuring the intensity distribution of an incident beam (X-rays or neutrons) scattered at very small angles after passing through a sample. A typical setting of the SAS test is shown in Fig. 29(a). SAS usually measures the scattered intensity I as a function of the scattering vector q. q is related to the scattering angle and the radiation wavelength. A smaller value of q corresponds to larger structural features, while a larger q value probes smaller structural details. Standard SAXS/SANS instruments typically probe structures in the 1–100 nm range. Probing larger structures up

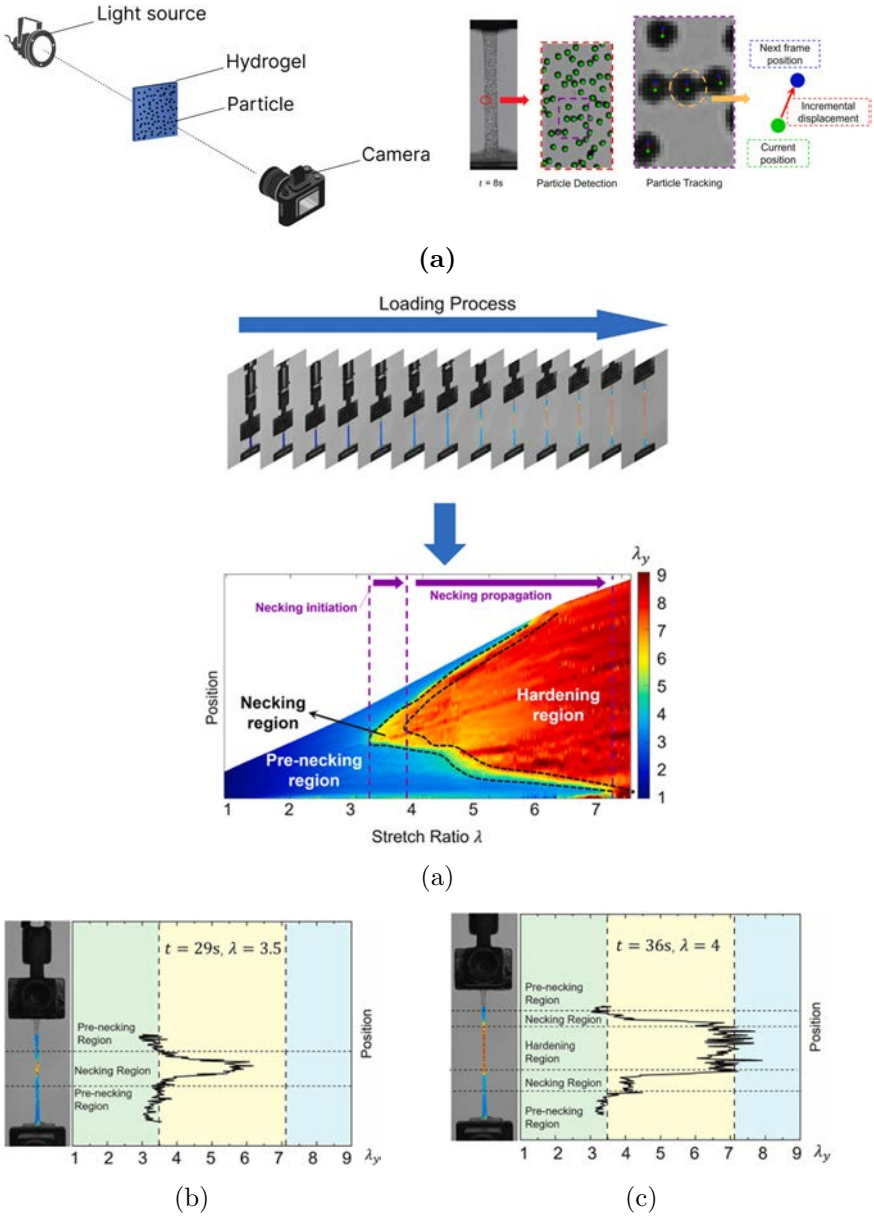

Fig. 28. Strain measurement using the MPT technique. (a) Schematic illustration of the technique. Discrete particles are randomly spread onto the specimen surface, and the deformation process is recorded via a camera. Displacement and strain fields are computed by detecting and tracking particle positions using an algorithm. (b) Evolution of the stretch distribution along the loading direction of a DN gel during uniaxial tension. The corresponding 2D and 1D stretch distribution maps at t= 29s (top) and t= 36s (bottom) are shown [Wang *et al.*, 2025a].

Source: Copyright 2025 Elsevier.

to 1 μm requires specialized ultra-small angle scattering (USAXS/USANS) instruments [Hammouda, 2010], which access a lower q-range.

The microstructure of DN hydrogels can be measured using SAS experiments, and this information can often provide a microscopic perspective on the mechanical behavior of DN gels, helping to understand their performance enhancement mechanism. Researchers performed static and dynamic structural analysis through SANS and USANS tests on DN gels and their components without and with pure shear deformation [Tirumala *et al.*, 2008; Tominaga *et al.*, 2007]. Experimental results indicated that during deformation, the PAAm chains form reversible, periodic fluctuations with a spacing of $\sim$ 1.5 μm, while the PAMPS network undergoes irreversible, permanent structural damage [Fig. 29(b)]. Furthermore, scattering intensity reveals that the fluctuations on PAMPS networks and PAAm chains are out-of-phase, indicating that the PAAm-rich regions correspond to the PAMPS-deficient (fractured) regions. These experimental results indicate that the two-component networks of DN gels may be associated via molecular interactions, e.g., hydrogen bonds, which help them to self-regulate by breaking these associations to form a periodic structure, thereby dissipating a large amount of energy throughout the specimen and preventing crack propagation. Later, they quantitatively measured the thermodynamic interactions between the component networks using SANS measurement and validated the weak thermodynamic interactions between two component networks [Tominaga *et al.*, 2008] and proposed a stress transfer model for the toughness enhancement of DN gels based on these SANS experimental results [Tirumala *et al.*, 2008]. Using SANS tests, Tominaga *et al.* [2014] also investigated water absorption in freeze-dried DN gels and identified a characteristic network mesh size of approximately 8 nm. Their finding revealed a two-stage absorption process of DN gels. At low humidity, i.e., when relative humidity (RH) is lower than 68%, water molecules only absorb onto larger structures ($>$ 8 nm), while at high humidity (RH¿68%), they begin to penetrate the smaller, internal mesh ($<$ 8 nm) and interact directly with the polymer segments.

Although SANS can characterize the microstructure of DN gels well, SAXS may be a more convenient method when conditions permit. For example, King *et al.* [2020] employed SAXS to quantitatively measure the degree of orientation of the physical sacrificial network (PBDT) in the anisotropic double-network hydrogels. The scattering patterns confirmed the successful induction of an oriented structure upon pre-stretching, and the data were used to calculate a structural anisotropy factor which correlated directly with the observed mechanical anisotropy of the hydrogels. Using the in situ SAXS, Fukao *et al.* [2020] analyzed the microscopic structural changes in PAMPS/PDMAAm DN gels during uniaxial stretching and found that the relative strength of the two networks dictates the internal fracture process, either leading to localized strain amplification and necking in specimens with low second network concentration (DN-2), or to dispersed, homogeneous fracture, in specimens with high second network concentration (DN-4) [Fig. 29(c)].

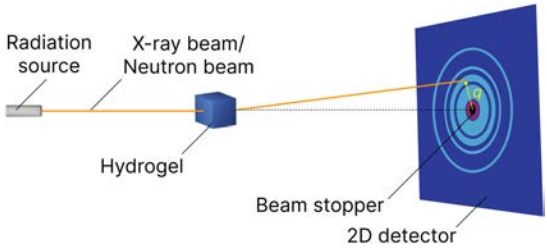

(a)

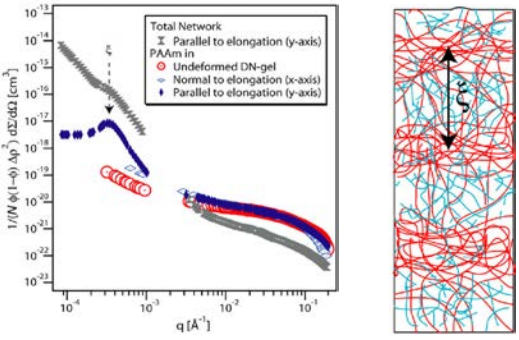

(a) (b)

(b)

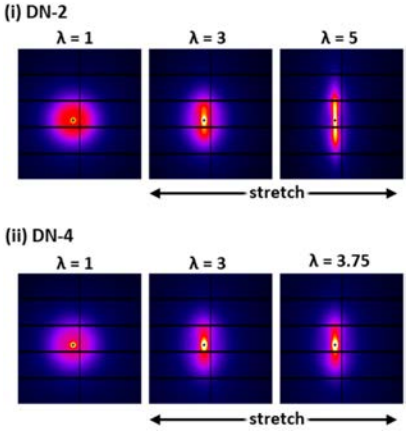

(c)

Fig. 29. (Color online) Structural characterization of DN gels using SAS. (a) Schematic illustration of a SAS instrument (applicable to both SAXS and SANS). (b) SANS profiles of PAMPS/PAAm DN gels in undeformed and pure shear deformation states. Blue and red lines represent PAMPS and PAAm networks, respectively. The correlation length ξ, derived from the peak position in the deformed gel, corresponds to concentration fluctuations in the component structure of PAAm at $\approx 1.5\mu$m [Tominaga *et al.*, 2007]. (c) Representative 2D SAXS images of PAMPS/PDMAAm DN gels under uniaxial stretching [Fukao *et al.*, 2020].

Source: Copyright 2020 American Chemical Society.

Besides SAS, other scattering methods such as dynamic light scattering [Furukawa *et al.*, 2008; Huang *et al.*, 2007; Na *et al.*, 2004] are also widely used in the study of DN gels. However, DSL is mainly used to capture dynamic information in the structure of DN gels, such as molecular motion and relaxation modes, and will not be elaborated here.

2.8.5. *Mechanochemistry method*

Mechanochemistry has recently emerged as a reporting tool of damage or of local stress in soft materials during deformation or macroscopic crack propagation [Davis *et al.*, 2009; Ducrot *et al.*, 2014; Stratigaki *et al.*, 2020]. The idea is simple in principle that certain suitably designed molecules chemically incorporated (e.g., as crosslinkers) into materials can change their light absorption spectrum, become fluorescent, or emit light when a mechanical stimulus is applied, and these molecules are called mechanophores. In other words, these force-responsive mechanophores can be used as a force sensor or detectors of bond breakage or stress concentration.

Not until recently, researchers started to apply this method to investigate DN gels and gained insightful results. By covalently incorporating a hydrophobic rhodamine derivative (Rh mechanophore) into the first network of DN gels as the crosslinker, Wang *et al.* [2020] endowed DN gels for the first time with stress-sensitive, freezing-induced mechanochromic and pH-regulated mechanochromic properties [Fig. 30(a)]. Later, by embedding cyclobutene-based mechanophore crosslinkers with varied activation forces in the first network of DN gels, Wang *et al.* [2024b] quantitatively investigated the role of activation forces in the activation competition among mechanophores within a polymer network. When a single mechanophore is incorporated as the crosslinker, a lower activation force relative to the bonds in the polymer main chain results in higher activation efficiency and sensitivity. When two mechanophores are incorporated, mechanophore activation faces the competition from the other mechanophore and non-specific bond cleavage in the backbone, and the weak mechanophores can completely suppress the activation of a stronger mechanophore and stronger bond cleavage in the backbone.

Through the combination of mechanoradical polymerization and fluorescence microscopy, Matsuda *et al.* [2020] propose a novel mechanochemical technique for the visualization and quantification of the bond scission in DN gels [Fig. 30(b)]. They adopted the mechanoradicals that were generated by homolytic covalent bond scission to initiate the radical polymerization of the *N*-isopropylacrylamide (NIPAAm) monomers in the DN gel, which formed a thermoresponsive polymer PNIPAAm tethered to the broken ends of the first-network strands. The distribution of PNIPAAm records the internal fracture around the crack tip during the crack opening and propagation, and is then visualized using an environment-responsive fluorescent probe, 8-anilino-1-naphthalenesulfonic acid (ANS), at a temperature above its lower critical solution temperature (LSCT). Using a laser scanning confocal microscope

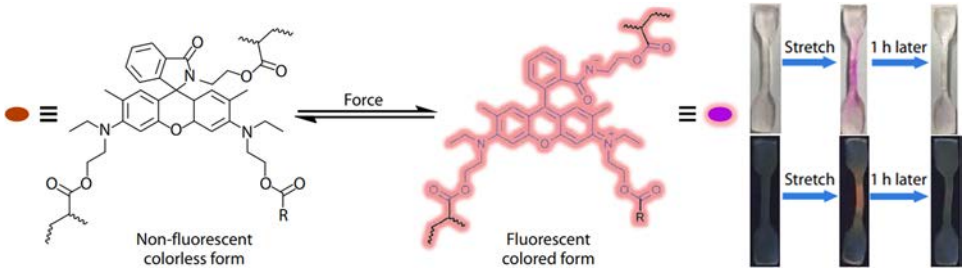

(a)

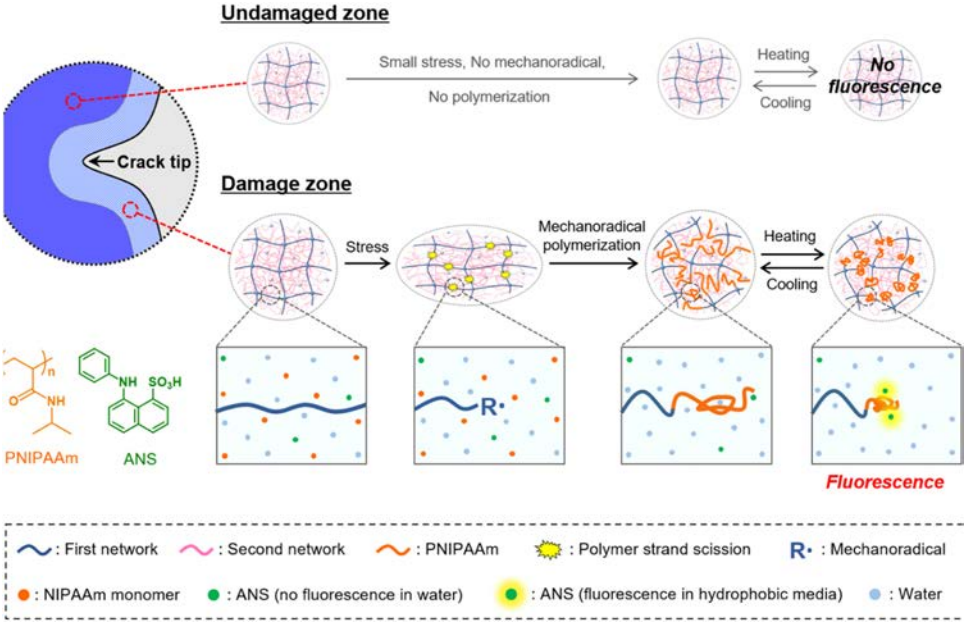

(b)

Fig. 30. Visualization of internal damage in DN gels using the mechanochemistry method. (a) Chemical structure and mechanochromic/mechanofluorescent response of a Rh mechanophore-functionalized DN gel [Wang *et al.*, 2020]. (b) Schematic illustrating the damage visualization mechanism. Mechanoradicals generated by strand scission initiate the polymerization of NIPAAm to form thermoresponsive PNIPAAm. The fluorescent probe ANS binds to hydrophobic PNIPAAm domains formed above the LCST, selectively visualizing the damaged region while the undamaged region remains dark. (c) 3D fluorescence images obtained using a laser scanning confocal microscope around the crack tip of a torn DN gel containing NIPAAm and ANS, observed at 42°C. (d) Profile of dissipated mechanical energy density in the damage zone, obtained by calibrating fluorescence intensity using tensile data [Matsuda *et al.*, 2020].

Source: Copyright 2019 Chinese Chemical Society Institute of Chemistry. Copyright 2020 American Chemical Society.

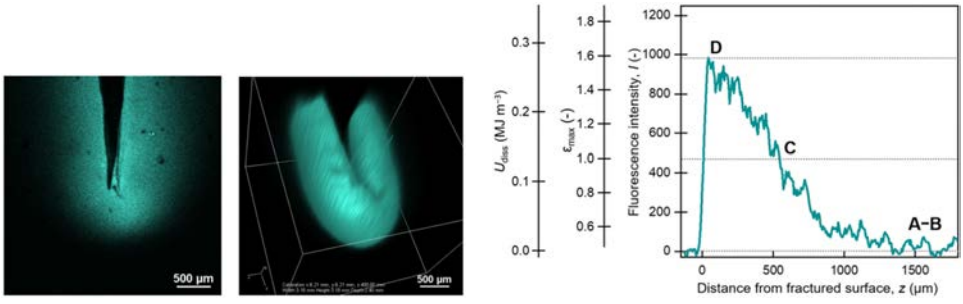

(c) (d)

Fig. 30. (*Continued*)

(LSCM), even three-dimensional damage distribution can be captured [Fig. 30(c)]. In addition, by calibrating the fluorescence intensity using tensile data, the profiles of the maximum strain and stress imposed, and the dissipated mechanical energy density in the damage zone of a DN gel can be quantitatively estimated with a resolution of around 50 μm [Fig. 30(d)]. Furthermore, by comparing the dissipated energy in the damage zone around the crack tip of the DN gel obtained from this method with the fracture energy obtained from the tear test, Matsuda *et al.* [2021] found that in addition to energy dissipation in a relatively narrow yield region, the dissipation in the wide preyielding region and the intrinsic fracture energy also have a large contribution to the fracture energy, and the intrinsic fracture energy is comparable to the dissipated energy and way much larger, instead of comparable, to the fracture energy of the second network.

Despite insightful results obtained by the mechanochemistry method, the use of this method as a tool to investigate the mechanical behavior of DN gels remains in its infancy. The method has obvious disadvantages as it usually requires a relatively complicated procedure, and the existing method for DN gels is based on posterior observation instead of real-time observation. However, it does not require the incorporation of specific mechanophores into the polymer network, and the posterior observation may help to characterize the complicated deformation of high-speed fracture of DN gels by recording the fracture history [Matsuda *et al.*, 2020]. In addition, compared to the optical measurement technology mentioned in Sec. 2.8, the mechanochemical method can achieve quantitative measurement with high spatial accuracy, and both 2D and 3D characterization, all at the same time.

While the development of these non-contact characterization methods has greatly facilitated our understanding of the deformation and toughening mechanisms of DN gels, sometimes contact or even invasive methods also have their advantages. For example, the microelectrode technique, developed in recent years, inserts extremely fine glass microelectrodes (with tip sizes typically in the submicron to micron range) into the interior of the hydrogel. Since the primary network of the DN

gel is a charged polyelectrolyte, its internal potential (Donnan potential) is directly related to the local charge density (i.e., polymer concentration). By analyzing and measuring the potential changes at the depth of measurement, the breakage and distribution of the primary network can be indirectly quantified. For example, Guo *et al.* [2019] investigated the internal damage evolution of double-network hydrogels under uniaxial stretching by measuring the electric potential distribution of reswollen samples using the microelectrode technique. It reveals that the polymer network transitions from a homogeneous structure to a heterogeneous bimodal state composed of minor and major damaged regions as strain increases. Furthermore, the analysis of the transition zone suggests that necking initiates at the gel surface and propagates into the depth. Recently, Nishimura *et al.* [2024] utilized the microelectrode technique to spatially visualize the three-dimensional damage distribution of the brittle first network near the crack tip of a torn DN gel. It revealed distinct fracture behaviors along the thickness direction: a pre-yield zone characterized by local necking with alternating fractured layers, and a yield zone exhibiting global necking with homogeneous fragmentation. These findings provide the first quantitative demonstration of how two-stage energy dissipation in the damage zone contributes to the material's toughness. Therefore, there is no superiority or inferiority between non-contact and contact characterization methods; it all depends on the requirements.

2.9. *Comparison of different experimental methods*

The comprehensive characterization of DN gels requires a systematic understanding of various experimental methods, as each provides distinct advantages across different length scales. Table 1 summarizes the test scale, key properties measured, and advantages/insights provided by each method. Conventional mechanical testing methods, such as uniaxial tension, compression and pure shear tests, serve as the foundation for mechanical characterization, providing bulk mechanical properties including elastic modulus, work of fracture, energy dissipation, fracture toughness, fractocohesive length, fatigue properties and crack growth behavior. Single-edge notch tests are also employed to measure fracture toughness, fatigue properties, and flaw sensitivity, proving particularly useful when sample size or testing space is limited. Trouser tear tests are particularly effective for measuring fracture toughness and fatigue behavior under controlled crack propagation. For DN gels containing dynamic bonds, the rheology test is a powerful tool for probing flow and deformation properties, such as thixotropy and viscoelasticity. Interfacial and surface characterization methods complement bulk tests by focusing on adhesion and tribological behaviors. Specifically, adhesion tests measure interfacial toughness and strength, while tribological tests assess friction and wear behaviors at the interface between DN gels and solid substrates. Furthermore, coupling conventional mechanical tests with advanced non-contact characterization techniques enables a deeper exploration of the mechanical properties of DN gels.

Table 1. Summary of experimental methods for characterizing DN gels.

EXPERIMENTAL METHOD	PROBING SCALE	KEY PROPERTIES MEASURED	ADVANTAGES/ INSIGHTS
UNIAXIAL TENSION & COMPRESSION	Macroscale	Elastic modulus, work of fracture, energy dissipation	Foundational for bulk mechanical property characterization
PURE SHEAR	Macroscale	Elastic modulus, fracture toughness, fractocohesive length, fatigue properties, crack growth behavior	Foundational for bulk mechanical property characterization
SINGLE-EDGE NOTCH	Macroscale	fracture toughness, fatigue properties, flaw sensitivity	Useful when experimental samples or space are limited
TROUSER TEAR	Macroscale	Fracture toughness, damage zone, components of fracture toughness and damage zone	Effective for measuring properties under controlled crack propagation
ADHESION	Macroscale	Interfacial toughness, interfacial strength, fatigue properties	Focuses on interfacial and surface properties
TRIBOLOGICAL	Nano-to macroscale	Coefficient of friction, wear behaviors	Assesses behavior at the interface between the material and solid substrates
RHEOLOGICAL	Macroscale	Rheological properties, viscoelasticity, self-healing	A powerful tool for probing flow and deformation properties of dynamic materials
NON-CONTACT CHARACTERIZATION (BIREFRINGENCE, DIC, MPT, SAS, MECHANOCHEM-ISTRY.)	Nano- to macroscale	Damage zone, stress, strain, and dissipated energy density distribution, microstructure evolution	Bridges length scales by providing detailed, spatially resolved insights into deformation behaviors.

These experimental methods operate across different length scales, thereby offering complementary information. Macroscopic tests, such as uniaxial tension and compression, pure shear, single-edge notch, trouser tear, adhesion, tribological, and rheological tests, typically use specimens on the order of 10–100 mm to capture overall deformation processes. Non-contact characterization technologies, including birefringence observation, DIC, MPT, SAS and mechanochemistry techniques, bridge macro- and microscales by resolving localized damage zones with a high spatial resolution (1 nm–10μm), providing more detailed insight into the deformation behaviors that occur during macroscopic testing.

Worth noting that individual experimental methods can be used to measure multiple mechanical properties, while a single mechanical property can be measured by

various methods. For instance, the fracture toughness of DN gels can be measured using pure shear, single-edge notch, trouser tear, or even peel tests. Although results from different methods may not be identical due to different stress states, they generally agree in magnitude. In practice, the selection of methods primarily depends on objectives. For fundamental studies, integrating conventional testing with non-contact techniques provides the most comprehensive understanding of DN gels. In engineering practice, the selection of characterization methods is dictated by the specific requirements of the end-use system. For example, in the development of artificial cartilage, high-cycle fatigue testing is prioritized to predict the long-term durability required for load-bearing implants, ensuring they can withstand millions of physiological cycles without failure; for DN hydrogels utilized as drilling fluid plugging agents in the oil and gas industry, rheological tests are critical for validating seal integrity in harsh downhole environments; in the rapid prototyping of soft robotic actuators, non-contact optical techniques (such as DIC or MPT) are pivotal for identifying stress concentrations in complex, irregular geometries. These examples demonstrate how the reviewed methodologies are directly translated into validation protocols for real-world products.

3. Computational Methods for Studying Mechanical Properties

3.1. *Molecular dynamics method*

MD method serves as a crucial bridge connecting microscopic molecular structures to macroscopic material properties, playing a key role in revealing the strengthening and toughening mechanisms, anti-freezing mechanisms, and functional designs of DN gels. Based on the scale of the study, relevant research can be generally categorized into all-atom simulations, CG simulations, and multiscale simulations.

3.1.1. *All-atom simulations*

AAS offer the highest level of chemical and physical detail by explicitly modeling monomers, crosslinkers, and water at the atomic scale [Fig. 31]. These models typically employ advanced force fields, such as the condensed-phase optimized molecular potential (COMPASS) or Dreiding, to accurately capture specific intermolecular interactions. To mimic experimental curing and achieve equilibrated network structures, researchers often utilize cyclic NPT (Isothermal-Isobaric Ensemble) and NVT (Canonical Ensemble) simulations combined with thermal annealing protocols, which involve starting from high temperatures and cooling down. Networks are generally pre-assembled or grown in silico (e.g., via pre-crosslinking or algorithmic polymerization), and the system is solvated with explicit water molecules and counterions. This approach enables the detailed characterization of mechanical properties (e.g., stress–strain curves), transport properties (e.g., self-diffusion coefficients, SDCs), and solvent structures (e.g., radial distribution functions, RDFs).

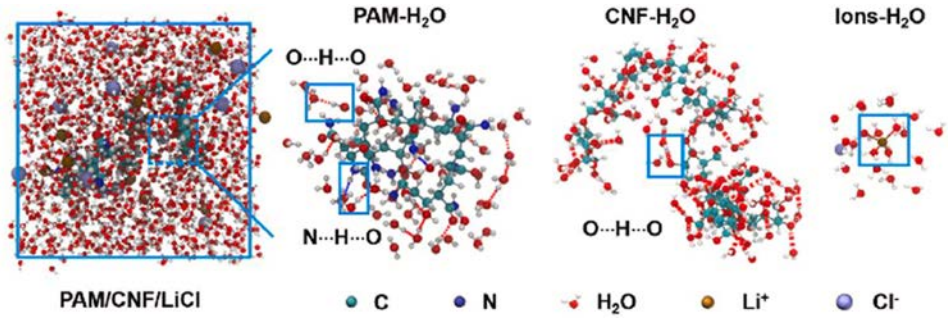

Fig. 31. All-atom MD simulations of the PAM/CNF/LiCl hydrogel. Equilibrium structures of the hydrogel and the interactions of each component with water are displayed [Ge *et al.*, 2021].

Source: Copyright 2020 Elsevier.

AAS have been extensively utilized to elucidate the critical role of hydrogen bonding in governing the mechanical properties of DN gels. For instance, researchers employed RDFs and binding energy calculations to confirm that the formation of a large amount of hydrogen bonds within DN gels is a key factor in enhancing hydrogel toughness and modulus [Wang *et al.*, 2024a; Wu *et al.*, 2024]. Additionally, simulations by Jia *et al.* [2025] revealed that acid-induced treatment increases hydrogen bond density within polymer networks while reducing electrostatic repulsion, thereby strengthening the DN gels. For nanocomposite DN gels, Xu *et al.* [2022] analyzed the non-bonded interaction energy between silica nanoparticle surfaces and PAM/PAA polymer chains, clarifying the reinforcement mechanism of nanoparticles acting as physical crosslinking points. Furthermore, by analyzing the dynamic behavior of confined water molecules, AAS helps reveal the underlying mechanisms of freeze and dehydration tolerance of DN gels [Ge *et al.*, 2021; Liu *et al.*, 2023; Zhou *et al.*, 2022].

Beyond mechanical reinforcement and environmental stability, AAS provide thermodynamic insights into network behaviors. JaramilloBotero *et al.* [2010] calculated the entropic and enthalpic contributions to elastic responses, viscosities and stress–strain characteristics, offering a thermodynamic explanation for the mechanical enhancement mechanisms in DN gels. AAS have also been effectively applied to screen DN gels for specific adsorption functions. For example, Huang *et al.* [2022] calculated the binding energy between various natural polymer functional groups and the explosive components, identifying carrageenan as the optimal backbone material. Regarding transport phenomena, Jang *et al.* [2007] simulated solute diffusion (e.g., glucose) within DN gels, finding that solute diffusion rates are significantly lower than in SN gels due to the reduced mesh size of DN gels.

Collectively, these all-atom studies elucidate the microscopic origins of DN gels' superior mechanical properties by capturing explicit chemical details. However, inherent spatiotemporal limitations and high computational costs restrict AAS

to small scales, often precluding the investigation of realistic chain entanglement, macroscopic crack propagation, and long-term structural evolution.

3.1.2. *Coarse-grained simulations*

CGS simplify the atomistic details by mapping groups of atoms into single interaction sites (beads), typically employing bead-spring models and Lennard-Jones potentials. This reduction in degrees of freedom facilitates the investigation of network topology evolution, fracture processes, and dynamic behaviors across significantly larger spatiotemporal scales than those accessible via AAS.

CGS have been instrumental in visualizing the microscopic fracture process and validating the strengthening and toughening mechanisms of DN gels. Higuchi *et al.* [2018] utilized CGS to visualize the fracture process of DN gels during stretching, thereby verifying the "sacrificial bond" principle [Fig. 32]. They further analyzed how network concentration and cross-linking density of DN gels influence their void formation and stress–strain behavior. Building on this, Li *et al.* [2020] highlighted the critical roles of inter-network interaction strength and first-network stiffness in enhancing modulus and fracture stress. Recently, Gong *et al.* [2025] reproduced the characteristic pre-necking, necking, and strain hardening behavior of DN gels during the stretching process, quantitatively attributing energy dissipation to the fracture of the first network and the chain orientation of both networks.

Beyond basic fracture mechanics, simulations reveal that stress redistribution in DN gels is highly inhomogeneous. Tauber *et al.* [2021] discovered that the fracture of sacrificial chains occurs in two distinct steps, governed by intra-network and inter-network load sharing, respectively. Their findings emphasize that topological constraints between networks are crucial for enhancing the macroscopic stress

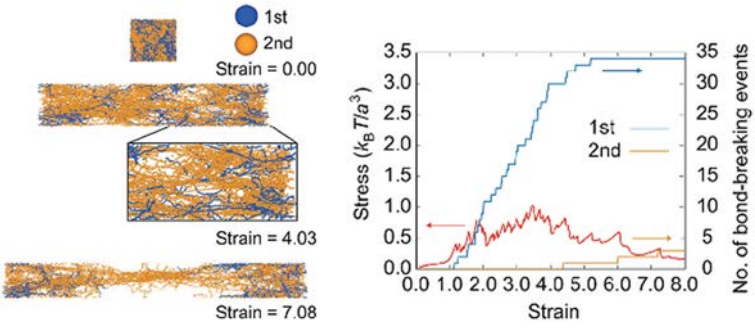

(a) (b)

Fig. 32. CG MD simulations of PAMPS/PAAm DN gels. The fracture process of a DN gel composed of 20% first network and 80% second network is shown, alongside the corresponding stress–strain curve and the evolution of bond-breaking events in each network [Higuchi *et al.*, 2018].

Source: Copyright 2018 American Chemical Society.

response, which deviates significantly from affine deformation predictions. Furthermore, in the context of self-strengthening DN gels triggered by mechanochemical reactions, Wang *et al.* [2025c] elucidated the competitive relationship between the rate of new network formation and crack propagation, demonstrating that effective self-strengthening requires the network formation to outpace crack extension.

CGS are also widely employed to guide synthesis strategies of DN gels. For instance, Jian *et al.* [2023] demonstrated that reducing the ionic crosslinking rate improves spatial homogeneity and overall ionic crosslinking density, thereby toughening the DN gels. Similarly, Wan *et al.* [2018] identified optimal stiffness ratios and concentrations of two networks to maximize mechanical performance of DN gels, while Xing *et al.* [2021] verified that mechanochemical coupling and self-healing kinetics significantly influence viscoelastic behavior. Additionally, for hybrid physical-chemical DN gels, Zhao *et al.* [2020] revealed that physical interaction clusters dissociate to dissipate energy in the early stages of deformation, while the chemically cross-linked network bears the main stress in later stages.

In summary, the primary advantage of CGS lies in its ability to explore qualitative mechanisms over extended length and time scales, allowing researchers to observe bond breakage sequences and network delocalization in systems comprising thousands of beads. However, a notable limitation is the omission of chemical specificity, such as explicit hydrogen bonding and water structuring, meaning that fine interactions must be carefully parameterized.

3.1.3. *Multiscale simulations*

MS aim to bridge the gap between the macroscopic synthesis parameters (e.g., reaction kinetics) and the microscopic molecular structures (e.g., network topology) by employing specialized algorithmic designs. This approach effectively circumvents the limitations inherent in traditional pre-assembled models, enabling the construction of DN topologies that more accurately reflect experimental synthesis conditions.

A key advancement in this domain is the development of the random walk reactive polymerization (RWRP) algorithm [Liu *et al.*, 2023; Zhang *et al.*, 2021]. Zhang *et al.* [2021] first applied this method to simulate the free radical polymerization process of monomers, encompassing initiation, chain propagation, and cross-linking, at the mesoscopic scale. This method allowed them to generate all-atom agar/polyacrylamide (agar/PAM) DN gel models with realistic topological features, such as chain entanglement and physical interpenetration. By coupling this constructive algorithm with steered molecular dynamics (SMD), they successfully simulated tensile fracture processes at the atomic level, revealing synergistic energy dissipation mechanisms involving chain pull-out and hydrogen bond rupture. As shown in Figs. 33(a)–33(c), the simulated stress–strain curve showed clear yielding and plateau behaviors akin to experiment.

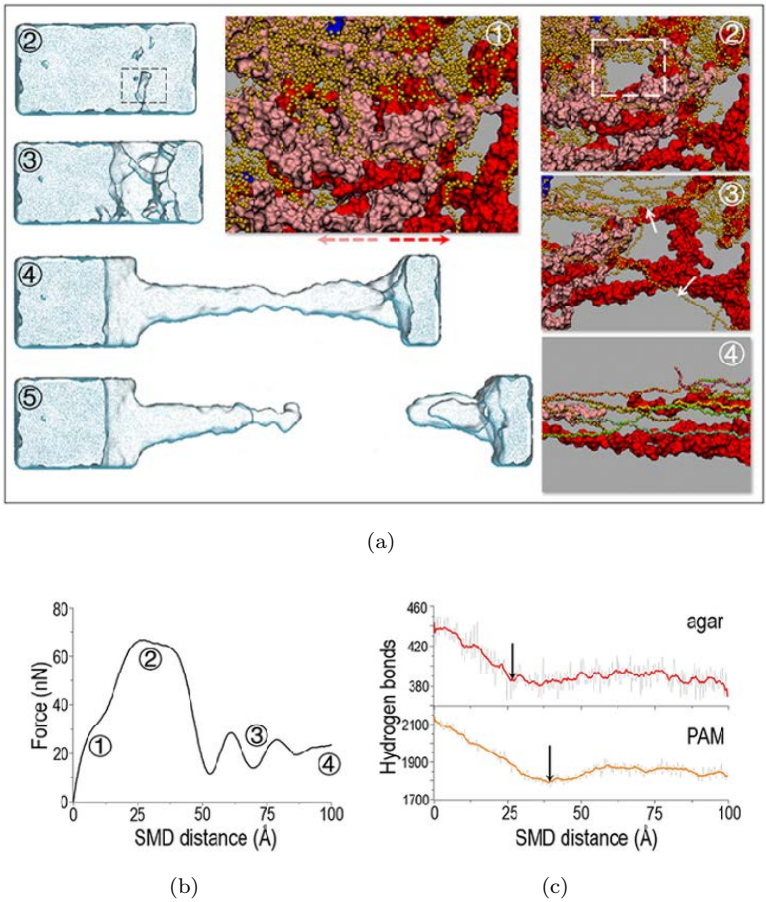

(a)

(b)

(c)

Fig. 33. Multiscale MD simulations of Agar/PAm DN gels. (a) Representative snapshots of DN gels at characteristic points: jyielding, kfracture, lcrack propagation, and mfracture. (b) Force–distance curve characterizing the fracture process. (c) Evolution of the number of hydrogen bonds in the two networks as a function of applied distance Zhang *et al.* [2021].

Building on this framework, Liu *et al.* [2023] further advanced the RWRP algorithm to construct physically-chemically linked polyvinyl alcohol/poly(*N*-(2-hydroxyethyl) acrylamide) (PVA/PHEAA) DN gels from monomers. This study utilized the multiscale approach to directly link polymerization kinetics to the final network topology and its interaction with water molecules. By generating realistic network structures with varying water contents, the researchers were able to perform subsequent AAS to investigate water dynamics and distribution. This multiscale workflow successfully elucidated the anti-freezing mechanism, demonstrating how the specific network topology (formed via RWRP) and strong polymer–water interactions collaboratively inhibit ice nucleation.

Collectively, these multiscale approaches effectively bridge the timescale of polymerization reactions with the structural scale of MD, providing critical molecular-level guidance for the rational design of DN gels. However, it is worth noting that multiscale simulations are computationally demanding. Constructing a DN network ab initio requires numerous incremental steps, and the resulting systems remain nanoscopic with relatively short simulation times, which prevents the direct observation of macroscopic crack propagation. Furthermore, the linking of different models introduces potential challenges, as parameter mismatches can occur if integration is not carefully managed.

3.2. *Network simulation method*

The DN gel possesses a complex network structure characterized by two interpenetrating networks with distinct physical and chemical properties. Its deformation and fracture behaviors, such as necking, hardening, and damage evolution, exhibit high nonlinearly and microscopic complexity. Although early theoretical frameworks based on the ideal Arruda–Boyce eight-chain model [Arruda and Boyce, 1993] provided a foundation, they often struggle to capture the impact of internal defects and non-affine deformations under large deformation.

To address these challenges, a series of works has been devoted to completing the stochastic structure modeling of networks by constructing a mesoscale network model of DN gels. This approach, known as network simulation, allows researchers to reveal how the mesoscopic chain structure determines the macroscopic mechanical performance. The foundation of this field was established by the periodic random network (PRN) model developed by Lei *et al.* [2021a], which broke the ideal network hypothesis of the traditional Arruda–Boyce model. They proposed a mesoscopic network mechanics method that reproduces the entire large deformation and fracture process of cross-linked elastomers. Key to this method was the introduction of a hybrid total energy form, which combines polymer chain free energy with volumetric deformation energy, to resolve the computational challenges of high incompressibility, alongside a defined stretch criterion to realize chain scission.

To provide a robust physical basis for such discrete fracture simulations, Lei and Liu [2024] further elucidated the theoretical mechanisms of damage of DN gels. They developed a chain scission-induced anisotropic damage constitutive model, which revealed that damage originates from the successive scission of polymer chains due to the inherent randomness of the network structure. By deriving a probability density function for the initial stretch ratio of chains, they demonstrated that damage is highly anisotropic and dependent on the deformation history, thereby validating the use of stretch-based criteria in mesoscopic simulations.

Building on this established framework of mesoscopic mechanics and damage theory, recent studies have utilized network simulations to visualize and quantify the fracture process of DN gels. Li et al [2024a] extended the method to DN gels by introducing shared cross-linking points to simulate physical entanglement

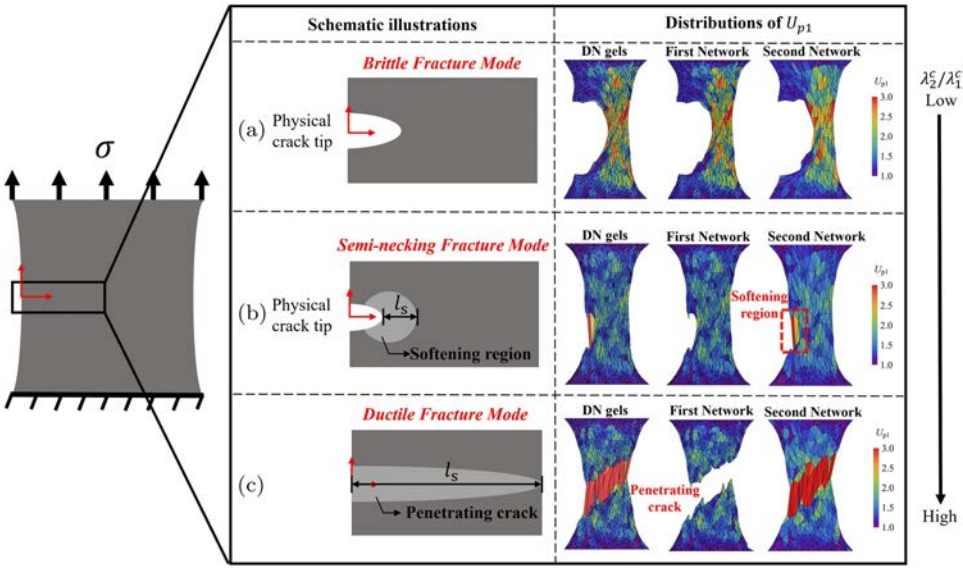

Fig. 34. Microstructure-based fracture models and corresponding stretch contours for DN gels. The figures illustrate three distinct fracture modes: (a) brittle fracture, (b) semi-necking fracture, and (c) ductile fracture [Li *et al.* 2024a].

Source: Copyright 2024 Elsevier.

between the two networks. They identified the stretch criterion ratio between the second and first networks (λ_2^c/λ_1^c) as the critical "knob" governing the macroscopic fracture mode. Their simulations revealed a transition from brittle fracture (when the ratio is low) to a ductile mode characterized by distinct pre-necking, necking, and hardening stages (when the ratio is high) [Fig. 34]. Furthermore, they quantified that increasing the structural uniformity of the first network significantly enhances toughness by mitigating local stress concentrations. This work clarified the micro-critical conditions for brittle-ductile transition and provided microstructure-based fracture models from the perspective of network simulation.

Complementing this phenomenological understanding with fundamental physics, Walker and Fielding [2025] recently employed a mesoscale model to elucidate the suppression of crack propagation in DN gels. They proposed that the underlying toughening mechanism is the reduction of the Eshelby stress propagator. In an SN, the failure of a bond propagates stress to its neighbors, triggering a cascading macroscopic crack. In contrast, their simulations showed that in a DN gel, the soft matrix network shares the load, delocalizing the stress and inhibiting this propagation. This mechanism suppresses brittle failure, favoring ductile deformation via diffusely distributed microcracks.

In conclusion, the network simulation has provided a powerful tool for bridging the microscopic nature and macroscopic mechanical properties of DN gels.

By integrating proper free energy of an abstract polymer chain and chain fracture criteria, network simulation has completed the jump from affine to non-affine assumptions and shows great advantages to characterize the fracture initiation and propagation behavior of DN gels due to its intrinsic discontinuity.

3.3. *Finite element method*

The FEM has emerged as an indispensable numerical tool for predicting the nonlinear mechanical behaviors of the DN gels under complex loading conditions. DN gels usually exhibit unique mechanical properties arising from the synergistic interaction between their two networks, including necking instability, shape memory effects, and self-healing capabilities. These multi-scale and multi-physics coupling characteristics pose significant challenges to traditional constitutive modeling, prompting researchers to develop refined finite element modeling methodologies.

To accurately capture these complex behaviors, user subroutines serve as a critical bridge connecting theoretical constitutive models with commercial software packages such as ABAQUS. Researchers have tailored these subroutines to address specific physical mechanisms. For instance, Zhao [2012] implemented a hyperelastic model via the UHYPER subroutine, integrating an interpenetrating network model with the network alteration theory to capture stress softening under large deformation. Similarly, Chen *et al.* [2021] employed the UMAT subroutine to simulate the shape memory effect of DN gels. Beyond user-defined subroutines, alternative modeling strategies have been adopted to address specific mechanical problems. Zhang *et al.* [2015] combined a cohesive zone model (CZM) describing intrinsic fracture energy with a modified Ogden–Roxburgh model describing bulk energy dissipation, achieving a refined description of the fracture process in DN gels. Furthermore, Xing *et al.* [2021] focused on dynamic properties, using modal analysis to study the resonance differences between components in DN gels.

Regarding element selection and meshing strategies, studies have optimized numerical schemes to address specific challenges. To mitigate volumetric locking in incompressible materials during large deformation, Liu *et al.* [2016] employed element formulations based on the F-bar technique. For axisymmetric compression or tension cases, Gao *et al.* [2024] and Zhao [2012] chose 2D axisymmetric elements or rectangular axisymmetric elements. To precisely capture microstructural responses in 3D space, Xing *et al.* [2021] used high-precision 20-node hexahedral elements, while Zhang *et al.* [2015] established planar models with fine mesh refinement to resolve high-gradient stress fields at crack tips.

Finite element simulations have played a decisive role in revealing the unique toughening, instability, and microscopic mechanisms of DN gels. Simulations by Zhao [2012] and Liu *et al.* [2016] intuitively reproduced the necking phenomenon, capturing the sudden drop in stress and the coexistence of thick and thin phases during necking propagation [Fig. 35]. Chen *et al.* [2021] effectively captured the stress drop induced by the formation of physical networks during cooling and enabled

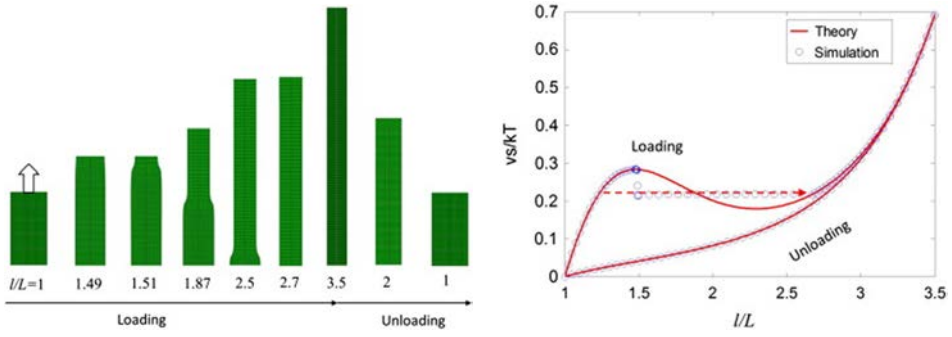

(a) (b)

Fig. 35. FEM simulations of DN gel deformation. The initiation and propagation of necking instability in a DN gel bar are shown, alongside the corresponding evolution of nominal stress with stretch [Zhao, 2012].

Source: Copyright 2011 Elsevier.

the simulation of shape-memory behaviors of DN gels under complex deformation modes, such as twisting and indentation. Simulations by Zhang *et al.* [2015] not only accurately predicted the total fracture energy but also visualized the crack tip process zone; the simulated strain fields matched highly with DIC experiments, revealing the synergistic toughening mechanism of intrinsic fracture energy and bulk energy dissipation. Furthermore, FEM is widely used to validate theoretical models by linking microscopic parameters to macroscopic performance. For instance, Xing *et al.* [2021] visualized the deflection distribution caused by resonance through cloud maps, clarifying the energy dissipation mechanism under mechanochemical coupling. Furthermore, Xing *et al.* [2023] validated the potential well model, quantitatively revealing how potential well depth (barrier energy) and width (mesh size) directly determine the material's yield and strengthening behavior, thereby confirming the model's validity in describing host-guest chemical interactions.

These works collectively demonstrate the core role of FEM in validating constitutive theories and bridging microscopic mechanisms with macroscopic performance of DN gels. However, further methodological developments are required to better characterize their nonlinear deformation and complex damage behaviors. For example, the phase field method represents a promising approach that can be embedded into commercial software to simulate the crack growth process. Additionally, coupling mechanical fields with external stimuli such as temperature and pH will further expand the scope of FEM in the design and optimization of future DN gels.

3.4. *Machine learning method*

With the rise of data-driven science, artificial intelligence (AI) has been extensively applied throughout the entire development process of hydrogels [Liao *et al.*, 2025;

Zhang *et al.*, 2025; Zheng and Liu, 2021; Zhu *et al.*, 2024a]. ML has evolved from a mere data analysis tool into a core driving force in the field of DN hydrogels. Based on current literature, the role of ML is primarily manifested in two dimensions: enabling material design and performance prediction and boosting application efficiency.

In the front-end material development stage, ML algorithms significantly accelerate the inverse design and high-throughput characterization of DN gels by handling high-dimensional experimental parameters. Addressing the complexity of multicomponent coupling, such as cross-linking density and interactions between the first and second networks, Xu *et al.* [2024] constructed a closed-loop optimization system using Bayesian optimization, the schematic workflow illustrating the Bayesian optimization process used to optimize the properties of DN gels is shown in Fig. 36. This study efficiently obtained an optimized recipe for PAAm/Alginate DN gels by balancing strain sensitivity, elongation, fracture energy, hysteresis, and resistivity, and utilized a random forest (RF) regression model to precisely predict mechanical properties under varying component concentrations. Additionally, to address efficiency bottlenecks in traditional rheological testing, Zhang *et al.* [2023a] introduced physics-guided ML strategies into micro-electromechanical sensing systems. By fusing raw sensor data of Alginate/ poly(N-isopropylacrylamide) (Alginate/PNIPAM) DN gels with fluid-structure interaction models, they achieved automated high-throughput classification of the sol-gel transition, increasing characterization efficiency by over 70 times.

In the back-end application phase, the robust signal decoupling and pattern recognition capabilities of ML, combined with the unique mechanical and functional properties of DN gels, have greatly boosted their potential in human-machine interaction, robotic tactile sensing, and biomedical diagnosis [Fig. 37]. Benefiting from the superior stretchability and fatigue resistance of the DN structure, conductive

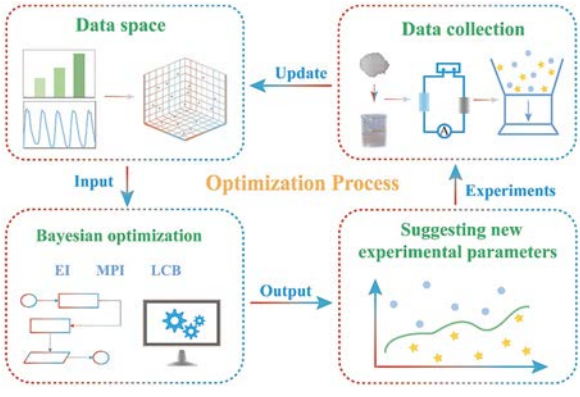

Fig. 36. Bayesian optimization framework for the data-driven design of DN gels [Xu *et al.*, 2024].

Source: Copyright 2024 under the terms of the Creative Commons CC BY license.

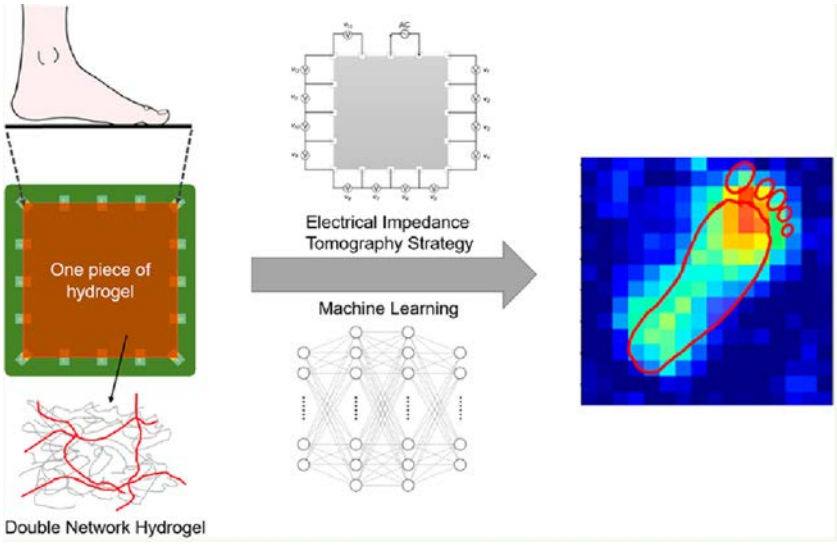

Fig. 37. ML-boosted application of DN gels. Schematic of a DN gel pressure sensor utilizing an EIT imaging strategy combined with ML [Liu *et al.*, 2021].

Source: Copyright 2021 American Chemical Society.

DN gels serve as robust wearable sensors [Ma *et al.*, 2023; Yang *et al.*, 2023; Zhou *et al.*, 2024a]. When coupled with deep learning models like convolutional neural network (CNN) [Yang *et al.*, 2023; Zhou *et al.*, 2024a], fully convolutional networks (FCN) [Ma *et al.*, 2023], or bidirectional long short-term memory (BiLSTM) networks [Zhou *et al.*, 2024a; Zhuo *et al.*, 2023] to process resistance signals under dynamic deformation, they achieve multiple human-machine interactions such as precise recognition of handwritten characters and Morse code. In fine tactile perception, DN ionogels utilize their rigid-flexible interpenetrating networks to achieve a hysteresis-free high-frequency response (520 Hz), enabling the CNN to accurately classify complex surface textures via friction signals [Qiu *et al.*, 2025]. Similarly, DN gels can also combine thermoelectric and piezoresistive mechanisms to assist multilayer perceptron (MLP) models in empowering robotic hands with object shape recognition capabilities [Tang *et al.*, 2025]. In the biomedical field, the high water retention and skin adaptability of DN structures ensure stable signal acquisition. DN gels can also provide low-impedance conformal contact, supporting RF algorithms in classifying blood pressure states based on high-fidelity ECG signals [Yang *et al.*, 2024]. Furthermore, surface-enhanced Raman spectroscopy (SERS) patches based on DN gels leverage their flexible matrix advantages, combined with Gaussian Naive Bayes (GNB) models, to realize non-invasive detection of sweat biomarkers [Zhu *et al.*, 2025]. For high-load scenarios, the high compressive strength of DN gel makes it suitable for plantar pressure monitoring. By combining the FCN algorithm to solve the inverse problem of electrical impedance tomography (EIT), high-precision

pressure distribution images of the plantar surface can be reconstructed [Liu *et al.*, 2021] [Fig. 37].

Despite the immense potential of ML in DN gel research, significant challenges remain. First and foremost, ML algorithms heavily depend on the dataset. If the input data are limited, it would be hard for the algorithm to make precise predictions [Xu *et al.*, 2024]. Currently, research data on hydrogels are often scattered with inconsistent formats, and the limited availability of high-quality public datasets makes it difficult to replicate results across different models. Therefore, establishing shared data platforms and standardizing data collection are essential. Second is the issue of interpretability; the black box nature of AI decision-making makes it difficult to elucidate the causal relationships between model predictions and the complex toughening mechanisms of DN gels (e.g., energy dissipation, network entanglement). Developing interpretable tools is urgent to reveal intrinsic structure-property relationships. Finally, multidisciplinary integration and data security are critical hurdles.

3.5. *Comparison of different computational methods*

In the field of DN gels, computational simulation has evolved from a mere supplementary tool for experimental validation into a core driver for revealing multiscale mechanical mechanisms, predicting macroscopic responses, and guiding inverse material design. Since the exceptional mechanical properties of DN gels arise from synergistic actions across vast spatiotemporal scales, from atomic hydrogen bond rupture and molecular chain conformational entropy to mesoscopic network damage and macroscopic necking deformation, no single computational method can simultaneously cover this entire spectrum. Consequently, existing computational research exhibits a distinct hierarchical structure, characterized by an inherent trade-off between physical resolution (accuracy) and simulation scale (efficiency). Table 2 summarizes the characteristics of these primary computational methods.

At the apex of the resolution hierarchy lies AAS. By employing high-precision force fields, AAS explicitly models the chemical structures and interactions of monomers, crosslinkers and water molecules, offering irreplaceable advantages in elucidating mechanisms dependent on specific chemical details. However, this extreme chemical precision comes at a high computational cost, restricting the field of view to the nanometer ($<$20 nm) and nanosecond scales. This limitation prevents AAS from directly simulating complex mechanical processes involving long-range chain entanglement, micron-scale phase separation, or macroscopic crack propagation, and periodic boundary conditions often obscure the material's large-scale heterogeneity.

To transcend the spatiotemporal constraints of AAS, CGS, and network simulations have adopted a strategy of reducing degrees of freedom, serving as a vital bridge connecting microscopic molecular structures to macroscopic mechanical performance. CGS typically maps atomic clusters into beads using bead-spring models, sacrificing some chemical specificity to access larger simulation scales. This

Table 2. Summary of computational methods for characterizing DN gels.

COMPUTATIONAL METHOD		TYPICAL SPATIOTEMPORAL SCALE	ADVANTAGES & MECHANISM ELUCIDATION	LIMITATIONS
MD METHOD	All-atom simulations (AAS)	Angstrom/nanosecond	High chemical precision: hydrogen bonding, electrostatics, solvent structures, thermodynamic origins (entropy/enthalpy)	Limited field of view to the nanometer and nanosecond scales, high computational cost
	Coarse-grained simulations (CGS)	Nanometer-micrometer/microsecond	Topology visualization: sacrificial bond fracture, void formation, network deformation mechanisms	Lacks specific chemical or physical details
	Multiscale simulations (MS)	Cross-scale (micro-meso)	Structural fidelity: connects synthesis kinetics to realistic topology and mechanical response	Challenging to couple different solvers/models, high computational cost
NETWORK SIMULATION METHOD		Mesoscopic statistical scale	Statistical damage mechanics: introduces chain length distribution and fracture probability to quantify defect effects on macroscopic mechanical behaviors	Lacks specific chemical or physical details
FEM		Millimeter-meter/Second-hour	Engineering simulation: handles complex geometries, multi-physics coupling, device-level responses (e.g., necking, shape memory)	Relies on preset constitutive models and input parameters, cannot spontaneously discover micro-mechanisms
ML METHOD		Arbitrary (Data-driven)	Inverse design & real-time inference: efficiently traverses parameter space for recipe optimization, processes nonlinear signals for HMI	Lacks physical interpretability, predictive capability is constrained by the scale and quality of training data

approach has successfully enabled the intuitive visualization of network topology evolution, the sequential fracture of sacrificial bonds, and void formation processes. Complementing this, network simulation approaches from a statistical mechanics perspective, introducing randomness in chain scission and distribution functions. This allows for the quantification of how structural homogeneity and stiffness ratios of two networks control the brittle-ductile transition. While these mesoscopic methods have greatly enriched the understanding of damage evolution mechanisms, their simplified treatment of solvent effects and the empirical parameterization of interaction energies limit their ability to quantitatively predict specific chemical or physical properties. To bridge this gap, MS have emerged as a powerful strategy, employing algorithms like RWRP to generate realistic network topologies that reflect experimental synthesis conditions such as chain entanglement. This approach allows for the direct investigation of how polymerization kinetics influence properties like anti-freezing mechanisms, though it remains computationally demanding and complex to implement due to the challenges of parameter passing between scales. In practical application, these MD methods serve as a critical tool for molecular engineering, enabling researchers to pre-screen functional monomers before actual synthesis.

When the research scale expands to millimeter or meter-scale engineering applications, the FEM based on continuum mechanics becomes the dominant tool. Unlike discrete particle models, FEM employs hyperelastic constitutive models and damage criteria to accurately handle complex geometric boundaries and multi-physics coupling. Beyond basic prediction, FEM serves as an important tool for device engineering and virtual prototyping. It allows engineers to simulate complex loading scenarios and optimize geometric structures virtually, thereby minimizing costly physical iterations. It remains the most effective method for predicting necking instability, shape memory effects, and large deformation behaviors of DN gels in soft robotics and sensor devices. However, the core limitation of FEM lies in its phenomenological nature: it cannot spontaneously "discover" unknown microscopic physical mechanisms. Its predictive accuracy is highly sensitive to input constitutive parameters (such as fracture energy and shear modulus), which must often be derived from experiments or lower-scale simulations.

In recent years, with the rise of data-driven science, ML has emerged as a new paradigm reshaping the design and application workflow of DN gels. Distinct from physics-based methods, ML establishes high-dimensional nonlinear mappings between composition, structure, and properties, enabling material inverse design and high-throughput screening that are difficult to achieve with traditional trial-and-error approaches. Crucially, the utility of ML extends into manufacturing and deployment. Algorithms are now employed to optimize synthesis parameters (e.g., curing time) for industrial scalability and to predict the service life of deployed components by integrating sensor data. Furthermore, ML acts as the "brain" for intelligent systems, capable of decoupling complex viscoelastic hysteresis signals

to achieve precise recognition of dynamic mechanical stimuli. Although ML currently faces challenges regarding "black box" interpretability and reliance on high-quality datasets, its integration with physical simulations represents an inevitable trend.

In summary, future computational research on DN gels will no longer be confined to single scales but will move towards a multi-scale integrated closed-loop workflow. For example, utilizing AAS to obtain fundamental physical parameters, inputting them into mesoscopic models to resolve topological mechanisms, extracting constitutive equations for macroscopic FEM simulations, and employing ML to accelerate iterative optimization. We believe this will significantly propel the precise design and engineering application of DN gels.

4. Current Challenges

Despite the remarkable progress in the experimental characterization and computational modeling of DN gels, several critical challenges remain. First, unlike the mature testing standards established for metals and rubbers (e.g., ASTM or ISO), there is a distinct lack of unified testing protocols specifically designed for soft and hydrated materials like DN gels. Variations in sample geometry, clamping methods, and loading rates across different research groups often lead to significant discrepancies in reported mechanical data, such as fracture toughness and fatigue thresholds. More critically, environmental factors, specifically humidity and hydration levels during testing, are frequently unreported, yet they drastically alter the mechanical response. This "data heterogeneity" creates a formidable barrier for data-driven research, as ML models trained on inconsistent datasets suffer from poor generalizability.

Besides, a persistent challenge in computational methods is the spatiotemporal gap between microscopic simulations and macroscopic reality. AAS provide chemical accuracy but are computationally limited to nanometers and nanoseconds, failing to capture macroscopic crack propagation or long-term fatigue behaviors. Conversely, FEM can simulate device-scale deformation but rely on phenomenological constitutive models that cannot spontaneously predict unknown micro-mechanisms. Although MS or network simulations aim to bridge this gap, they are currently computationally demanding and difficult to implement for complex, heterogeneous systems. Furthermore, the lack of quantitative agreement between simulation predictions and experimental outcomes remains a hurdle for identifying and predicting the mechanical behaviors of DN gels.

5. Conclusions and Outlook

This review has systematically summarized the state-of-the-art experimental and computational methods for studying the mechanical properties of DN gels. From the fundamental macroscopic testing to advanced non-contact techniques like DIC

and mechanochemistry, researchers now possess a versatile toolkit to probe the multiscale mechanisms of these materials. Parallelly, computational tools ranging from MD to ML have evolved from explanatory tools into predictive engines for material design. Looking forward, the convergence of these methodologies points toward transformative directions for the field.

To effectively navigate the vast design space of DN gels (e.g., varied monomer combinations, crosslinking ratios, and synthesis conditions) and deepen research, the field must establish consistent, high-quality material databases via standardized testing protocols. Coupling these databases with high-throughput experiments will not only accelerate the discovery of optimized formulations but also generate the robust datasets needed to train ML models. With such data foundations, ML will become a powerful tool for the inverse design optimal network architectures of DN gels, greatly reducing the development cycle.

Beyond material optimization, the impact of ML extends significantly into engineering practice. In manufacturing, ML algorithms can analyze synthesis parameters (e.g., curing time) to minimize variability and ensure the scalability and quality control essential for industrial production. For deployed systems, ML enables lifetime performance prediction. By integrating strain, stretch, and other parameters, ML models can predict the long-term degradation, fatigue life, and failure points of DN gels. Moreover, in applications such as soft robotics, ML can optimize dynamic operational parameters, such as actuation voltage, to achieve precise movements based on real-time feedback. Ultimately, ML offers a clear pathway to translate laboratory achievements into robust, commercially viable engineered systems.

While extensive research has focused on toughening DN gels, future work will likely shift toward developing multifunctional, intelligent systems. By leveraging insights from multiscale experiments and simulations, as well as data-driven design, DN gels will be engineered to possess life-like features such as autonomous self-healing, adaptive responsiveness to environmental stimuli (e.g., pH, temperature, electric fields), and shape-memory capabilities. These advanced hydrogels will form the material basis for the next generation of soft robotics, bio-integrated electronics, and artificial organs, blurring the boundary between synthetic materials and biological tissues. In turn, the emergence of these hydrogels will also facilitate in-depth research into their mechanical properties and the development of advanced experimental and computational methods, thereby driving the field forward.

Acknowledgments

This work was supported by the National Natural Science Foundation of China [Grant Nos: 12172273 and 11820101001]. The authors also acknowledge support from the Guangdong and Hong Kong Universities '1 + 1 + 1' Joint Research Collaboration Scheme. The authors would like to thank all the publishers mentioned for granting permission to reproduce the figures used in this work.

ORCID

Zidi Zhou https://orcid.org/0000-0001-8447-1851
Jiapeng You https://orcid.org/0009-0002-2569-7345
Jianxi Huang https://orcid.org/0009-0001-7445-4019
Zishun Liu https://orcid.org/0000-0003-4669-8347

References

Ahmed, S., Nakajima, T., Kurokawa, T., Haque, M. A. and Gong, J. P. [2014] "Brittle-ductile transition of double network hydrogels: Mechanical balance of two networks as the key factor," *Polymer* **55**(3), 914–923.

Ajam, A., Huang, Y. W., Islam, M. S., Kilian, K. A. and Kruzic, J. J. [2024] "Mechanical and biological behavior of double network hydrogels reinforced with alginate versus gellan gum," *Journal of the Mechanical Behavior of Biomedical Materials* **157**, 106642.

Arruda, E. M. and Boyce, M. C. [1993] "A three-dimensional constitutive model for the large stretch behavior of rubber elastic materials," *Journal of the Mechanics and Physics of Solids* **41**(2), 389–412.

Bai, R. B., Chen, B. H., Yang, J. W. and Suo, Z. G. [2019a] "Tearing a hydrogel of complex rheology," *Journal of the Mechanics and Physics of Solids* **125**, 749–761.

Bai, R. B., Yang, J. W. and Suo, Z. G. [2019b] "Fatigue of hydrogels," *European Journal of Mechanics A/Solids* **74**, 337–370.

Bai, R. B., Yang, Q. S., Tang, J. D., Morelle, X. P., Vlassak, J. and Suo, Z. G. [2017] "Fatigue fracture of tough hydrogels," *Extreme Mechanics Letters* **15**, 91–96.

Bonyadi, S. Z., Atten, M. and Dunn, A. C. [2019] "Self-regenerating compliance and lubrication of polyacrylamide hydrogels," *Soft Matter* **15**(43), 8728–8740.

Bonyadi, S. Z., Demott, C. J., Grunlan, M. A. and Dunn, A. C. [2021] "Cartilage-like tribological performance of charged double network hydrogels," *Journal of the Mechanical Behavior of Biomedical Materials* **114**, 104202.

Bonyadi, S. Z. and Dunn, A. C. [2020a] "Brittle or ductile? Abrasive wear of polyacrylamide hydrogels reveals load-dependent wear mechanisms," *Tribology Letters* **68**(1), 16.

Bonyadi, S. Z. and Dunn, A. C. [2020b] "Compositional dependence of polyacrylamide hydrogel abrasive wear resistance," *ACS Applied Polymer Materials* **2**(12), 5444–5451.

Brown, H. R. [2007] "A model of the fracture of double network gels," *Macromolecules* **40**(10), 3815–3818.

Chanda, A., Basu, D., Dasgupta, A., Chattopadhyay, S. and Mukhopadhyay, A. K. [1997] "A new parameter for measuring wear of materials," *Journal of Materials Science Letters* **16**(20), 1647–1651.

Chang, D. P., Dolbow, J. E. and Zauscher, S. [2007] "Switchable friction of stimulus-responsive hydrogels," *Langmuir* **23**(1), 250–257.

Chen, C., Wang, Z. J. and Suo, Z. G. [2017] "Flaw sensitivity of highly stretchable materials," *Extreme Mechanics Letters* **10**, 50–57.

Chen, Q., Chen, H., Zhu, L. and Zheng, J. [2015] "Fundamentals of double network hydrogels," *Journal of Materials Chemistry B* **3**(18), 3654–3676.

Chen, Y. F., Zhang, H. H., Chen, J. H., Kang, G. Z. and Hu, Y. H. [2021] "Hyperelastic model for polyacrylamide-gelatin double network shape-memory hydrogels," *Acta Mechanica Sinica* **37**(5), 748–756.

Costa, A. M. S. and Mano, J. F. [2015] "Extremely strong and tough hydrogels as prospective candidates for tissue repair — A review," *European Polymer Journal* **72**, 344–364.

Creton, C. and Ciccotti, M. [2016] "Fracture and adhesion of soft materials: A review," *Reports on Progress in Physics* **79**(4), 046601.

Davis, D. A. *et al.* [2009] "Force-induced activation of covalent bonds in mechanoresponsive polymeric materials," *Nature* **459**(7243), 68–72.

Ducrot, E., Chen, Y. L., Bulters, M., Sijbesma, R. P. and Creton, C. [2014] "Toughening elastomers with sacrificial bonds and watching them break," *Science* **344**(6180), 186–189.

Es-haghi, S. S., Leonov, A. I. and Weiss, R. A. [2014] "Deconstructing the double-network hydrogels: The importance of grafted chains for achieving toughness," *Macromolecules* **47**(14), 4769–4777.

Es-haghi, S. S., Mayfield, M. B. and Weiss, R. A. [2018] "Effect of freeze/thaw process on mechanical behavior of double-network hydrogels in finite tensile deformation," *Macromolecules* **51**(3), 1052–1057.

Es-haghi, S. S. and Weiss, R. A. [2016] "Fabrication of tough hydrogels from chemically cross-linked multiple neutral networks," *Macromolecules* **49**(23), 8980–8987.

Fang, Y. H., Liang, C., Liljeström, V., Lv, Z. P., Ikkala, O. and Zhang, H. [2024] "Toughening hydrogels with fibrillar connected double networks," *Advanced Materials* **36**(27), 2402282.

Frauenlob, M. *et al.* [2019] "Modulation and characterization of the double network hydrogel surface-bulk transition," *Macromolecules* **52**(17), 6704–6713.

Freedman, B. R. *et al.* [2024] "Instant tough adhesion of polymer networks," *Proceedings of the National Academy of Sciences* **121**(9), e2304643121.

Fukao, K., Nakajima, T., Nonoyama, T., Kurokawa, T., Kawai, T. and Gong, J. P. [2020] "Effect of relative strength of two networks on the internal fracture process of double network hydrogels as revealed by in situ small-angle X-ray scattering," *Macromolecules* **53**(4), 1154–1163.

Furukawa, H., Kuwabara, R., Tanaka, Y., Kurokawa, T., Na, Y. H., Osada, Y. and Gong, J. P. [2008] "Tear velocity dependence of high-strength double network gels in comparison with fast and slow relaxation modes observed by scanning microscopic light scattering," *Macromolecules* **41**(19), 7173–7178.

Gao, J. P., Luedtke, W. D., Gourdon, D., Ruths, M., Israelachvili, J. N. and Landman, U. [2004] "Frictional forces and Amontons' law: From the molecular to the macroscopic scale," *Journal of Physical Chemistry B* **108**(11), 3410–3425.

Gao, Y., Chen, J. J., Han, X. Y., Pan, Y. D., Wang, P. Y., Wang, T. J. and Lu, T. Q. [2020] "A universal strategy for tough adhesion of wet soft material," *Advanced Functional Materials* **30**(36), 2003207.

Gao, Y., La, H., Min, H. and Hou, Z. [2024] "Study on the mechanical properties of polyacrylic acid/chitosan double network hydrogels in dynamic water content," *Materials Research Express* **11**(11), 115308.

Ge, W., Cao, S., Yang, Y., Rojas, O. J. and Wang, X. [2021] "Nanocellulose/LiCl systems enable conductive and stretchable electrolyte hydrogels with tolerance to dehydration and extreme cold conditions," *Chemical Engineering Journal* **408**, 127306.

Gombert, Y., Simic, R., Roncoroni, F., Dubner, M., Geue, T. and Spencer, N. D. [2019] "Structuring hydrogel surfaces for tribology," *Advanced Materials Interfaces* **6**(22), 1901320.

Gong, B., Lin, J., Xie, Y. and Qian, J. [2025] "A combined numerical and theoretical study on the strengthening and toughening mechanisms of double network hydrogels," *International Journal of Smart and Nano Materials* **16**(2), 284–308.

Gong, J. P. [2010] "Why are double network hydrogels so tough?," *Soft Matter* **6**(12), 2583–2590.

Gong, J. P., Iwasaki, Y., Osada, Y., Kurihara, K. and Hamai, Y. [1999a] "Friction of gels. 3. Friction on solid surfaces," *Journal of Physical Chemistry B* **103**(29), 6001–6006.

Gong, J. P., Kagata, G. and Osada, Y. [1999b] "Friction of gels. 4. Friction on charged gels," *Journal of Physical Chemistry B* **103**(29), 6007–6014.

Gong, J. P., Katsuyama, Y., Kurokawa, T. and Osada, Y. [2003] "Double-network hydrogels with extremely high mechanical strength," *Advanced Materials* **15**(14), 1155–1158.

Gong, J. P., Kurokawa, T., Narita, T., Kagata, G., Osada, Y., Nishimura, G. and Kinjo, M. [2001] "Synthesis of hydrogels with extremely low surface friction," *Journal of the American Chemical Society* **123**(23), 5582–5583.

Gong, J. P. and Osada, Y. [2002] "Surface friction of polymer gels," *Progress in Polymer Science* **27**(1), 3–38.

Greensmith, H. W. [1963] "Rupture of rubber. X. The change in stored energy on making a small cut in a test piece held in simple extension," *Journal of Applied Polymer Science* **7**(3), 993–1002.

Guo, H. L. *et al.* [2019] "Internal damage evolution in double-network hydrogels studied by microelectrode technique," *Macromolecules* **52**(18), 7114–7122.

Hammouda, B. [2010] "SANS from polymers—Review of the recent literature," *Polymer Reviews* **50**(1), 14–39.

He, Y. F., Wan, X. D., Chen, Y. J. and Yang, C. H. [2021] "Enhance the debonding resistance of hydrogel by large-scale bridging," *Journal of the Mechanics and Physics of Solids* **155**.

Higuchi, Y., Saito, K., Sakai, T., Gong, J. P. and Kubo, M. [2018] "Fracture process of double-network gels by coarse-grained molecular dynamics simulation," *Macromolecules* **51**(8), 3075–3087.

Hsu, W. H., Kao, Y. C., Chuang, S. H., Wang, J. S., Lai, J. Y. and Tsai, H. C. [2019] "Thermosensitive double network of zwitterionic polymers for controlled mechanical strength of hydrogels," *RSC Advances* **9**(42), 24241–24247.

Huang, L., Jin, S., Bao, F., Tang, S., Yang, J., Peng, K. and Chen, Y. [2022] "Construction of a physically cross-linked carrageenan/chitosan/calcium ion double-network hydrogel for 3-Nitro-1, 2, 4-triazole-5-one removal," *Journal of Hazardous Materials* **424**, 127510.

Huang, M., Furukawa, H., Tanaka, Y., Nakajima, T., Osada, Y. and Gong, J. P. [2007] "Importance of entanglement between first and second components in high-strength double network gels," *Macromolecules* **40**(18), 6658–6664.

Huang, R., Zheng, S. J., Liu, Z. S. and Ng, T. Y. [2020] "Recent advances of the constitutive models of smart materials — Hydrogels and shape memory polymers," *International Journal of Applied Mechanics* **12**(2), 2050014.

Imaoka, C., Nakajima, T., Indei, T., Iwata, M., Hong, W., Marcellan, A. and Gong, J. P. [2023] "Inverse mechanical-swelling coupling of a highly deformed double-network gel," *Science Advances* **9**(19), eabp8351.

Itagaki, H., Kurokawa, T., Furukawa, H., Nakajima, T., Katsumoto, Y. and Gong, J. P. [2010] "Water-induced brittle-ductile transition of double network hydrogels," *Macromolecules* **43**(22), 9495–9500.

Jang, S. S., Goddard, W. A. and Kalani, M. Y. S. [2007] "Mechanical and transport properties of the poly(ethylene oxide)-poly(acrylic acid) double network hydrogel from molecular dynamic simulations," *Journal of Physical Chemistry B* **111**(7), 1729–1737.

Jaramillo-Botero, A., Blanco, M., Li, Y. Y., McGuinness, G. and Goddard, W. A. [2010] "First-principles based approaches to nano-mechanical and biomimetic characterization of polymer-based hydrogel networks for cartilage scaffold-supported therapies," *Journal of Computational and Theoretical Nanoscience* **7**(7), 1238–1256.

Jia, Y. T., Zhou, Z. D., Jiang, H. L. and Liu, Z. S. [2022] "Characterization of fracture toughness and damage zone of double network hydrogels," *Journal of the Mechanics and Physics of Solids* **169**, 105090.

Jia, Y. T., Zhou, Z. D. and Liu, Z. S. [2023] "Double network hydrogels: A measurement method of fracture toughness based on trouser tear test," IAAM-SC, S0003-2023 (IAAM Standard) Singapore.

Jia, Z. X. *et al.* [2025] "Flexible fluorescent sensor based on a heterojunction-functionalized hydrogel with dual-mode crosslinking for H2S monitoring during fish spoilage," *Chemical Engineering Journal* **522**, 168158.

Jian, N. N., Wang, J. L., Zuo, L. and Zhang, K. [2023] "An in situ inhibition strategy: Forming a physical barrier around ionic crosslinkers to toughen double-network hydrogels," *Materials & Design* **225**, 111522.

Jiang, X. C., Chen, Q. Q., Yang, M., Chen, X., Lu, T. Q. and Wang, T. J. [2024] "Achieving ultrastrong adhesion of soft materials by discretized stress dispersion," *Journal of the Mechanics and Physics of Solids* **192**, 105800.

Johnson, J. A., Turro, N. J., Koberstein, J. T. and Mark, J. E. [2010] "Some hydrogels having novel molecular structures," *Progress in Polymer Science* **35**(3), 332–337.

Joseph, D., Brise, R. M., Li, D. P. and Chalivendra, V. [2025] "Interfacial fracture of hydrogen-bonded double network hydrogels," *Polymer Engineering and Science* **65**(10), 5248–5265.

Kagata, G., Gong, J. P. and Osada, Y. [2002] "Friction of gels. 6. Effects of sliding velocity and viscoelastic responses of the network," *Journal of Physical Chemistry B* **106**(18), 4596–4601.

Kaneko, D., Tada, T., Kurokawa, T., Gong, J. P. and Osada, Y. [2005] "Mechanically strong hydrogels with ultra-low frictional coefficients," *Advanced Materials* **17**(5), 535–538.

Khalesi, H., Lu, W., Nishinari, K. and Fang, Y. P. [2020] "New insights into food hydrogels with reinforced mechanical properties: A review on innovative strategies," *Advances in Colloid and Interface Science* **285**, 102278.

Kim, J., Zhang, G. G., Shi, M. X. and Suo, Z. G. [2021] "Fracture, fatigue and friction of polymers in which entanglements greatly outnumber cross-links," *Science* **374**(6564), 212–216.

King, D. R., Okumura, T., Takahashi, R., Kurokawa, T. and Gong, J. P. [2019] "Macroscale double networks: Design criteria for optimizing strength and toughness," *ACS Applied Materials & Interfaces* **11**(38), 35343–35353.

King, D. R., Takahashi, R., Ikai, T., Fukao, K., Kurokawa, T. and Gong, J. P. [2020] "Anisotropic double-network hydrogels via controlled orientation of a physical sacrificial network," *ACS Applied Polymer Materials* **2**(6), 2350–2358.

Kolvin, I., Kolinski, J. M., Gong, J. P. and Fineberg, J. [2018] "How supertough gels break," *Physical Review Letters* **121**(13), 135501.

Kopnar, V., O'Connell, A., Shirshova, N. and Aufderhorst-Roberts, A. [2025] "Mechanistic origins of yielding in hybrid double-network hydrogels," *Macromolecules* **58**(16), 8610–8621.

Kurokawa, T., Furukawa, H., Wang, W., Tanaka, Y. and Gong, J. P. [2010] "Formation of a strong hydrogel-porous solid interface via the double-network principle," *Acta Biomaterialia* **6**(4), 1353–1359.

Lake, G. J. and Thomas, A. G. [1967] "The strength of highly elastic materials," *Proceedings of the Royal Society of London. A. Mathematical and Physical Sciences* **300**(1460), 108–119.

Lee, M. J. and Espinosa-Marzal, R. M. [2023] "Intrinsic and extrinsic tunability of double-network hydrogel strength and lubricity," *ACS Applied Materials & Interfaces* **15**(16), 20495–20507.

Lei, J. C., Li, Z. Q., Xu, S. and Liu, Z. S. [2021a] "A mesoscopic network mechanics method to reproduce the large deformation and fracture process of cross-linked elastomers," *Journal of the Mechanics and Physics of Solids* **156**, 104599.

Lei, J. C., Li, Z. Q., Xu, S. and Liu, Z. S. [2021b] "Recent advances of hydrogel network models for studies on mechanical behaviors," *Acta Mechanica Sinica* **37**(3), 367–386.

Lei, J. C. and Liu, Z. S. [2024] "A chain scission-induced anisotropic damage constitutive model for double network hydrogels," *International Journal of Applied Mechanics* **16**(06), 2450076.

Li, H., Lei, J. C., Wang, D. Y. and Liu, Z. S. [2024a] "The fracture and toughening mechanism of double-network hydrogel using the network mechanics method," *Engineering Fracture Mechanics* **309**, 110413.

Li, H. X., Wu, H. Y., Li, B., Gao, Y. Y., Zhao, X. Y. and Zhang, L. Q. [2020] "Molecular dynamics simulation of fracture mechanism in the double interpenetrated cross-linked polymer," *Polymer* **199**, 122571.

Li, J. *et al.* [2017] "Tough adhesives for diverse wet surfaces," *Science* **357**(6349), 378–381.

Li, J. Y., Illeperuma, W. B. K., Suo, Z. G. and Vlassak, J. J. [2014] "Hybrid hydrogels with extremely high stiffness and toughness," *ACS Macro Letters* **3**(6), 520–523.

Li, L. F., Lei, H. and Cao, Y. [2024b] "Fatigue-resistant hydrogels," *Chemical Research in Chinese Universities* **40**(1), 64–77.

Li, Q., Wang, L., Liu, Q., Hong, W. and Yang, C. [2021] "Fatigue damage–resistant physical hydrogel adhesion," *Frontiers in Robotics and AI* **8**, 666343.

Li, X., Wu, C., Yang, Q., Long, S. and Wu, C. [2015] "Low-velocity super-lubrication of sodium-alginate/polyacrylamide ionic–covalent hybrid double-network hydrogels," *Soft Matter* **11**(15), 3022–3033.

Li, Y. H., Liu, J. J., Zhang, Q. F., Hu, N., Jiang, Z. H., Kan, Q. H. and Kang, G. Z. [2024c] "Growth of double-network tough hydrogel coatings by surface-initiated polymerization," *ACS Applied Materials & Interfaces* **16**(8), 10822–10831.

Liang, S. M., Flu, J., Wu, Z. L., Kurokawa, T. and Gong, J. P. [2012] "Toughness enhancement and stick-slip tearing of double-network hydrogels in poly(ethylene glycol) solution," *Macromolecules* **45**(11), 4758–4763.

Liao, H. G. *et al.* [2025] "Data-driven de novo design of super-adhesive hydrogels," *Nature* **644**(8075), 89–95.

Lin, W. C., Fan, W., Marcellan, A., Hourdet, D. and Creton, C. [2010] "Large strain and fracture properties of poly(dimethylacrylamide)/silica hybrid hydrogels," *Macromolecules* **43**(5), 2554–2563.

Liu, J., Lin, S. T., Liu, X. Y., Qin, Z., Yang, Y. Y., Zang, J. F. and Zhao, X. H. [2020] "Fatigue-resistant adhesion of hydrogels," *Nature Communications* **11**(1), 1071.

Liu, J. J., Yang, C. H., Yin, T. H., Wang, Z. J., Qu, S. X. and Suo, Z. G. [2019a] "Polyacrylamide hydrogels. II. elastic dissipater," *Journal of the Mechanics and Physics of Solids* **133**, 103737.

Liu, J. X., Du, Y. H., Zhou, Y. F., Wu, H. and Lu, T. Q. [2024] "High-throughput experimental method for measuring fatigue crack growth rate curve of soft materials," *International Journal of Fatigue* **184**, 108320.

Liu, J. Y. *et al.* [2017] "Triggerable tough hydrogels for gastric resident dosage forms," *Nature Communications* **8**, 124.

Liu, R. X., Li, Y. X. and Liu, Z. S. [2019b] "Experimental study of thermo-mechanical behavior of a thermosetting shape-memory polymer," *Mechanics of Time-Dependent Materials* **23**(3), 249–266.

Liu, Y., Zhang, H. W. and Zheng, Y. G. [2016] "A micromechanically based constitutive model for the inelastic and swelling behaviors in double network hydrogels," *Journal of Applied Mechanics-Transactions of the ASME* **83**(2), 021008.

Liu, Y. L., Zhang, D., Tang, Y. J., Gong, X. and Zheng, J. [2023] "Development of a radical polymerization algorithm for molecular dynamics simulations of antifreezing hydrogels with double-network structures," *npj Computational Materials* **9**(1), 209.

Liu, Z. S. [2024] *Fundamentals of Continuum Mechanics* (World Scientific, Singapore).

Liu, Z. S., Swaddiwudhipong, S., Cui, F. S., Hong, W., Suo, Z. and Zhang, Y. W. [2011] "Analytical solutions of polymeric gel structures under buckling and wrinkle," *International Journal of Applied Mechanics* **3**(2), 235–257.

Liu, Z. S., Toh, W. and Ng, T. Y. [2015] "Advances in mechanics of soft materials: A review of large deformation behavior of hydrogels," *International Journal of Applied Mechanics* **7**(5), 1530001.

Liu, Z. X. *et al.* [2021] "Hydrogel pressure distribution sensors based on an imaging strategy and machine learning," *ACS Applied Electronic Materials* **3**(8), 3599–3609.

Long, R. and Hui, C. Y. [2016] "Fracture toughness of hydrogels: Measurement and interpretation," *Soft Matter* **12**(39), 8069–8086.

Long, R., Hui, C. Y., Gong, J. P. and Bouchbinder, E. [2021] "The fracture of highly deformable soft materials: A tale of two length scales," *Annual Review of Condensed Matter Physics* **12**,71–94.

Lu, F. X., Nakajima, T., Zheng, Y., Fan, H. L. and Gong, J. P. [2024] "Tensile behaviors of double network hydrogels with varied first network topological and chemical structures," *Macromolecules* **57**(24), 11520–11533.

Lu, W. J., Wang, C., Zhou, Z. D., Xu, S. and Liu, Z. S. [2025] "Quantify the failure zone and elastic release zone: A new insight into intrinsic fracture of polymer networks," *Extreme Mechanics Letters* **78**, 102362.

Ma, J. *et al.* [2024] "Designing ultratough single-network hydrogels with centimeter-scale fractocohesive lengths via inelastic crack blunting," *Advanced Materials* **36**(23), 2311795.

Ma, Y. H. *et al.* [2023] "Self-adhesive, anti-freezing MXene-based hydrogel strain sensor for motion monitoring and handwriting recognition with deep learning," *ACS Applied Materials & Interfaces* **15**(24), 29413–29424.

Ma, Z. W. *et al.* [2022] "Controlled tough bioadhesion mediated by ultrasound," *Science* **377**(6607), 751–755.

Mao, Y. W., Lin, S. T., Zhao, X. H. and Anand, L. [2017] "A large deformation viscoelastic model for double-network hydrogels," *Journal of the Mechanics and Physics of Solids* **100**, 103–130.

Matsuda, T., Kashimura, N., Sakai, T., Nakajima, T., Matsushita, T. and Gong, J. P. [2025] "Yielding of double-network hydrogels with systematically controlled tetra-PEG first networks," *Macromolecules* **58**(12), 6017–6032.

Matsuda, T., Kawakami, R., Nakajima, T. and Gong, J. P. [2020] "Crack tip field of a double-network gel: Visualization of covalent bond scission through mechanoradical polymerization," *Macromolecules* **53**(20), 8787–8795.

Matsuda, T., Kawakami, R., Nakajima, T., Hane, Y. and Gong, J. P. [2021] "Revisiting the origins of the fracture energy of tough double-network hydrogels with quantitative mechanochemical characterization of the damage zone," *Macromolecules* **54**(22), 10331–10339.

Matsuda, T., Kawakami, R., Namba, R., Nakajima, T. and Gong, J. P. [2019] "Mechanoresponsive self-growing hydrogels inspired by muscle training," *Science* **363**(6426), 504–508.

Matsuda, T. *et al.* [2016] "Yielding criteria of double network hydrogels," *Macromolecules* **49**(5), 1865–1872.

Meinert, C. *et al.* [2025] "Crosslinking substrate regulates frictional properties of tissue-engineered cartilage and chondrocyte response to loading," *Communications Materials* **6**(1), 55.

Mezger, T. [2020] *The Rheology Handbook* (Vincentz Network, Hannover, Germany)

Milner, P. E., Parkes, M., Puetzer, J. L., Chapman, R., Stevens, M. M., Cann, P. and Jeffers, J. R. T. [2018] "A low friction, biphasic and boundary lubricating hydrogel for cartilage replacement," *Acta Biomaterialia* **65**, 102–111.

Mooney, M. [1940] "A theory of large elastic deformation," *Journal of Applied Physics* **11**(9), 582–592.

Morovati, V. and Dargazany, R. [2019] "Micro-mechanical modeling of the stress softening in double-network hydrogels," *International Journal of Solids and Structures* **164**, 1–11.

Morovati, V., Saadat, M. A. and Dargazany, R. [2020] "Necking of double-network gels: Constitutive modeling with microstructural insight," *Physical Review E* **102**(6), 062501.

Murosaki, T. *et al.* [2009] "Antifouling properties of tough gels against barnacles in a long-term marine environment experiment," *Biofouling* **25**(7), 657–666.

Na, Y. H. *et al.* [2004] "Structural characteristics of double network gels with extremely high mechanical strength," *Macromolecules* **37**(14), 5370–5374.

Na, Y. H., Tanaka, Y., Kawauchi, Y., Furukawa, H., Sumiyoshi, T., Gong, J. P. and Osada, Y. [2006] "Necking phenomenon of double-network gels," *Macromolecules* **39**(14), 4641–4645.

Nakajima, T. [2017] "Generalization of the sacrificial bond principle for gel and elastomer toughening," *Polymer Journal* **49**(6), 477–485.

Nakajima, T., Fukuda, Y., Kurokawa, T., Sakai, T., Chung, U. and Gong, J. P. [2013] "Synthesis and fracture process analysis of double network hydrogels with a well-defined first network," *ACS Macro Letters* **2**(6), 518–521.

Nakajima, T., Furukawa, H., Tanaka, Y., Kurokawa, T., Osada, Y. and Gong, J. P. [2009] "True chemical structure of double network hydrogels," *Macromolecules* **42**(6), 2184–2189.

Nakajima, T., Kurokawa, T., Furukawa, H. and Gong, J. P. [2020] "Effect of the constituent networks of double-network gels on their mechanical properties and energy dissipation process," *Soft Matter* **16**(37), 8618–8627.

Nakajima, T., Sato, H., Zhao, Y., Kawahara, S., Kurokawa, T., Sugahara, K. and Gong, J. P. [2012] "A universal molecular stent method to toughen any hydrogels based on double network concept," *Advanced Functional Materials* **22**(21), 4426–4432.

Nishimura, T., Guo, H. L., Katsuyama, Y., Yoshida, M., Gong, J. P. and Kurokawa, T. [2024] "Spatial analysis of the damage zone in double network hydrogel using the microelectrode technique," *Macromolecules* **57**(4), 1502–1508.

Nonoyama, T. and Gong, J. P. [2021] "Tough double network hydrogel and its biomedical applications," *Annual Review of Chemical and Biomolecular Engineering,***12**, 393–410.

Parada, G. A., Yuk, H., Liu, X. Y., Hsieh, A. J. and Zhao, X. H. [2017] "Impermeable robust hydrogels via hybrid lamination," *Advanced Healthcare Materials* **6**(19), 1700520.

Patel, M., Leggett, S. E., Landauer, A. K., Wong, I. Y. and Franck, C. [2018] "Rapid, topology-based particle tracking for high-resolution measurements of large complex 3D motion fields," *Scientific Reports* **8**, 5581.

Qi, Y. *et al.* [2024] "Mapping deformation and dissipation during fracture of soft viscoelastic solid," *Journal of the Mechanics and Physics of Solids* **186**, 105595.

Qiu, J. M., Song, Y. Y., Li, J., Lu, C. H., Wu, X. D. and Xiong, R. [2025] "Chiral photonic ionic skin for ultrafast, hysteresis-free mechanosensing," *ACS Nano* **19**(46), 39827–39838.

Rao, P. *et al.* [2018] "Tough hydrogels with fast, strong, and reversible underwater adhesion based on a multiscale design," *Advanced Materials* **30**(32), 1801884.

Ren, X. R. *et al.* [2024] "Enzyme-immobilized surface-catalyzed cross-linking: Creating multifunctional double network hydrogel coatings on diverse substrates," *Advanced Functional Materials* **34**(27), 2312465.

Rivlin, R. S. and Thomas, A. G. [1953] "Rupture of rubber. I. Characteristic energy for tearing," *Journal of Polymer Science* **10**(3), 291–318.

Rose, S., Prevoteau, A., Elzière, P., Hourdet, D., Marcellan, A. and Leibler, L. [2014] "Nanoparticle solutions as adhesives for gels and biological tissues," *Nature* **505**(7483), 382–385.

Ruan, J.-A. and Bhushan, B. [1994] "Atomic-scale friction measurements using friction force microscopy: Part I—General principles and new measurement techniques," *Journal of Tribology* **116**(2), 378–388.

Saito, J. *et al.* [2011] "Robust bonding and one-step facile synthesis of tough hydrogels with desirable shape by virtue of the double network structure," *Polymer Chemistry* **2**(3), 575–580.

Sakurai, S., Kurokawa, T., Furukawa, H., Gong, J. P. and Nakajima, T. [2025] "Double-network hydrogels with a gradient hydrophobic coating that prevents water evaporation and allows strong adhesion to a solid substrate," *Polymer Journal* **57**(4), 441–447.

Selvamuthu, M. G. *et al.* [2023] "Development of soft inchworm robot with friction control of feet using double-network gel," *Advanced Robotics* **37**(6), 407–422.

Shestakova, P., Willem, R. and Vassileva, E. [2011] "Elucidation of the chemical and morphological structure of double-network (DN) hydrogels by high-resolution magic angle spinning (HRMAS) NMR spectroscopy," *Chemistry-A European Journal* **17**(52), 14867–14877.

Shoaib, T. and Espinosa-Marzal, R. M. [2018] "Insight into the viscous and adhesive contributions to hydrogel friction," *Tribology Letters* **66**(3), 96.

Shoaib, T. and Espinosa-Marzal, R. M. [2019] "Influence of loading conditions and temperature on static friction and contact aging of hydrogels with modulated microstructures," *ACS Applied Materials & Interfaces* **11**(45), 42722–42733.

Shoaib, T., Prendergast, P. and Espinosa-Marzal, R. M. [2022] "Compositional tuning reveals a pathway to achieve a strong and lubricious double network in agarose-polyacrylamide hydrogels," *Tribology Letters* **70**(3), 71.

Simic, R., Yetkin, M., Zhang, K. H. and Spencer, N. D. [2020] "Importance of hydration and surface structure for friction of acrylamide hydrogels," *Tribology Letters* **68**(2), 64.

Song, R. J. *et al.* [2024] "Enhanced strength for double network hydrogel adhesive through cohesion-adhesion balance," *Advanced Functional Materials* **34**(23), 2313322.

Stratigaki, M., Baumann, C., van Breemen, L. C. A., Heuts, J. P. A., Sijbesma, R. P. and Göstl, R. [2020] "Fractography of poly(N-isopropylacrylamide) hydrogel networks crosslinked with mechanofluorophores using confocal laser scanning microscopy," *Polymer Chemistry* **11**(2), 358–366.

Sun, D. Q., Zhou, Y. F., Guo, H. Y., Yang, M., Lu, T. Q. and Wang, T. J. [2024] "Flaw sensitivity of bacterial cellulose hydrogel under monotonic and cyclic loadings," *Engineering Fracture Mechanics* **303**, 110134.

Sun, J. Y. *et al.* [2012] "Highly stretchable and tough hydrogels," *Nature* **489**(7414), 133–136.

Tada, H., Paris, P. C. and Irwin, G. R. [2000] *The Stress Analysis of Cracks Handbook*, 3rd edn. (ASME Press, USA).

Takagi, M., Yoshida, K., Hoshino, H., Tadakuma, R., Suzuri, Y. and Furukawa, H. [2019] "Sliding walk with friction control of double-network gel on feet of inchworm robot," *Frontiers in Mechanical Engineering* **5**, 44.

Takahashi, R. *et al.* [2018] "Tough particle-based double network hydrogels for functional solid surface coatings," *Advanced Materials Interfaces* **5**(23), 1801018.

Tanaka, Y. [2007] "A local damage model for anomalous high toughness of double-network gels," *Europhysics Letters*, **78**(5), 56005.

Tanaka, Y., Kawauchi, Y., Kurokawa, T., Furukawa, H., Okajima, T. and Gong, J. P. [2008] "Localized yielding around crack tips of double-network gelsa," *Macromolecular Rapid Communications* **29**(18), 1514–1520.

Tang, J. D., Li, J. Y., Vlassak, J. J. and Suo, Z. G. [2016] "Adhesion between highly stretchable materials," *Soft Matter* **12**(4), 1093–1099.

Tang, J. D., Li, J. Y., Vlassak, J. J. and Suo, Z. G. [2017] "Fatigue fracture of hydrogels," *Extreme Mechanics Letters* **10**, 24–31.

Tang, X. Z. *et al.* [2025] "Development of a two-mode hydrogel sensor with a thermal diffusion effect for intelligent sensing and temperature warning," *Materials Today Physics* **55**, 101750.

Tauber, J., Rovigatti, L., Dussi, S. and van der Gucht, J. [2021] "Sharing the load: Stress redistribution governs fracture of polymer double networks," *Macromolecules* **54**(18), 8563–8574.

Teng, Y. T. *et al.* [2025] "Hydrogel toughening resets biomedical application boundaries," *Progress in Polymer Science* **161**, 101929.

Tirumala, V. R., Tominaga, T., Lee, S., Butler, P. D., Lin, E. K., Gong, J. P. and Wu, W. L. [2008] "Molecular model for toughening in double-network hydrogels," *Journal of Physical Chemistry B* **112**(27), 8024–8031.

Tominaga, T., Sano, K. I., Kikuchi, J., Mitomo, H., Ijiro, K. and Osada, Y. [2012] "Hydrophilic double-network polymers that sustain high mechanical modulus under 80% humidity," *ACS Macro Letters* **1**(3), 432–434.

Tominaga, T., Takata, S.-i., Suzuki, J.-i., Aizawa, K., Seto, H. and Arai, M. [2014] "Adsorption of water to double-network polymers having a hierarchical structure," *Journal of Physics: Conference Series* **502**(1), 012058.

Tominaga, T., Tirumala, V. R., Lee, S., Lin, E. K., Gong, J. P. and Wu, W. L. [2008] "Thermodynamic interactions in double-network hydrogels," *Journal of Physical Chemistry B* **112**(13), 3903–3909.

Tominaga, T., Tirumala, V. R., Lin, E. K., Gong, J. P., Furukawa, H., Osada, Y. and Wu, W. L. [2007] "The molecular origin of enhanced toughness in double-network hydrogels: A neutron scattering study," *Polymer* **48**(26), 7449–7454.

Tsukeshiba, H. *et al.* [2005] "Effect of polymer entanglement on the toughening of double network hydrogels," *Journal of Physical Chemistry B* **109**(34), 16304–16309.

Wada, M. *et al.* [2018] "Electric control of friction on surface of high-strength hydrogels," *Microsystem Technologies* **24**(1), 639–646.

Walker, S. B. and Fielding, S. M. [2025] "Toughness of double network hydrogels: The role of reduced stress propagation," *Physical Review Letters* **135**(18), 188201.

Wan, H. X., Shen, J. X., Gao, N. S., Liu, J., Gao, Y. Y. and Zhang, L. Q. [2018] "Tailoring the mechanical properties by molecular integration of flexible and stiff polymer networks," *Soft Matter* **14**(12), 2379–2390.

Wang, C., Jia, Y. T., You, J. P., Lei, J. C. and Liu, Z. S. [2025a] "A damage model of characterizing the internal damage evolution for DN hydrogel using multi-particle tracking (MPT) method," *Mechanics of Materials* **206**, 105360.

Wang, F., Yu, X., Cao, Z. X., Liu, Y., Jiang, X. B. and Gu, X. L. [2024a] "Synergic enhancement of hydrogel upon multi-level hydrogen bonds via macromolecular design for dual-mode electronic skin," *Chemical Engineering Journal* **489**, 151249.

Wang, L. *et al.* [2023a] "Injectable double-network hydrogel for corneal repair," *Chemical Engineering Journal* **455**, 140698.

Wang, L. J., Yang, K. X., Zhou, Q., Yang, H. Y., He, J. Q. and Zhang, X. Y. [2020] "Rhodamine mechanophore functionalized mechanochromic double network hydrogels with high sensitivity to stress," *Chinese Journal of Polymer Science* **38**(1), 24–36.

Wang, S.-C. *et al.* [2023b] "Understanding gel-powers: Exploring rheological marvels of acrylamide/sodium alginate double-network hydrogels," *Molecules* **28**(12), 4868.

Wang, S. T., Euchler, E., Schneider, K. and Wiessner, S. [2025b] "Characterization of the deformation and fracture of tough double-network hydrogels," *Polymer* **340**, 129190.

Wang, S. Y., Li, J. R., Pan, Y. D., Liu, F. K., Zeng, L. S., Gao, Y. and Lu, T. Q. [2022] "A double-network strategy for the tough tissue adhesion of hydrogels with long-term stability under physiological environment," *Soft Matter* **18**(33), 6192–6199.

Wang, X. D., Lu, H. B., Wu, N., Hui, D. and Fu, Y. Q. [2019] "Unraveling bio-inspired pre-swollen effects of tetra-polyethylene glycol double network hydrogels with ultra-stretchable yielding strain," *Smart Materials and Structures* **28**(3), 035005.

Wang, Z. J., Li, W., Li, X. Y., Nakajima, T., Rubinstein, M. and Gong, J. P. [2025c] "Rapid self-strengthening in double-network hydrogels triggered by bond scission," *Nature Materials* **24**(4), 607–614.

Wang, Z. J. *et al.* [2024b] "Effect of the activation force of mechanophore on its activation selectivity and efficiency in polymer networks," *Journal of the American Chemical Society* **146**(19), 13336–13346.

Wang, Z. J., Wei, G. M., Nakajima, T. and Gong, J. P. [2025d] "Effect of the second network on first network rupture and the origin of energy dissipation in double network hydrogels," *Macromolecules* **58**(9), 4835–4846.

Webber, R. E., Creton, C., Brown, H. R. and Gong, J. P. [2007] "Large strain hysteresis and mullins effect of tough double-network hydrogels," *Macromolecules* **40**(8), 2919–2927.

Wichterle, O. and Lím, D. [1960] "Hydrophilic gels for biological use," *Nature* **185**(4706), 117–118.

Wu, Y., Liu, Y., Yang, X., Tong, M., Jiang, X. and Gu, X. [2024] "Triple-responsive, multimodal, visual electronic skin toward all-in-one health management for gestational diabetes mellitus," *ACS Sensors* **9**(5), 2634–2644.

Xiao, Y. H., Friis, E. A., Gehrke, S. H. and Detamore, M. S. [2013] "Mechanical testing of hydrogels in cartilage tissue engineering: Beyond the compressive modulus," *Tissue Engineering Part B-Reviews* **19**(5), 403–412.

Xin, H., Saricilar, S. Z., Brown, H. R., Whitten, P. G. and Spinks, G. M. [2013] "Effect of first network topology on the toughness of double network hydrogels," *Macromolecules* **46**(16), 6613–6620.

Xing, Z. Y., Li, P. Z., Lu, H. B. and Fu, Y. Q. [2021] "Mechanoresponsive resonance differences in double-network hydrogels towards multipartite dynamics," *Journal of Physics D-Applied Physics* **54**(46), 465301.

Xing, Z. Y., Lu, H. B., Lau, D. and Fu, Y. Q. [2023] "A potential well model for host-guest chemistry in double-network hydrogels toward mechanochemical coupling and toughening," *Journal of Physics D-Applied Physics* **56**(6), 065302.

Xu, P., Shang, Z. J., Yao, M. L., Ke, Z. Y., Li, X. X. and Liu, P. D. [2022] "Molecular insights on the mechanical properties of double-network hydrogels reinforced by covalently compositing with silica-nanoparticles," *Journal of Molecular Liquids* **368**, 120611.

Xu, S., Chen, X., Wang, S., Chen, Z., Pan, P. and Huang, Q. [2024] "Integrating machine learning for the optimization of polyacrylamide/alginate hydrogel," *Regenerative Biomaterials* **11**, rbae109.

Xu, X. W., Jerca, V. V. and Hoogenboom, R. [2021] "Bioinspired double network hydrogels: From covalent double network hydrogels via hybrid double network hydrogels to physical double network hydrogels," *Materials Horizons* **8**(4), 1173–1188.

Yang, C. C. *et al.* [2024] "Polymer hydrogel electronics with adhesive, self-healing and anti-ultraviolet capabilities for machine learning-promoted electrophysiological detection," *Chemical Engineering Journal* **498**, 155766.

Yang, C. H., Yin, T. H. and Suo, Z. G. [2019] "Polyacrylamide hydrogels. I. Network imperfection," *Journal of the Mechanics and Physics of Solids* **131**, 43–55.

Yang, J. *et al.* [2022] "Recent progress in double network elastomers: One plus one is greater than two," *Advanced Functional Materials* **32**(19), 2110244.

Yang, J., Li, Y., Zhu, L., Qin, G. and Chen, Q. [2018a] "Double network hydrogels with controlled shape deformation: A mini review," *Journal of Polymer Science Part B-Polymer Physics* **56**(19), 1351–1362.

Yang, J. S. *et al.* [2023] "Tough, multifunctional, and green double-network binary solvent eutectogel with in-situ generation of lignin nanoparticles based on one-step dual phase separations for wearable flexible strain sensors," *Chemical Engineering Journal* **474**, 145544.

Yang, J. W., Bai, R. B., Chen, B. H. and Suo, Z. G. [2020] "Hydrogel adhesion: A supramolecular synergy of chemistry, topology, and mechanics," *Advanced Functional Materials* **30**(2), 1901693.

Yang, J. W., Bai, R. B. and Suo, Z. G. [2018b] "Topological adhesion of wet materials," *Advanced Materials* **30**(25), 1800671.

Yasuda, K. *et al.* [2005] "Biomechanical properties of high-toughness double network hydrogels," *Biomaterials* **26**(21), 4468–4475.

Yasuda, K. *et al.* [2009] "A novel double-network hydrogel induces spontaneous articular cartilage regeneration in vivo in a large osteochondral defect," *Macromolecular Bioscience* **9**(4), 307–316.

Yin, Y., Gu, Q. Z., Liu, X. B., Liu, F. G. and McClements, D. J. [2023] "Double network hydrogels: Design, fabrication, and application in biomedicines and foods," *Advances in Colloid and Interface Science* **320**, 102999.

Yoshida, M., Kiyama, R., Zhang, Y., King, D. R., Kurokawa, T. and Gong, J. P. [2024] "Pre-yielding and necking process of double network hydrogels revealed by sample geometry effects," *Extreme Mechanics Letters* **69**, 102163.

You, J. P. and Liu, Z. S. [2024] "Revealing novel insights into the toughening mechanism of double network hydrogels via uniaxial tensile tests," *Journal of the Mechanics and Physics of Solids* **190**, 105710.

You, J. P., Wang, C., Li, Z. X. and Liu, Z. S. [2025a] "Characterizing dissipated energy density distribution and damage zone in double network hydrogels," *Journal of the Mechanics and Physics of Solids* **196**, 106006.

You, J. P., Zhang, J. Y., Yang, B. S., Wang, C. and Liu, Z. S. [2025b] "Damage mechanism insights into double network hydrogels: Predicting cyclic loading behaviors via monotonic loading," *Journal of the Mechanics and Physics of Solids* **205**, 106324.

Yu, Q. M., Tanaka, Y., Furukawa, H., Kurokawa, T. and Gong, J. P. [2009] "Direct observation of damage zone around crack tips in double-network gels," *Macromolecules* **42**(12), 3852–3855.

Yuan, T., Li, C., Kolinski, J. M. and Amstad, E. [2025] "Electrostatically reinforced double network granular hydrogels," *Advanced Science* **12**(20), 2412566.

Yuk, H., Varela, C. E., Nabzdyk, C. S., Mao, X. Y., Padera, R. F., Roche, E. T. and Zhao, X. H. [2019] "Dry double-sided tape for adhesion of wet tissues and devices," *Nature* **575**(7781), 169–174.

Yuk, H., Zhang, T., Lin, S. T., Parada, G. A. and Zhao, X. H. [2016a] "Tough bonding of hydrogels to diverse non-porous surfaces," *Nature Materials* **15**(2), 190–196.

Yuk, H., Zhang, T., Parada, G. A., Liu, X. Y. and Zhao, X. H. [2016b] "Skin-inspired hydrogel-elastomer hybrids with robust interfaces and functional microstructures," *Nature Communications* **7**, 12028.

Zhang, J. L. *et al.* [2014] "Shape memory/change effect in a double network nanocomposite tough hydrogel," *European Polymer Journal* **58**, 41–51.

Zhang, J. R. *et al.* [2023a] "Rapid, autonomous high-throughput characterization of hydrogel rheological properties via automated sensing and physics-guided machine learning," *Applied Materials Today* **30**, 101720.

Zhang, K. H., Simic, R., Yan, W. Q. and Spencer, N. D. [2019a] "Creating an interface: Rendering a double-network hydrogel lubricious via spontaneous delamination," *ACS Applied Materials & Interfaces* **11**(28), 25427–25435.

Zhang, M. Z., Zhang, D., Chen, H., Zhang, Y. X., Liu, Y. L., Ren, B. P. and Zheng, J. [2021] "A multiscale polymerization framework towards network structure and fracture of double-network hydrogels," *npj Computational Materials* **7**(1), 39.

Zhang, S. H. *et al.* [2025] "Artificial intelligence-enabled hydrogels: Innovations and applications," *Journal of Materials Chemistry B* **13**(46), 14967–14981.

Zhang, T., Lin, S., Yuk, H. and Zhao, X. [2015] "Predicting fracture energies and crack-tip fields of soft tough materials," *Extreme Mechanics Letters* **4**, 1–8.

Zhang, W., Gao, Y., Zhou, Y., Wu, H., Suo, Z. and Lu, T. [2023b] "Strength and toughness of tissue adhesives depend on thickness," *Giant* **16**, 100200.

Zhang, W. L., Hu, J., Tang, J. D., Wang, Z. T., Wang, J. K., Lu, T. Q. and Suo, Z. G. [2019b] "Fracture toughness and fatigue threshold of tough hydrogels," *ACS Macro Letters* **8**(1), 17–23.

Zhang, W. L., Liu, X., Wang, J. K., Tang, J. D., Hu, J., Lu, T. Q. and Suo, Z. G. [2018] "Fatigue of double-network hydrogels," *Engineering Fracture Mechanics* **187**, 74–93.

Zhang, W. P. *et al.* [2023] "Double-network hydrogels for biomaterials: Structure-property relationships and drug delivery," *European Polymer Journal* **185**, 111807.

Zhang, Y., Fukao, K., Matsuda, T., Nakajima, T., Tsunoda, K., Kurokawa, T. and Gong, J. P. [2022] "Unique crack propagation of double network hydrogels under high stretch," *Extreme Mechanics Letters* **51**, 101588.

Zhao, R. Q., Wang, Y., Wang, S., Zhao, C. Y. and Gong, X. L. [2020] "The dissociation of physical interaction clusters under tensile deformation of hybrid double network gels," *Polymer* **210**.

Zhao, X. H. [2012] "A theory for large deformation and damage of interpenetrating polymer networks," *Journal of the Mechanics and Physics of Solids* **60**(2), 319–332.

Zhao, X. H. [2014] "Multi-scale multi-mechanism design of tough hydrogels: Building dissipation into stretchy networks," *Soft Matter* **10**(5), 672–687.

Zheng, J. X. *et al.* [2023a] "3D printed microstructured ultra-sensitive pressure sensors based on microgel-reinforced double network hydrogels for biomechanical applications," *Materials Horizons* **10**(10), 4232–4242.

Zheng, S. J., Cohen, N. and Liu, Z. S. [2022] "Large deformation adhesion study of polymetric hydrogel under different stimuli," *Mechanics of Materials* **165**, 104174.

Zheng, S. J. and Liu, Z. S. [2021] "The machine learning embedded method of parameters determination in the constitutive models and potential applications for hydrogels," *International Journal of Applied Mechanics* **13**(1), 2150001.

Zheng, Y. and Gong, J. P. [2025] "Viscous solvent effect on fracture of predamaged double-network gels examined by pre-notch and post-notch crack tests," *Journal of the Mechanics and Physics of Solids* **194**, 105926.

Zheng, Y. *et al.* [2021] "How chain dynamics affects crack initiation in double-network gels," *Proceedings of the National Academy of Sciences* **118**(49), e2111880118.

Zheng, Y., Nakajima, T., Cui, W., Hui, C. Y. and Gong, J. P. [2023b] "Swelling effect on the yielding, elasticity, and fracture of double-network hydrogels with an inhomogeneous first network," *Macromolecules* **56**(11), 3962–3972.

Zheng, Y., Wang, Y. R., Nakajima, T. and Gong, J. P. [2024a] "Effect of predamage on the fracture energy of double-network hydrogels," *ACS Macro Letters* **13**(2), 130–137.

Zheng, Y., Wang, Y. R., Tian, F. C., Nakajima, T., Hui, C. Y. and Gong, J. P. [2024b] "Unique stick-slip crack dynamics of double- network hydrogels under pure-shear loading," *Proceedings of the National Academy of Sciences* **121**(30), e2322437121.

Zhou, B. G., Li, Y. H., Chen, Y., Gao, C., Li, J. C., Bai, Z. Q. and Guo, J. S. [2022] "In situ synthesis of highly stretchable, freeze-tolerant silk-polyelectrolyte double-network hydrogels for multifunctional flexible sensing," *Chemical Engineering Journal* **446**, 137405.

Zhou, J. *et al.* [2024a] "Superior compressive and tensile bi-directional strain sensing capabilities achieved using liquid metal hybrid-hydrogels empowered by machine learning algorithms," *Chemical Engineering Journal* **479**, 147790.

Zhou, Y. F., Hu, J., Zhao, P. P., Zhang, W. L., Suo, Z. G. and Lu, T. Q. [2021] "Flaw-sensitivity of a tough hydrogel under monotonic and cyclic loads," *Journal of the Mechanics and Physics of Solids* **153**, 104483.

Zhou, Z. D., Jia, Y. T., Lu, W. J., Lei, J. C. and Liu, Z. S. [2024b] "Enhancing the crack initiation resistance of hydrogels through crosswise cutting," *Journal of the Mechanics and Physics of Solids* **183**, 105516.

Zhu, J., Yu, W. R., Xiong, H. Y., Xia, X. L., Li, Y. L. and Huang, Y. Z. [2025] "Wearable double network plasmonic hydrogel for SERS detection of urea and uric acid in sweat," *ACS Sensors* **10**(8), 6123–6131.

Zhu, J. A., Xue, Y. H. and Liu, Z. S. [2024a] "A transfer learning enhanced physics-informed neural network for parameter identification in soft materials," *Applied Mathematics and Mechanics-English Edition* **45**(10), 1685–1704.

Zhu, P. P. and Zhong, Z. [2020] "Modelling the mechanical behaviors of double-network hydrogels," *International Journal of Solids and Structures* **193**, 492–501.

Zhu, R. X., Zhu, D. D., Zheng, Z. and Wang, X. L. [2024b] "Tough double network hydrogels with rapid self-reinforcement and low hysteresis based on highly entangled networks," *Nature Communications* **15**(1), 1344.

Zhu, S. L. *et al.* [2023] "Enhanced rupture force in a cut-dispersed double-network hydrogel," *Gels* **9**(2), 158.

Zhuo, F. *et al.* [2023] "Kirigami-inspired 3D-printable MXene organohydrogels for soft electronics," *Advanced Functional Materials* **33**(52), 2308487.

Zong, T., Liu, X., Zhang, X. Y. and Yang, Q. S. [2024] "Efficient characterization of double-cross-linked networks in hydrogels using data-inspired coarse-grained molecular dynamics model," *Journal of Chemical Physics* **160**(2), 024115.